CHAPTER 1

INTRODUCTION TO GRAVITATIONAL LENSING

" Nobody sees a flower, really, it is so small. So I said to myself – I'll paint what I see – what the flower is to me but I'll paint it big and they will be surprised into taking time to look at it – I will make even busy New Yorkers take time to see what I see of flowers."

-Georgia O'Keeffe

Light paths respond to mass. The deflection of light by massive bodies gives rise to many interesting phenomena that can modify how the sources of radiation are seen by an observer. As artist Georgia O'Keeffe magnified tiny flowers to startle busy New Yorkers into noticing them, gravitational lenses magnify distant galaxies that might otherwise remain undetected. Her large-format flowers are as bright and colorful as their tiny models (Figure 1.1).

Figure 1.1 White Rose with Larkspur, No. 2 by Georgia O'Keeffe 1927 (101.6 cm x 76.2 cm).

Similarly, in addition to magnifying the source, gravitational lensing amplifies the *luminosity* of the source, enabling observation of objects too distant or intrinsically too faint to be observed without lensing. Consider a galaxy that subtends one square arcsecond on the sky. If this galaxy, when magnified by a gravitational lens, results in an image that subtends ten square arcseconds, the observed luminosity will be ten times the luminosity of the source in the absence of lensing.

On the flip side, we learn something about the artist who magnifies flowers to make even busy New Yorkers take time to notice a flower. Similarly, we can infer characteristics of the lens that magnifies background galaxies.

Strong lensing systems were found via a search algorithm developed to select potential gravitational lensing systems from the Sloan Digital Sky Survey (SDSS) database. The search algorithm, verification of the potential lensing systems, and analyses yielding the mass to lights ratios of these systems are presented in this thesis.

A brief historical introduction to the regimes of gravitational lensing (microlensing, weak lensing, and strong lensing) along with applications of lensing to the study of astrophysics are presented in this chapter. Chapter 2 provides the lensing theory and astronomical tools used in the analysis. Characteristics of the lensing and source galaxies are presented in Chapter 3. Details and results of the search algorithm are discussed in Chapter 4. Identification of the arcs is described in Chapter 5. The analysis, yielding the mass to light ratios of the lensing systems,

is presented in Chapter 6. The resultant mass to light ratios are discussed and compared to the literature in Chapter 7, which concludes with suggestions for further research.

1.1 Early History of Gravitational Lensing

Gravitational lensing is a direct consequence of general relativity. If a photon passes near a compact massive object of mass *M*, at an impact parameter *b*, the local curvature of space-time will cause the photon to be deflected by an angle

$$\alpha = \frac{4GM}{c^2 b} \qquad \text{Equation 1.1}$$

where *G* is Newton's gravitational constant and *c* is the speed of light as illustrated in Figure 1.2 (Ryden 2003).

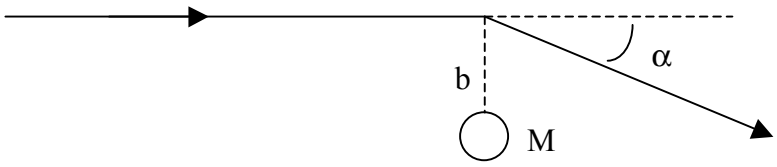

Figure 1.2 Deflection of light by a massive compact object.

Light from a distant star that just grazes the Sun's surface such that its impact parameter is equal to the radius of the Sun, R_{Sun}, should be deflected through an angle

$$\alpha = \frac{4GM_{Sun}}{c^2 R_{Sun}} = 1.7 \text{ arcsec}.$$

In 1919, after Einstein predicted a deflection of this magnitude, an eclipse expedition led by Arthur Eddington photographed stars in the vicinity of the Sun (Figure 1.3). The circular inset in Figure 1.3 shows that the expected apparent stellar positions are farther from the lens than they would be in the absence of lensing. Comparison of the eclipse photographs with photographs of the same star field taken six months earlier revealed that the positions of the stars were deflected by the amount that Einstein predicted. This result brought experimental support to the theory of general relativity (Ryden 2003).

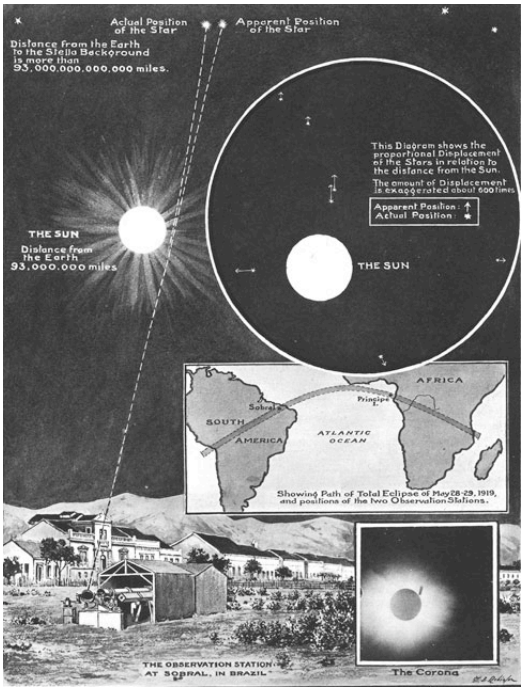

Figure 1.3 Graphical explanation of Eddington's experiment as it appeared in *Illustrated London News* of November 22, 1919 (Fernie 2005).

Einstein's notebooks contain calculations of the magnification of images and of the possibility of double images from a single source. Lensing can produce

multiple images in the *strong lensing regime*, which is the focus of this thesis. Lensing can also amplify the light curves of stars due to *microlensing*, or it can lead to small distortions at the level of a few percent in the shapes of distant galaxies in *weak lensing*.

The distinction between these regimes depends on the relative positions of the source, lens, and observer as shown in Figure 1.4.

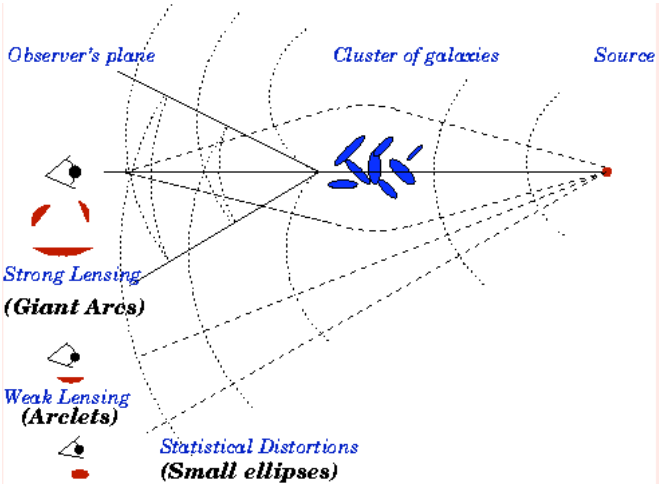

Figure 1.4 Depending on the lens configuration, the observer will see multiple and strongly distorted images (giant arcs), single distorted images with elliptical shapes (arclets), or distorted images (small ellipses).
Image from http://www.hep.upenn.edu/~bjain/lensing.html

In the strong lensing regime, multiple images of the same source are observed. Often the images are in the shape of giant arcs. For strong lensing to occur, the source, the gravitational lens, and the observer have to be sufficiently well aligned, and the bending angle has to be large enough to allow the different images to be resolved.

If the alignment is not close enough to produce multiple images, the effect of the gravitational lens can still be observed through the presence of many slightly distorted images. This is referred to as weak lensing. Since it is impossible to know the exact shape of a source a priori, a statistical analysis of a large number of images is necessary to acquire information about the distortions caused by the gravitational lens.

In the case of microlensing, the gravitational lens does cause multiple images, but the images cannot be resolved. However, since a gravitational lens can cause images to become brighter, the presence of a gravitational lens can be detected by the brightening of the image when source and lens move with respect to each other.

More detail and some history of the gravitational lensing regimes are presented in the next three sections.

1.2 Microlensing

Microlensing is a small-scale gravitational lensing effect. In microlensing, the gravitational field of the lensing object is not strong enough to form distinct images of the background source. Instead, it causes an apparent brightening of the source. Stars are expected to vary in brightness in a characteristic manner if low mass stars or planets pass in front of them, as has been detected for stars in the Magellanic Clouds and in the central bulge of our galaxy. The deflection of the source is typically of the order of μarcsecs. Therefore, the name "microlensing" is

associated with this process, and the name is generally applied to any gravitational lensing effect by a compact object producing unresolvable images of a source and a potentially large magnification of its light (Mollerach and Roulet 2002).

1.3 Weak Lensing

Small distortions in the shapes of background galaxies can be created via weak lensing by foreground galaxy clusters. By statistically averaging these small distortions, mass estimates of the clusters can be obtained.

Most of what is known about the distribution of mass in the universe comes from observations of galaxy distributions. By observing lensing by the mass, hopefully we can determine how well the light from galaxies traces the mass.

Cosmologists are interested in weak lensing by the generic large-scale structure of the universe. In this case, inferring the distribution of dark matter is not necessarily the goal. Instead, cosmologists would like measurements of statistics, such as the correlation function or its Fourier transform, to compare to theory. The main goal is to relate the observations of distortions of galaxy images to the underlying mass power spectrum (Dodelson 2003).

1.4 Strong Lensing

The sky contains many massive foreground objects, such as massive galaxies and galaxy clusters, which, when intercepting the line of sight of a galaxy in the background, can produce multiple virtual images of that galaxy. Light rays leaving a source in different directions are focused on the same point (us) by the intervening galaxy or cluster of galaxies. These are called strong lenses.

The first strong lensing observation was of the doubly imaged quasar Q0957+561 by Walsh, Carswell, and Weymann (1979). The quasar was one of many quasar candidates found in a survey of radio sources made using the MkIA radio telescope at Jodrell Bank. A pair of blue objects separated by ~6 arcseconds was found within the field of the quasar in Palomar Observatory Sky Survey (POSS) images. The two blue objects were found to have nearly identical spectra in subsequent observations using the 2.1 m telescope at Kitt Peak National Observatory (KPNO). Observations from Mauna Kea and Palomar showed a luminous galaxy almost in front of one quasar image and a surrounding cluster that might also contribute to the lensing. The quasar is at redshift $z = 1.41$ while the lensing galaxy is at redshift $z = 0.355$. There is a 1.14-year time lag between the two images. An optical image of QSO 0957+561 taken by HST's WFPCII camera is shown in Figure 1.5.

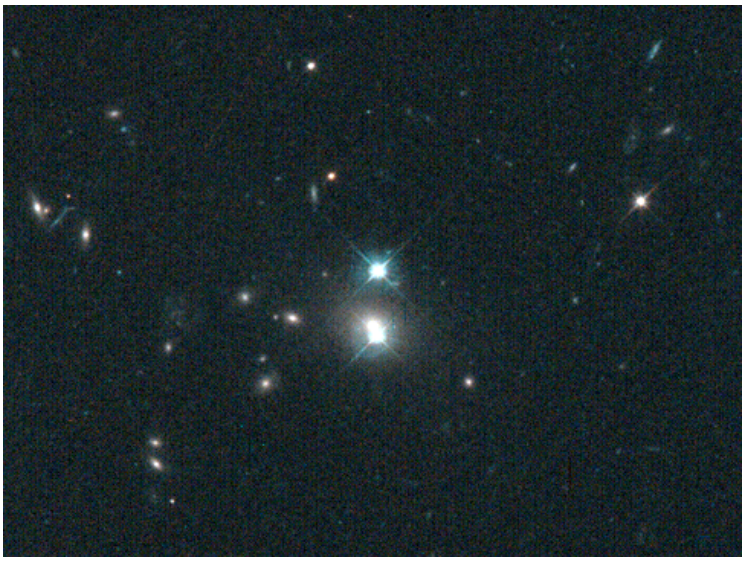

Figure 1.5 HST image of QSO 0957+561.

The magnification produced by strong lensing affects the observable properties of active galaxies, quasars, and any other lensed sources. Strong lensing also may provide information for cosmology. For example, the time delay among the multiple images of a quasar can be used to measure the Hubble constant. Also, lensing statistics are sensitive to cosmological parameters, with the frequency of multiple imaging giving constraints on the cosmological constant and the distribution of image splitting probing the amount of structure on galaxy and cluster scales (Mollerach and Roulet 2002, Dodelson 2003).

The first large luminous arc produced by strong lensing (Figure 1.6) was found in the massive nearby cluster, Abell 370, in 1986 by Lynds and Petrosian (1986) at Kitt Peak National Observatory (KPNO) and by Soucail et al. (1987a) at the Canada France Hawaii Telescope (CFHT).

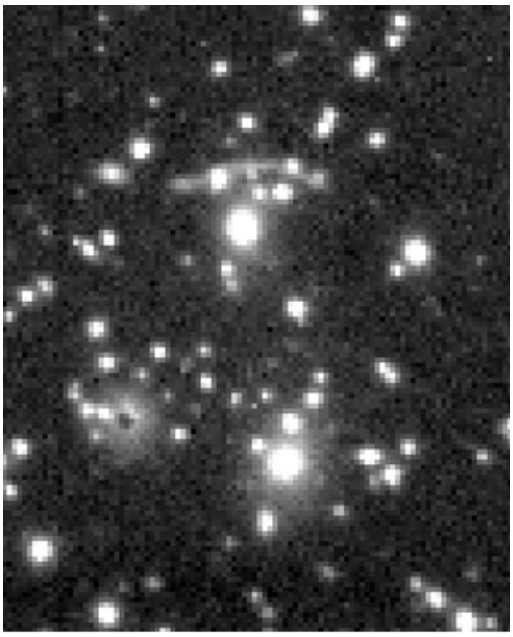

Figure 1.6 First observed giant gravitational arc (Soucail et al. 1987a).

Giant arcs are due to the lensing effect of rich clusters of galaxies on background galaxies, with huge magnifications that can distort the galaxy shapes into long arcs around the clusters' cores. The cluster Abell 2218 contains the most famous example of gravitationally lensed arcs (Figure 1.7). The large cluster in the foreground, Abell 2218, distorts the shapes of the background galaxies, leading to the distinctive pattern of elliptical arcs surrounding the central region of the cluster. This case is so spectacular, partly because the cluster is very massive, but also because there is a serendipitous alignment of several groups of galaxies almost directly behind the foreground cluster. Redshifts of the arcs from follow-up spectroscopy provide evidence for lensing of three groups of galaxies by Abell 2218 (Ebbels et al. 1998).

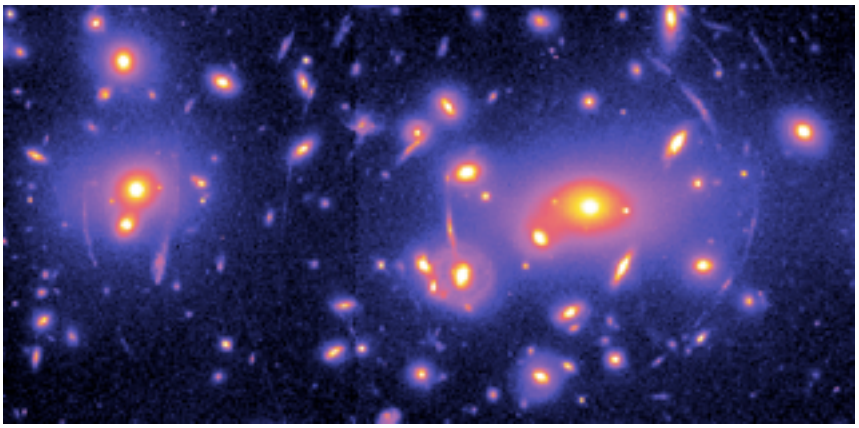

Figure 1.7 Foreground galaxies in the cluster Abell 2218 distort the images of background galaxies. Giant elliptical arcs surround the central region of the cluster at right.

Until recently, the most massive galaxies and galaxy clusters have been the object of gravitational lensing studies. Galaxy groups are comprised of a lower density of galaxies than clusters, making them more difficult to detect. The study of lensing by intermediate-scale structures, like galaxy groups, could lead to a better understanding of the evolution of structure in the universe. A key issue is to understand the transition between galaxy-scale and cluster-scale structures. The study of groups of galaxies in the Canadian Network for Observational Cosmology (CNOC) survey using weak lensing by Parker et al. (2005) provided a constraint on their mass to light ratios (Cabanac et al. 2007). The CFHT Legacy Survey (CFHTLS) plans to produce a large sample of galaxy-, group-, and cluster-scale strong lenses via a deep photometric survey. A preliminary sample of about 40 strong lensing candidates has been discovered using an automated search. This

sample demonstrates that it is possible to detect a large population of strong lenses from galaxy groups with typical masses of about $10^{13} h^{-1} M_{Sun}$ (Cabanac et al. 2007).

The strong lensing systems discovered in the SDSS that are the subject of this thesis represent systems lensed by massive galaxies as well as groups of galaxies with masses comparable to those found by CFHTLS.

1.5 What We Can Learn from Strong Lensing

Since the light paths of the lensed galaxies respond to *mass*, analysis yields the total mass of the lens, providing a probe of dark matter. In this thesis, the total mass of each lens is calculated from the geometry of the system. The luminosity of the lensing galaxy (or galaxies) is measured from the photometric information provided by each image. The resultant mass to light ratios are then presented as a function of mass and scale. These ratios are then compared to literature.

The strongly lensed source galaxies are useful for studies of galaxy evolution. The magnified galaxies are often better resolved, permitting more detailed study of their structure and dynamics than would be possible without lensing. Such galaxies, in particular, Lyman break galaxies (LBGs), are described in Chapter 3.

Although beyond the scope of this thesis, gravitational lensing systems are also valuable as training sets for automated arc searches. Automated searches are actively being developed with the hope of obtaining a much larger data set (Estrada

et al. 2007). Better statistics are required to understand the probability for galaxy clusters to produce arcs and, ultimately, to study cluster structure and cosmology.

1.6 Compare Another "Natural Tool"

Gravitational lenses can be considered as natural telescopes, magnifying and amplifying cosmic signals. Another example of a natural amplifier is the astrophysical maser. Maser emission has been detected from many different molecules in different astronomical environments. The first direct evidence for stimulated emission in an OH cloud was observed in the direction of the pulsar B1641-45 by Weisberg et al. 2005. The maser amplification is modified as the pulsar cycles on and off (Figure 1.8). Like gravitational lensing, the pulsar (or other radio source) and maser must be aligned to achieve amplification (Figure 1.9). From the strength of the maser line it can be calculated that approximately five excess photons are stimulated in the cloud for every 100 passing through it. This particular OH cloud amplified by 5%, but OH clouds of other sizes and densities may provide higher amplification (Weisberg et al. 2005).

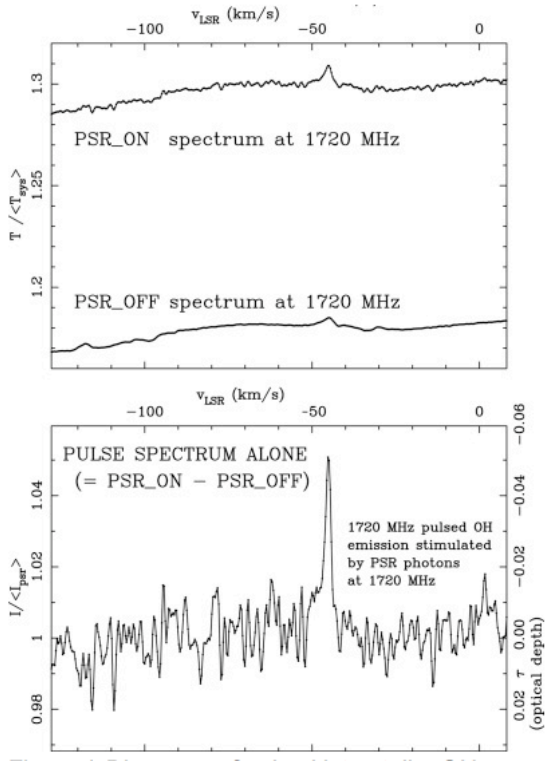

Figure 1.8 Evidence for maser amplification of pulsar signal (Weisberg et al. 2005).

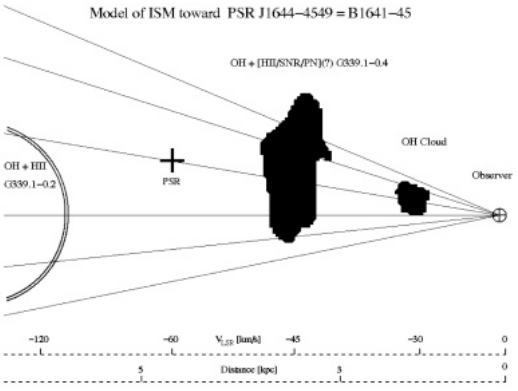

Figure 1.9 A schematic model of the interstellar medium (ISM) toward PSR B1641-45 showing the alignment of the pulsar, OH maser, and observer. (Weisberg et al. 2005).

CHAPTER 2

LENSING THEORY, DISTANCE MEASURES, AND PHOTOMETRIIC MAGNITUDES

"Music is the arithmetic of sounds as optics is the geometry of light."
-Claude Debussy

The tools required for the analysis of the lensing systems studied in this thesis are presented in this chapter. First, lensing theory with an emphasis on concepts used for calculating the mass of the lenses is presented. This is followed by cosmological distance measures used in gravitational lensing theory. Third, photometric magnitude scales are introduced. Last, *k*-corrections and galactic extinction correction are presented.

2.1 Lensing Theory

There are numerous approaches to lensing theory, including "exact" methods, iterative methods, and the thin lens approximation (Kling et al. 2000). When the extent of the lensing mass along the line of sight is small compared to the distance between the observer and the lens and between the lens and the source, the

approximation that the deflection of the light takes place at one point, the location of the lens, can be made, i.e., the thin lens approximation.

Lensing theory developed using the thin lens approximation is presented in *Lectures on Gravitational Lensing* by Narayan and Bartelmann (1997). The lensing relations relevant to the analysis in this thesis are taken from Narayan and Bartelmann and are presented below.

2.1.1 The Lens Equation

The geometry of a typical lensing system is shown in Figure 2.1. A light ray from a source S is deflected by the angle $\hat{\alpha}$ at the lens and reaches an observer O. The angle between the optical axis and the true source position is β, and the angle between the optical axis and the image I is θ. The distances between the observer and lens, lens and source, and observer and source are D_d, D_{ds}, and D_s, respectively.

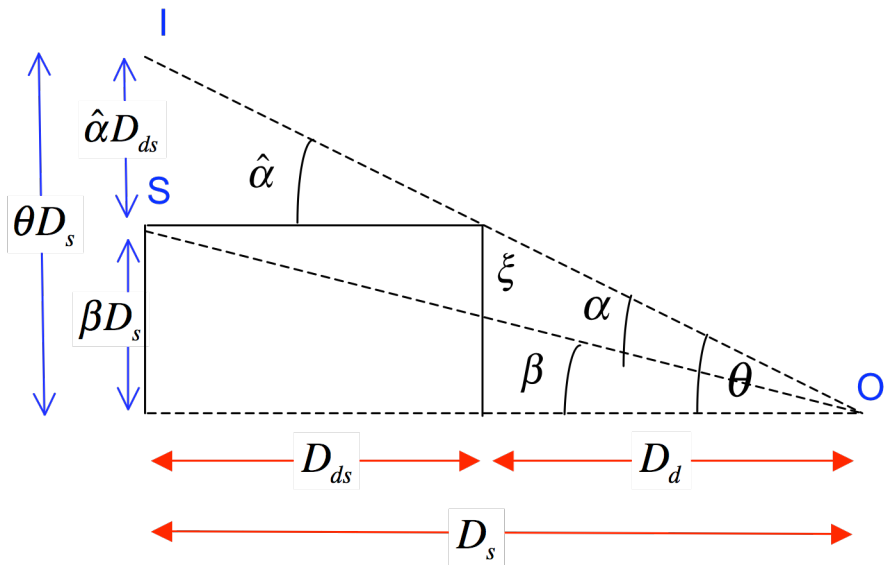

Figure 2.1 Illustration of a gravitational lens system (Narayan and Bartelmann 1997).

This is valid for curved space-time as long as the distances (D_d, D_{ds}, and D_s) used are angular diameter distances. Angular diameter distance is described in Section 2.2.4. Note that in general, $D_{ds} \neq D_s - D_d$.

From Figure 2.1,

$$\theta D_s = \beta D_s + \hat{\alpha} D_{ds}.$$

Defining a reduced deflection angle

$$\alpha = \frac{D_{ds}}{D_s}\hat{\alpha},$$

the positions of the source and image can be related through the *lens equation,*

$$\beta = \theta - \alpha.$$

The lens equation was derived using the small angle approximation

separation=angle x distance.

2.1.2 Einstein Radius

For the case of a circularly symmetric lens, the deflection angle points toward the center of symmetry,

$$\hat{\alpha}(\xi) = \frac{4GM(\xi)}{c^2 \xi},$$

where ξ is the distance from the lens center (shown in Figure 2.1) and $M(\xi)$ is the mass enclosed within radius ξ.

For a circularly symmetric lens with an arbitrary mass profile, $M(\theta)$, using the deflection angle $\hat{\alpha}(\xi)$ and the reduced deflection angle, α, above, the lens equation is

$$\beta(\theta) = \theta - \frac{D_{ds}}{D_d D_s} \frac{4GM(\theta)}{c^2 \theta}.$$

Due to rotational symmetry, a source on the optical axis ($\beta = 0$) would be imaged as a ring with radius

$$\theta_E = \left[\frac{4GM(\theta_E)}{c^2} \frac{D_{ds}}{D_d D_s} \right]^{1/2}.$$

θ_E is referred to as the Einstein radius.

Thus, clusters of galaxies at cosmological distance (~*Gpc*) with $M \sim 10^{15} M_{Sun}$ can result in lensing with Einstein radii of tens of arcseconds. For lensing by single galaxies or groups of galaxies considered in this thesis, with masses ranging from $10^{12} - 10^{13}\ M_{Sun}$, the Einstein radii would be correspondingly smaller, on the order of 10 arcseconds or less.

In the case of multiple imaging, the typical angular separation of images is of order $2\theta_E$. Sources closer than θ_E to the optical axis experience strong lensing in the sense that they are significantly magnified. Sources well outside the Einstein radius are magnified very little.

2.1.3 Lensing by a Singular Isothermal Sphere

One model for the mass distribution in galaxies assumes that the stars and other mass components behave like particles of an ideal gas, confined by their combined, spherically symmetric gravitational potential. This mass distribution, called a *singular isothermal sphere* (SIS), can be written as

$$\rho(r) = \frac{\sigma_v^2}{2\pi G}\frac{1}{r^2},$$

where ρ is the mass density, σ_v is the velocity dispersion of the stars, and *r* is the radius of the SIS.

This is the mass distribution that will be assumed in the analysis of the lensing systems studied in this thesis. Since $\rho \propto r^{-2}$, the mass *M(r),* increases with *r.* Therefore the rotational velocity is

$$v_{rot}^2(r) = \frac{GM(r)}{r} = 2\sigma_v^2 = \text{constant}.$$

This simple model approximately produces the observed flat rotation curves of galaxies.

In the case of the circularly symmetric SIS lens, the origin can be shifted to the center of symmetry, reducing the problem to one dimension. Projecting along the line of sight, the surface mass density is

$$\Sigma(\xi) = \frac{\sigma_v^2}{2G}\frac{1}{\xi}$$

where ξ is the distance from the center of the two-dimensional profile.

Narayan and Bartelmann show that the deflection angle corresponding to the SIS mass distribution is

$$\hat{\alpha} = 4\pi\frac{\sigma_v^2}{c^2}.$$

The resulting Einstein radius of the singular isothermal sphere is

$$\theta_E = 4\pi\frac{\sigma_v^2}{c^2}\frac{D_{ds}}{D_s} = \hat{\alpha}\frac{D_{ds}}{D_s} = \alpha.$$

Due to circular symmetry, the lens equation for the SIS is one-dimensional. Multiple images are obtained only if the source lies inside the Einstein ring ($\beta < \theta_E$). When this condition is satisfied, the lens equation has two solutions:

$$\theta_{\pm} = \beta \pm \theta_{E.}$$

The images at $\theta_{\pm}$, the source, and the lens lie on a straight line.

2.1.4 Why Do We See Arcs?

Consider a circular galaxy behind a large lensing mass density with the observer out of the page as shown in Figure 2.2a. Since the light rays are deflected

by the lensing mass, we do not observe a circular image. The light rays originating from the bottom of the source (the ones closer to the lens) are bent more than those farther from the lens. The light rays are bent such that the bottom appears farther away from the lens. Note that rays are bent toward the lens, so that as you extrapolate backward, the more a ray is bent toward the lens, the farther away the source appears to be. Images will therefore be distorted as in Figure 2.2b. The net effect is to turn a circular galaxy into the arc shown in Figure 2.2c (Dodelson 2003).

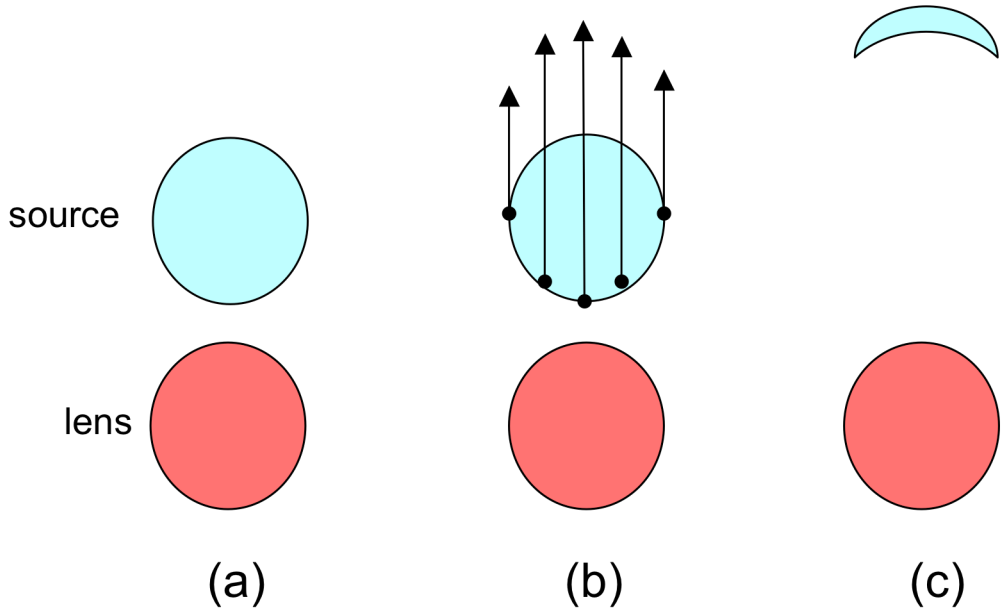

Figure 2.2 Arc formation.
(a) The circular source galaxy (blue) is located behind the lens (red). The observer is out of the page so that the foreground lens is between the observer and the source. (b) Light rays from the source are deflected as they pass near the lens. Rays traveling closest to the lens get deflected the most. (c) The resulting image is an arc.

2.1.5 Cluster Mass inside a Giant Arc

The location of an arc in a cluster provides a simple way to estimate the projected cluster mass within a circle traced by the arc (Narayan and Bartelmann 1997). For a circularly symmetric lens, the radius of the circle traced by the arc (θ_{arc}) gives an estimate of the Einstein radius (Narayan and Bartelmann 1997).

It follows that, for an SIS, the mass can be estimated by

$$M = \theta_E^2 \left(\frac{c^2}{4G} \frac{D_d D_s}{D_{ds}} \right), \qquad \text{Equation (2.1)}$$

with $\theta_E = \theta_{arc}$. Plugging in specific numbers gives

$$M(\theta) \approx 1.1 \times 10^{14} M_{Sun} \left(\frac{\theta}{30''} \right)^2 \left(\frac{D}{1\ \text{Gpc}} \right).$$

2.1.6 Conservation of Surface Brightness

Lensing does not change the intrinsic surface brightness of a source (Mollerach and Roulet 2002). Surface brightness is the flux of energy of a certain frequency, ν, crossing a unit area perpendicular to the direction of propagation, per unit time, per unit solid angle, per unit frequency interval, i.e.,

$$I(\nu) = \frac{\mathrm{d}E}{\mathrm{d}t \mathrm{d}A \mathrm{d}\Omega \mathrm{d}\nu}.$$

The radiation emitted from a source is a flux of photons characterized by a phase-space density, $f(\vec{x}, \vec{p}, t)$. The number of photons in a given phase-space volume is

$$f(\vec{x},\vec{p},t)=\frac{dN}{d^3\vec{x}d^3\vec{p}}.$$

The beam energy is $\mathrm{d}E = E_\gamma \mathrm{d}N$, the individual photon energies are $E_\gamma = h\nu = cp$, $\mathrm{d}^3\vec{p} = p^2 \mathrm{d}p\mathrm{d}\Omega$, and $\mathrm{d}^3\vec{x} = \mathrm{d}A c\mathrm{d}t$. This yields

$$f(\vec{x},\vec{p},t)=\frac{dE}{hcp^3 \mathrm{d}\nu \mathrm{d}\Omega \mathrm{d}A\mathrm{d}t}=\frac{I(\nu)}{hcp^3}.$$

Liouville's theorem applied to the photon beam requires that the phase-space density, *f,* be unchanged during the photon propagation if no absorption or emission of photons takes place. This implies the result that $I(\nu)/p^3$ remains constant along its trajectory, and therefore it is not affected by gravitational deflection of the light (Mollerach and Roulet 2002).

2.1.7 Magnification and Amplification

The flux received from a source is the product of its surface brightness and the solid angle it subtends. Since the surface brightness is conserved but the differential deflection of light rays changes the shape and the solid angle that the source subtends on the sky, the source luminosity will be amplified by the effect of gravitational lensing by an amount

$$A=\frac{d\Omega}{d\Omega_o},$$

where $d\Omega$ is the observed solid angle and $d\Omega_o$ is the corresponding solid angle in the absence of lensing (Mollerach and Roulet 2002). This is very different from

what happens in optically magnified images. In that case, the magnified images are dimmer, as shown in Figure 2.3.

Figure 2.3 Orion Nebula magnified by an optical lens approximately 50x, 80x, and 120x.
Notice that as the magnification increases, the field of view shrinks and the image gets dimmer. Dimming does *not* accompany magnification when the magnification is due to gravitational lensing.

Figure 2.4 shows the magnified images $I_{\pm}$ of an extended source S lensed by a point mass.

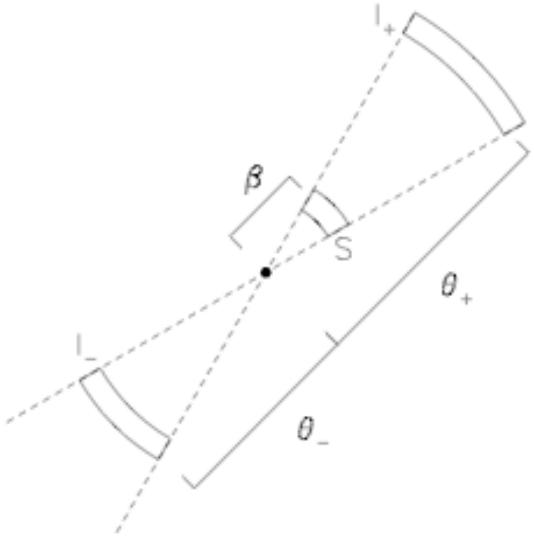

Figure 2.4 Magnified images of a source lensed by a point mass (Narayan and Bartelmann 1997)

For a circularly symmetric lens, the magnification factor for a gravitational lensing system, μ, is given by

$$\mu = \frac{\theta}{\beta}\frac{d\theta}{d\beta}.$$

The magnification produced by lensing by a singular isothermal sphere is

$$\mu_{\pm} = \frac{\theta_{\pm}}{\beta} = 1 \pm \frac{\theta_E}{\beta} = \left(1 \mp \frac{\theta_E}{\theta \pm}\right)^{-1}.$$

2.2 Distance Measures

Observational astronomy considers how objects with given properties, such as luminosity and size, will appear to us. It is concerned with the dependence of that appearance on the cosmological model.

A description of two distance measures required to calculate the mass to light ratios of the lenses studied, angular diameter distance and luminosity distance, are presented below (Hogg 2000). First, the cosmological parameters required to define these distance measures will be presented.

2.2.1 Cosmological Parameters

The Hubble constant, H_0, is the constant of proportionality between the recession speed, v, and the distance, d, in the expanding universe:

$$v = H_0 d.$$

The subscript "0" refers to the present epoch because H can change with time. The dimensions of H_0 are inverse time, but it is usually written

$$H_0 = 100h \text{km s}^{-1} Mpc^{-1},$$

where h is a dimensionless number currently thought to be about ~0.7. The current WMAP best fit value, H_0=73.2 km/s/Mpc, is also consistent with other measurements from HST, Cepheids, supernova, and gravitational lensing (Spergel et al. 2007).

If a homogeneous, isotropic, and matter-dominated universe is assumed, the following relation describes the geometry of the universe:

$$\Omega_M + \Omega_\Lambda + \Omega_k = 1$$

where

$$\Omega_M = \frac{8\pi G\rho_0}{3H_0^2}$$

is the matter density;

$$\Omega_\Lambda = \frac{\Lambda c^2}{3H_0^2}$$

is the density due to a cosmological constant; and Ω_k is the density parameter that measures the curvature of space.

In the calculations in this thesis, a flat universe is assumed ($\Omega_k = 0$), so $\Omega_M + \Omega_\Lambda = 1$. Furthermore, it is assumed that $\Omega_M = 0.3$ and $\Omega_\Lambda = 0.7$, which are consistent with the most recent cosmological values determined by WMAP (Spergel et al. 2007).

2.2.2 Redshift

The redshift of an object is the fractional Doppler shift of its emitted light resulting from radial motion

$$z \equiv \frac{\nu_e}{\nu_o} - 1 = \frac{\lambda_o}{\lambda_e} - 1,$$

where ν_o and λ_o are the observed frequency and wavelength and ν_e and λ_e are the emitted frequency and wavelength.

2.2.3 Angular Diameter Distance

The angular diameter distance, D_A, is defined as the ratio of an object's physical transverse size to its angular size (in radians). It is used to convert angular separations in telescope images into proper separations at the source. Angular diameter distance is related to the transverse comoving distance, D_M, by

$$D_A = \frac{D_M}{1+z},$$

where D_M is equal to the line of sight comoving distance, D_C, for $\Omega_k = 0$,

$$D_C = \frac{c}{H_0} \int_0^z \frac{dz'}{E(z')},$$

where

$$E(z) \equiv \sqrt{\Omega_M (1+z)^3 + \Omega_\Lambda}\,.$$

A plot of D_A vs. z is shown in Figure 2.5 for three values of Ω_M for a flat universe.

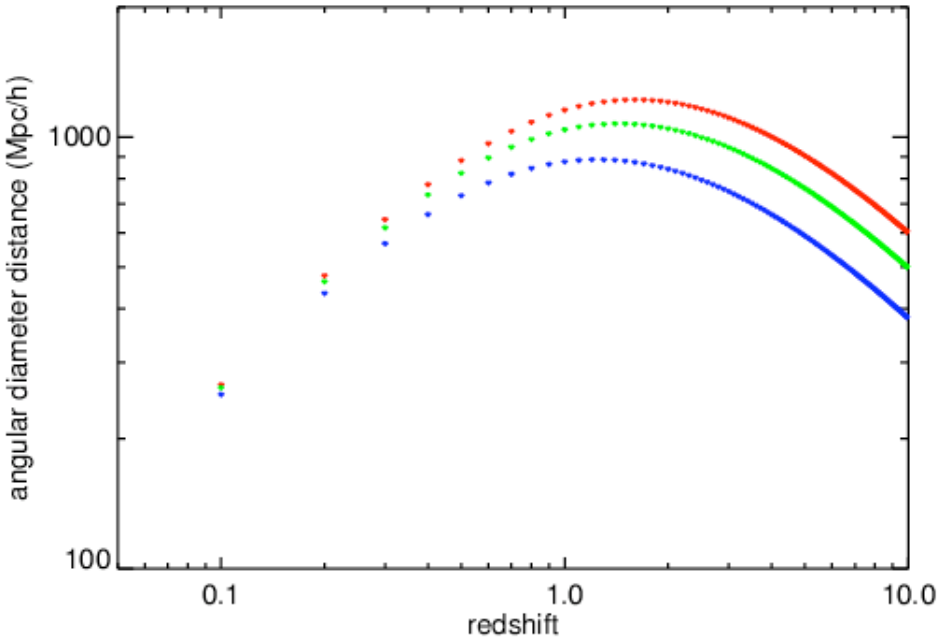

Figure 2.5 The angular diameter distance as a function of redshift for three different spatially flat cosmologies. From bottom to top: Ω_M=1.0, 0.5, 0.3.

The angular diameter distance between two objects at redshifts z_1 and z_2, D_{A12}, is used in gravitational lensing (i.e., the distance between the source and the lens). This is not equal to the difference between the two individual angular diameter distances. For $\Omega_k = 0$,

$$D_{A12} = \frac{1}{1+z_2}(D_{C2} - D_{C1}),$$

or, in terms of angular diameter distances and redshifts,

$$D_{A12} = \frac{1}{1+z_2}[D_{A2}(1+z_2) - D_{A1}(1+z_1)] = D_{A2} - D_{A1}\frac{(1+z_1)}{(1+z_2)}.$$

2.2.4 Luminosity Distance

Cosmic expansion causes photons to lose energy (as they are redshifted). The apparent brightness of a distant object is diminished by one power of 1+*z* because each photon carries less energy and by another power of 1+*z* because those photons arrive at a slower rate. An object that we observe with redshift *z* at the present time, t_0 , lies at comoving distance D_M . Its light is spread over an area $4\pi D_M^2$. The flux, *S,* of energy that we receive is related to the total luminosity, *L*, by

$$S = \frac{L}{4\pi D_L^2},$$

analogous to the familiar inverse square law where D_L is the luminosity distance and $D_L = (1+z)D_M$ (Sparke and Gallagher 2000).

The relation between the angular diameter distance and luminosity distance is

$$D_L = D_A(1+z)^2.$$

A plot of D_L vs. z is shown in Figure 2.6 for three values of Ω_M for a flat universe.

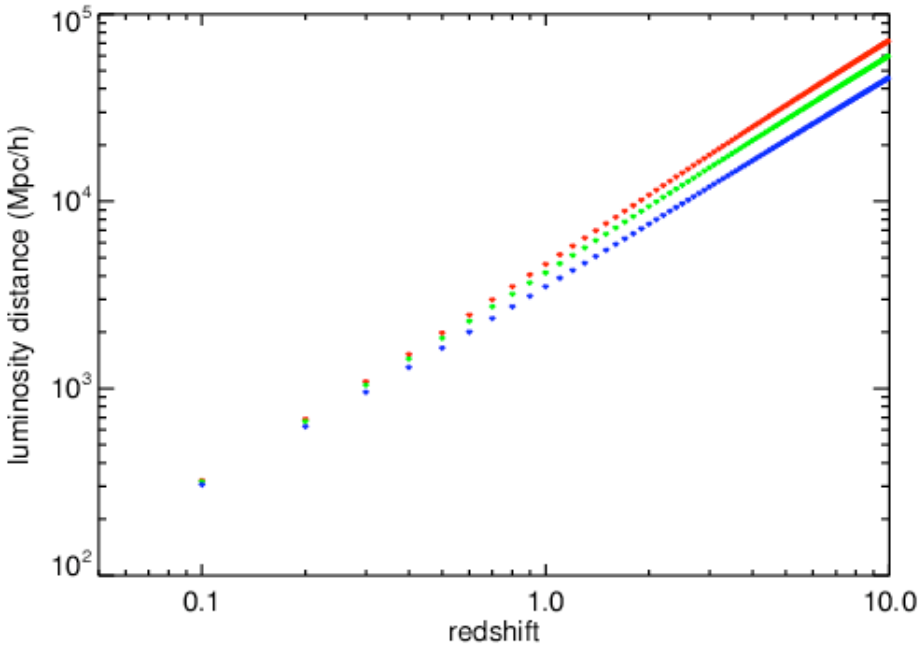

Figure 2.6 The luminosity distance as a function of redshift for three different spatially flat cosmologies. From bottom to top: Ω_M=1.0, 0.5, 0.3.

2.3 Photometric Magnitude

The magnitudes and colors of objects were used to search for gravitational lensing systems. Knowledge of the photometric system used by the SDSS was essential to implement such a search.

The ancients, particularly Hipparchus, set the tradition for the magnitude scale that we use today. Modern measurements of stellar brightness revealed that the magnitude scale is nearly logarithmic in apparent brightness in such a way that a difference of 5 magnitudes corresponded to nearly a factor of 100 in apparent brightness. To preserve the value of astronomical records and tradition, it was

decided by international agreement that the ancient nomenclature should be retained but with the precise definition:

$$\frac{b_1}{b_2} = \left(100^{1/5}\right)^{m_2 - m_1} = 2.512^{m_2 - m_1}, \qquad (2.2)$$

where m_1 and m_2 are the apparent magnitudes of two stars with flux, b_1 and b_2 (Clayton, 1983).

The magnitude scale shown in equation 2.2 defines the difference in two magnitudes, but it is equivalent to

$$m = -2.5 \log b + c ,$$

where c is the zero point constant that depends on the system of magnitudes used and on the units of flux.

2.3.1 Color and the *k*-correction

Astronomical observations are typically made through a set of bandpass filters. This is especially valuable for sky surveys in which an enormous number of objects are imaged, and spectra cannot be obtained for all of them. Therefore, even if a spectrum is not available, the characteristics of an object can be studied via a color-magnitude or a color-color plot.

The color of an object is defined as the difference in the magnitudes observed through two different filters. Just as objects have different spectra depending on their physical and chemical characteristics, objects have different colors. For example, two thermal radiation curves are shown in Figure 2.7. The colored dots

mark the center wavelengths of the SDSS's ultraviolet, green, and red bandpass filters. The graph shows how the SDSS's images provide three "samples" of the thermal radiation curve, where each sample is the intensity observed through each of three filters. For both curves, the green-wavelength intensity is greater than the ultraviolet-wavelength intensity. The green magnitude is less than the ultraviolet magnitude. Because magnitude decreases as the intensity of light emitted by a star increases, magnitude decreases moving up the y-axis on this graph. By definition,

$$u - g = -2.5\log_{10}[\text{intensity}(u)] + 2.5\log_{10}[\text{intensity}(g)].$$

So u-g, which is the difference between the ultraviolet and green magnitudes, is more positive (redder) for the cooler T=4730 curve. Similarly, g-r is more positive (redder) for the cooler T = 4730 curve.

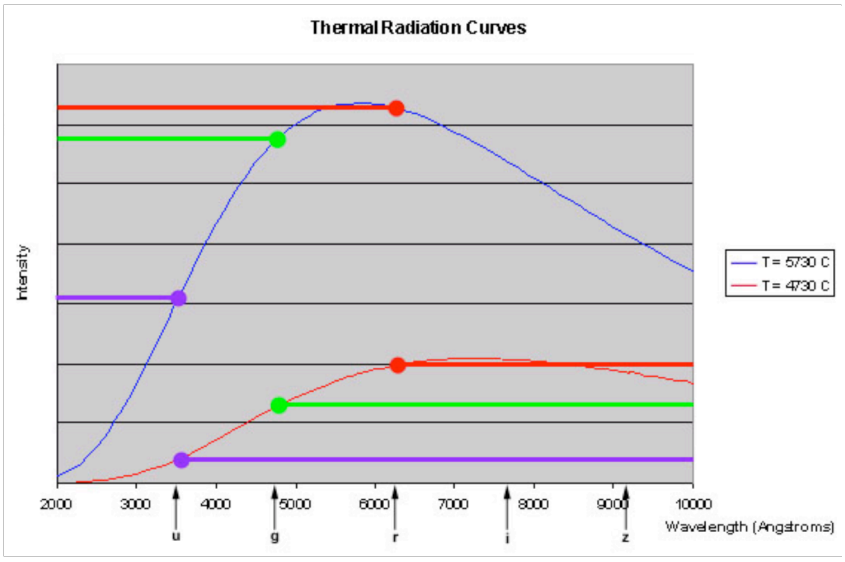

Figure 2.7 Thermal radiation curves for stars of two different temperatures ($4730^{\circ}C$ and $5730^{\circ}C$).

Although the spectra of astronomical objects are more complex than thermal radiation curves, color can be applied in a similar way to study these objects.

The luminosity distance refers to the total luminosity of the source across all wavelengths (called the bolometric luminosity). Due to the redshifting of light from distant sources, the distribution of the light received by each filter is dependent on the distance to the source, the shape of the object's spectrum, and the shape of the bandpass. This is shown in Figure 2.8. If enough is known about the spectrum of the object, a correction, called the *k*-correction, can be applied to account for this. The *k*-correction corrects different observed-frame bandpasses, at different redshifts, to the same rest-frame bandpass.

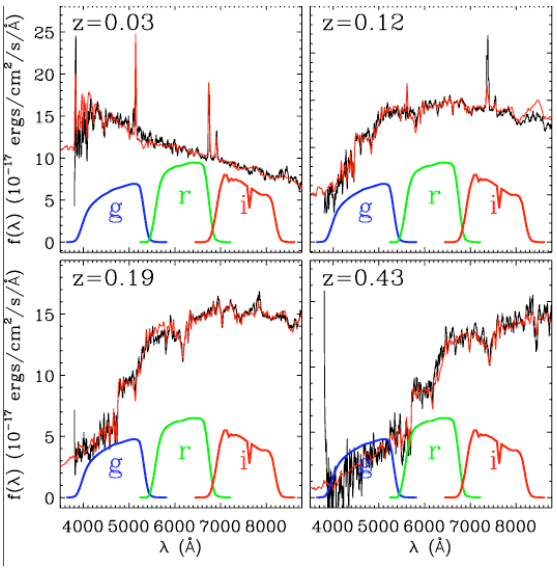

Figure 2.8 Spectra from the SDSS and the SDSS g, r, and i bandpasses. The observed flux through each passband is a function of the shape of the spectrum, the shape of the filter, and how highly redshifted the object is. From **http://cosmo.nyu.edu/blanton/kcorrect/#concept**

2.3.2 The AB_ν System

The SDSS photometric system is a five-band (u, g, r, i, z) wideband CCD system with a wavelength coverage from 3000 to 11,000A (Figure 2.9). The zero point magnitudes are based on an updated version of the spectrophotometric AB_ν system (Fukugita et al. 1996). The AB_ν system is defined such that *every* filter has a zero point flux density of 3631 Jy, where 1 Jy = 10^{-26} W Hz^{-1} m^{-2} = 10^{-23} erg s^{-1} Hz^{-1} cm^{-2}.

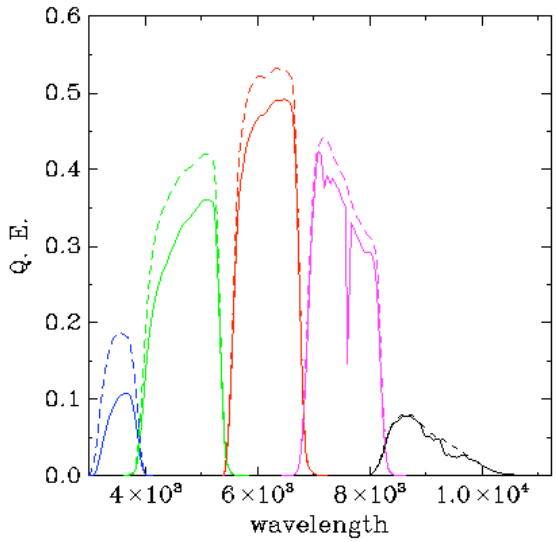

Figure 2.9 SDSS filter system.

The great advantage of the AB_ν system is that the magnitude is directly related to physical units via

$$AB_\nu = -2.5 \log f_\nu (\text{ergs s}^{-1}\ \text{cm}^{-2}\ \text{Hz}^{-1}) - 48.60\ ,$$

where f_ν is the flux per unit frequency. Therefore, in the SDSS AB_ν system (Oke and Gunn, 1983), a magnitude 0 object should produce the same signal as a source of $f_\nu = 3631$ Jy.

The spectral energy distributions (SEDs) of four F subdwarf stars (chosen by Oke and Gunn) whose absolute fluxes are calibrated against the absolute flux of α Lyr, are taken as the defining monochromatic magnitude standards for the AB_ν system.

Bev Oke invented the terminology *"AB."* It may represent *AB*solute, since the *AB* system is referenced to absolute spectrophotometry. [1]

The AB_ν system is based on spectral energy distributions expressed in f_ν.

2.3.3 f_ν vs. f_λ

The spectral energy distribution of an object can be expressed in f_ν or f_λ. The total power must be independent of which units are used, so one can equate differentials to determine the conversion from f_λ to f_ν:

[1] J. Gunn, personal correspondence, 2007 "Bev Oke invented the terminology before I came on the scene; I *think* it is just short for *AB*solute, since it is referenced to absolute spectrophotometry."

$$\int f_\lambda d\lambda = \int f_\nu d\nu$$

$$f_\lambda d\lambda = f_\nu d\nu$$

$$f_\lambda = f_\nu \frac{d\nu}{d\lambda}$$

$$\nu = \frac{c}{\lambda} \rightarrow f_\lambda = f_\nu \frac{d\left(\frac{c}{\lambda}\right)}{d\lambda}$$

$$f_\lambda = f_\nu \left(-\frac{c}{\lambda^2}\right)$$

The conversion from f_λ to f_ν can also be shown via dimensional analysis:

$$\frac{[f_\nu]}{[f_\lambda]} = \frac{\frac{W}{m^2 \cdot \nu}}{\frac{W}{m^2 \cdot \lambda}}$$

$$\frac{[f_\nu]}{[f_\lambda]} = \frac{\lambda}{\nu}$$

$$\nu = \frac{c}{\lambda}$$

$$\frac{[f_\nu]}{[f_\lambda]} = \frac{\lambda}{c/\lambda}$$

$$\frac{[f_\nu]}{[f_\lambda]} = \frac{\lambda^2}{c}$$

$$[f_\lambda] = \frac{c}{\lambda^2}[f_\nu]$$

An object that has a flat spectrum in f_ν does not exhibit a flat spectrum in f_λ but has a spectrum proportional to $1/\lambda^2$. This is shown graphically in Figure 2.10.

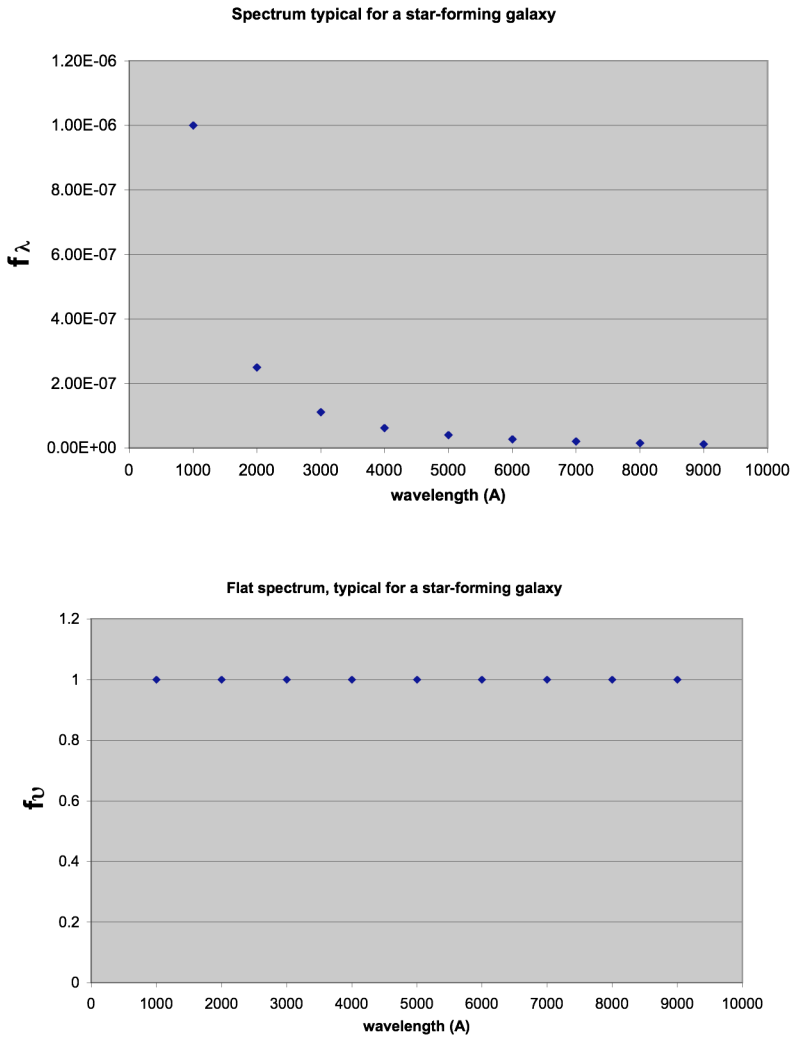

Figure 2.10 The same spectral information shown in f_λ (top) and f_ν (bottom).

2.4 Corrections for Galactic Extinction

The dust in our galaxy scatters and absorbs light. The amount of extinction due to dust is dependent on the location (right ascension and declination) of the source. Observed magnitudes can be corrected for galactic extinction using estimates of galactic extinction provided by the full-sky reddening maps of Schlegel, Finkbeiner, and Davis (1998). The extinction correction for each object is provided in the SDSS database.

2.5 Units

The standard unit of mass used by astronomers is the solar mass ($M_\odot$). The Sun's mass is $1\ M_\odot = 2.0 \times 10^{30}$ kg. The total mass of our galaxy is $\sim 10^{12}\ M_\odot$ (Ryden 2003).

The Sun also provides the standard unit for luminosity. In particular, we will be expressing luminosity in units of solar luminosity for each bandpass: $L_{g,\odot}$, $L_{r,\odot}$, $L_{i,\odot}$, and $L_{z,\odot}$.

The units of quantities of interest in this study, mass (M), luminosity (L), and M/L all include factors of the parameter *h*, which was introduced in the definition of the Hubble constant, H_0, in Section 2.2.1.

The following shows that $M \propto h^{-1}$. Recalling Equation 2.1,

$$M = \theta_E^2 \left(\frac{c^2}{4G} \frac{D_d D_s}{D_{ds}} \right);$$

it follows that

$$M = \theta_E^2 \left(\frac{c^2}{4G} \frac{D_d[Mpc/h] D_s[Mpc/h]}{D_{ds}[Mpc/h]} \right)$$

$$M \propto h^{-1}.$$

The following shows that $L \propto h^{-2}$:

$$\frac{L_{LRG}}{L_\odot} = 10^{\frac{-M+M_\odot}{2.5}},$$

where (as will be shown in Section 6.2.1)

$$M = m - \left(5 \log_{10} D_L[Mpc/h]\right) - 25 - k\,.$$

M is the absolute magnitude, *m* is the apparent magnitude, and *k* is the *k*-correction. Substituting for *M*,

$$\begin{aligned}
\frac{L_{LRG}}{L_\odot} &= 10^{\frac{-(m-(5\log_{10} D_L[Mpc/h])-25-k)+M_\odot)}{2.5}} \\
&= (\text{constant}) \cdot 10^{\frac{5\log_{10} D_L[Mpc/h]}{2.5}} \\
&= (\text{constant}) \cdot 10^{2\log_{10} D_l[Mpc/h]} \\
&= (\text{constant}) \cdot 10^{\log_{10}(D_L)^2[Mpc/h]^2} \\
&= (\text{constant}) \cdot (D_L)^2[Mpc/h]^2 \\
\frac{L_{LRG}}{L_\odot} &\propto h^{-2}.
\end{aligned}$$

It follows that $M / L \propto h$:

$$\frac{M[h^{-1}]}{L[h^{-2}]} \propto h .$$

CHAPTER 3

INTRODUCTION TO GALAXY SAMPLES

"There are too many stars in some places and not enough in others."
-Mark Twain

The lensing systems studied were discovered by a search for blue, star-forming galaxies near massive, red, elliptical galaxies. Details of the search are presented in Chapter 4. Properties of the galaxies are presented in this chapter.

Star-forming galaxies appear bluer, because they are the site of ongoing star formation. Massive stars are very bright and very hot, corresponding to a black body whose spectrum peaks in the blue.

Cooler stars burn more slowly and at lower temperatures, but they will live for 10 billion years, long after the massive stars have disappeared. Because they are cooler, the light that they produce has a redder color. In elliptical galaxies, star formation has ended and all of the hot, bright stars have died out (Sparke and Gallagher 2000).

3.1 The Lensing Galaxies

The areas around brightest cluster galaxies (BCGs) and luminous red galaxies (LRGs) were searched for evidence of lensing. BCGs and LRGs, typically elliptical galaxies, are described in Chapter 4. Elliptical galaxies are likely lensing galaxies for several reasons. 1. They can be more massive than spiral galaxies. Most lens galaxies are predicted (Fukugita & Turner 1991) and observed (Keeton et al. 1998) to be early type (E and S0) galaxies. Lens samples are dominated by early type galaxies, because early type galaxies are more massive even if they are slightly less numerous. Also typical lens-image separation for a spiral galaxy lens will be smaller, and therefore more difficult to resolve (Kochanek 2004). 2. Elliptical galaxies are more likely to be in more massive group and cluster environments, which are conducive to lensing. 3. Large catalogs of LRGs and BCGs are readily available from huge sky surveys, like the SDSS. Catalogs of BCGs and LRGs are described in Chapter 5.

Elliptical galaxies lack luminous blue stars. The brightest stars in ellipticals are red giants and asymptotic giant branch stars. Elliptical galaxies are older galaxies and have not experienced any new star formation in the last 1-2 Gyr. Since bright, blue stars have lifetimes much shorter than this, elliptical galaxies emit little light below 3500 Angstroms (Sparke and Gallagher 2000).

3.1.2 Clusters

Elliptical galaxies are typically near the center of galaxy clusters. Those in rich clusters are usually giant elliptical galaxies. The BCGs in our sample are, by definition, in a cluster (as explained in Section 4.4.1). LRGs can be in a variety of environments, as evidenced by those in the lensing sample.

3.2 The Lensed Galaxies

The study of high-redshift galaxies can improve our understanding of how galaxies form and evolve. Historically, the study of high-redshift galaxies was limited to luminous active galaxies. This changed when it was realized that broad-band colors could be used to select galaxies at extremely high redshifts (Peacock 2003). An actively star-forming galaxy will have an approximately flat spectrum down to the Lyman limit of 912 Angstroms, beyond which the spectrum will be truncated by intervening absorption (Figure 3.1). These galaxies are referred to as Lyman break galaxies (LBGs).

The Lyman break occurs at the Lyman limit, 912 Angstroms, corresponding to 13.6 eV, the ionization energy of hydrogen. All other hydrogen transitions correspond to lower energies (Figure 3.2).

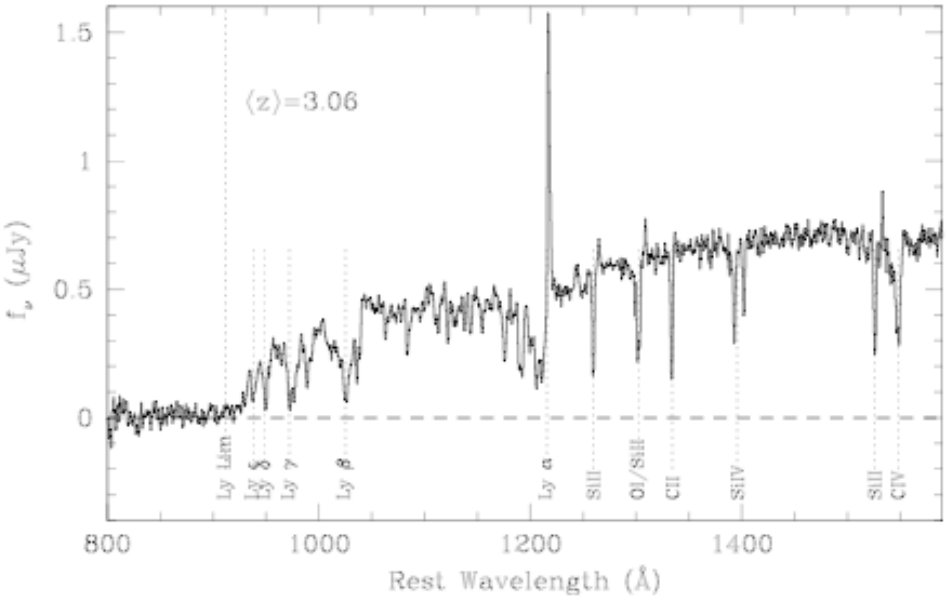

Figure 3.1 A Lyman break galaxy (a star-forming galaxy) has an approximately flat intensity spectrum in f_υ at wavelengths longer than the Lyman limit of 91.2 nm (Shapley et al. 2006).

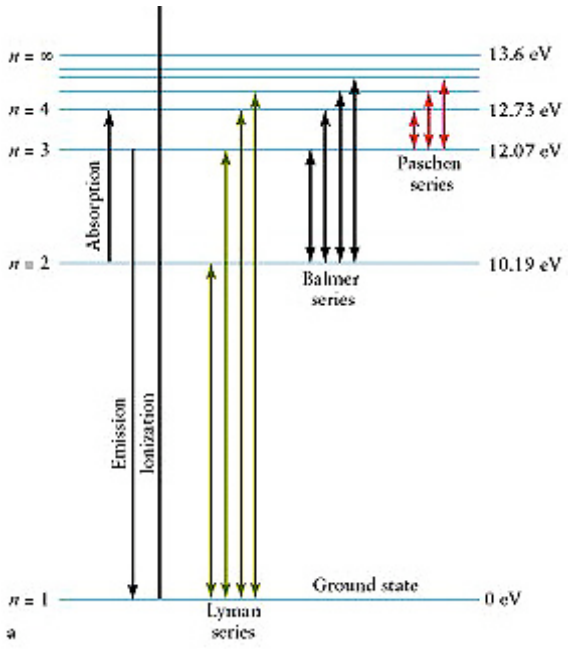

Figure 3.2 Hydrogen transitions.

In addition to the Lyman break, a star-forming galaxy exhibits an approximately flat spectrum in f_ν as shown in Figure 3.1. A prolonged burst of star formation has a flat intensity spectrum at wavelengths longer than the Lyman limit of 91.2 nm. The flatness of the spectrum is due to the flat spectra of O and B stars, whose light dominates a star-forming galaxy's luminosity.

The Lyman break is due to Lyman-continuum absorption in the atmospheres of these stars. As the light from the stars propagates toward earth, the Lyman break is strengthened, first by absorption by neutral hydrogen in the galaxy itself and then by neutral hydrogen in the intergalactic medium along the line of sight from the galaxy to the Earth. Photons blueward of the Lyman limit can ionize neutral hydrogen and hence stand a good chance of being absorbed.

Broadband imaging through filters that straddle the break (as u and g) provide an efficient way of locating high-redshift galaxies among the numerous foreground and background sources in deep images (Adelberger 2002, Steidel et al. 2003). Imaging through a third (red) filter helps distinguish high-redshift galaxies from intrinsically red objects in the more local universe. For example, at $z \cong 3$, the Lyman break corresponds to near-ultraviolet wavelengths. Therefore, a galaxy at this redshift would have very little flux in the u band while the g-r color would still be blue. This is referred to as a "u band dropout" (Sparke and Gallagher 2000).

While applying this technique to deep imaging data has been very successful (Adelberger et al. 2002, Steidel et al. 2003), these distant star-forming galaxies

would be difficult to find directly in a survey as shallow as the SDSS. However, if magnified by gravitational lensing, perhaps these galaxies could be detected via a search based on color selection. This was the strategy used to find distant star-forming galaxies near massive elliptical galaxies in this thesis.

LBGs have been studied by stacking spectra of many galaxies (Shapley et al. 2006). While the composite spectra revealed the range of rest-frame UV spectroscopic properties of LBGs, the data are limited by low spectral resolution and the loss of information incurred by averaging over large samples of galaxies (Shapley et al. 2006). Strongly gravitationally lensed LBGs are a promising way to probe small physical scales. Probing nonlensed LBGs in this way is impossible given their generally small radii, faint magnitudes, and low surface brightness (Nesvadba et al. 2006).

Currently only few strongly lensed LBGs are known. Until recently, only one, cB58 at z=2.7 (Yee et al. 1996), was bright enough for detailed observations over many wavelengths. cB58 was a very exciting and important discovery, for its magnified image offered detailed study of an LBG never before possible. With a magnification of ~30, cB58, has been extensively studied, yielding detailed properties of its stellar population and interstellar medium (Teplitz et al. 2000, Pettini et al. 2002, Baker et al. 2004). Recently a strongly lensed LBG, the 8 o'clock arc, was discovered in the SDSS DR4 imaging data (Allam et al. 2007). The LBG has a spectrum and redshift similar to those of cB58, the previous record holder for brightest LBG, but is three times brighter. The 8 o'clock arc is at z=2.73 and has a

magnification factor of ~12.3. It is lensed by an LRG at z=0.38. Follow-up observations are underway.

The discovery of these strongly lensed LBGs has motivated the arc search in this thesis. While cB58 and the 8 o'clock arc were discovered serendipitously, it was hoped that a directed search would yield a larger sample of lensed LBGs. This hope has been realized.

3.3 Galaxy Models

Photometric redshifts can be used to determine a galaxy's redshift from its observed colors and galaxy type. By comparing the observed colors (i.e., u-g and g-r), to those predicted for a galaxy at a given redshift, an estimate of the redshift can be derived (Figure 3.3).

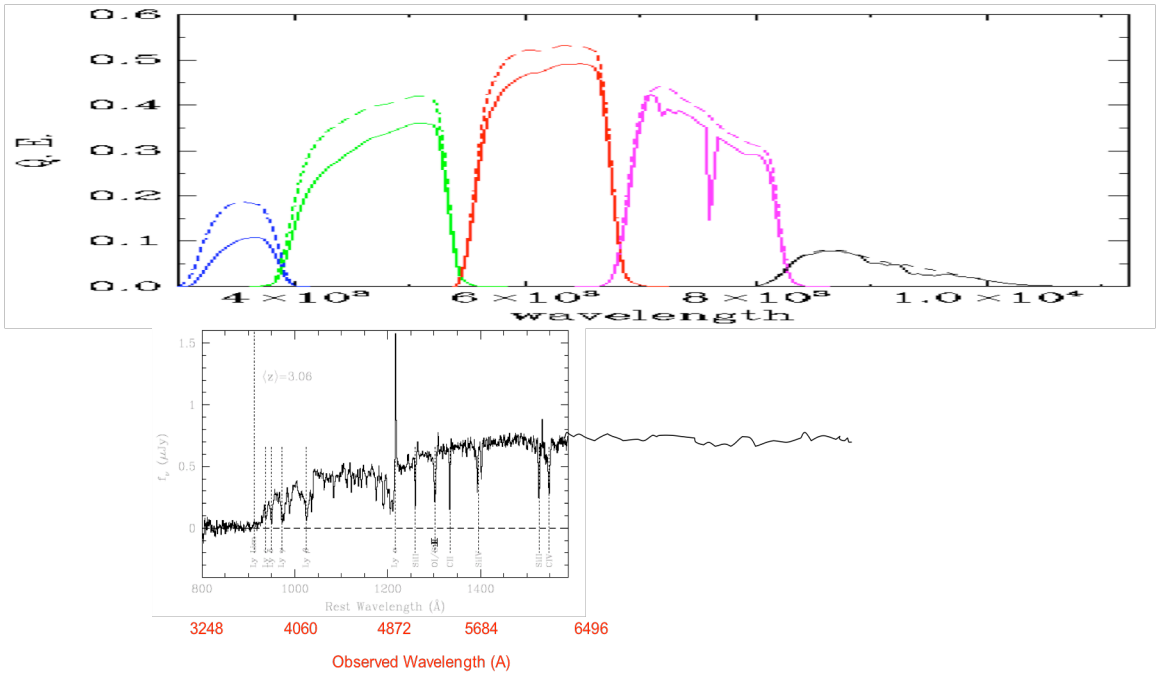

Figure 3.3 SDSS bandpasses (top) and composite spectrum of deep LBG spectra (Shapley et al. 2006) (bottom).
The horizontal axes are aligned to show where the SDSS filters straddle the break. Broadband imaging through filters that straddle the break (as u and g) provide a way to determine the redshift of galaxies.

Photometric redshifts were used to estimate the redshifts of the lensed galaxies studied in this thesis. A galaxy model for an irregular galaxy from H. Lin was used to estimate the redshifts of the lensed blue star-forming galaxies (Figure 3.4). Galaxy models exist for other types of galaxies (elliptical, spiral), but the blue galaxies detected in our search most likely match the model for an irregular galaxy. Star formation occurs in both spiral and irregular galaxies. Spiral galaxies are dominated by two visible components: a central sphere of stars called a "bulge" and a flattened disk of rotating stars. Typically the stars in the bulge have reddish colors,

while the disks tend to be bluer. The disks appear bluer, because they are the site of ongoing star formation.

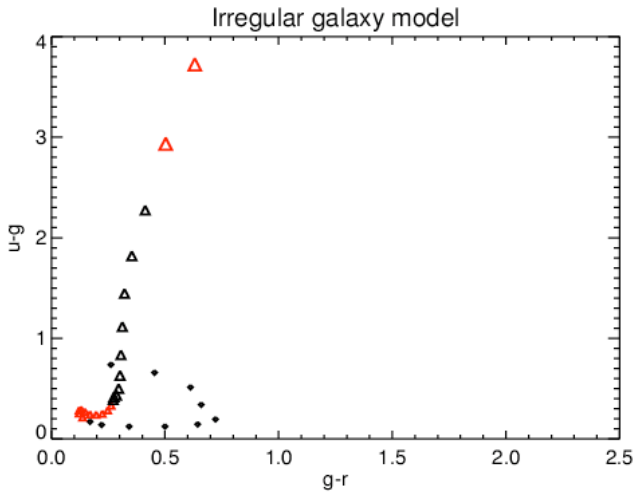

Figure 3.4 Irregular galaxy model.
Small black diamonds ($0 \le z \le 1.0$), small red triangles ($1.1 \le z \le 2.0$), larger black triangles ($2.1 \le z \le 3.0$), and large red triangles (z>3).

Irregular galaxies got their name from their asymmetrical appearance. Star formation occurs in disorganized patches that occupy a relatively large fraction of the galaxy. This is because the size and luminosity of star-forming regions increases only slowly with the size of the galaxy. Therefore, bright OB associations can be found even in small irregular galaxies (Sparke and Gallagher 2000). The blue light from these OB associations in irregular galaxies is the source of the blue color of the lensed galaxies found in our search for strong lenses.

The original galaxy model was derived from empirically measured galaxy templates by Coleman, Wu, and Weedman (1980). These are referred to as CWW templates. The templates were then extended beyond the wavelength coverage of the CWW templates into the UV and IR using the theoretical galaxy models of Bruzual

and Charlot (1993).

To apply photometric redshifts to the model, the model must include the effects of absorption by HI in the galaxy and by the intergalactic HI along the path from the galaxy to us. Madau (1995) calculated these absorption effects for high-redshift galaxies. H. Lin then applied Madau's relations, as well as the appropriate *k*-corrections, to the irregular galaxy model to predict the observed SDSS colors. The resultant model is shown in Figure 3.4. This is similar to the modeling done in the LBG survey by Steidel et al. 2003, although the effect of dust was included in their models.

CHAPTER 4

THE SEARCH ALGORITHM

"When I'm playful I use the meridians of longitude and parallels of latitude for a seine and drag the Atlantic Ocean for whales."
-*Mark Twain,* Life on the Mississippi

Strong-lensing arc systems are rare. A large search area betters one's chances of discovering new arcs. The Sloan Digital Sky Survey (SDSS), the most ambitious astronomical survey ever undertaken, offers such an area. The SDSS is a 5-year survey of the Northern sky with ½" resolution using a 2.5 meter telescope at Apache Point, NM. When completed, the SDSS will provide detailed optical images covering more than a quarter of the sky (10,000 square degrees). The SDSS will characterize about 200 million objects in five optical bands and will measure the spectra of a million objects. As the survey progresses, the data is released to the scientific community and the general public in annual increments. The most recent release is the Fifth Data Release (DR5) (Adelman-McCarthy et al. 2007).

While the large search area of the SDSS is attractive, the survey also imposes two limitations. The SDSS is a shallower survey and has poorer seeing than is typically used for arc surveys. The astronomical seeing conditions on a given night

at a given location describe how much the Earth's atmosphere perturbs the images of stars as seen through a telescope. The most common seeing measurement is the diameter (technically full width at half maximum or FWHM) of the seeing disc (the point-spread function for imaging through the atmosphere). Characteristics of the DR5 imaging area are shown in Table 4.1.

Table 4.1 Characteristics of the DR5 imaging area (Adelman-McCarthy et al. 2006)

Footprint area	8000 deg^2
Imaging catalog	217 million unique objects
AB magnitude limits	
u	22.0 mag
g	22.2 mag
r	22.2 mag
i	21.3 mag
z	20.5 mag
Median PSF width	1.4” in *r*
RMS photometric calibrations errors	
r	2%
u-g	3%
g-r	2%
r-i	2%
i-z	3%
Astrometry errors	<0.1” rms absolute per coordinate
Object counts	
Stars, primary	85,383,971
Stars, secondary	28,201,858
Galaxies, primary	131,721,368
Galaxies, secondary	33,044,047

The SDSS is a relatively shallow survey with 95% completeness limit in the *r* band of 22.2, as shown in Table 4.1 (Adelman-McCarthy et al. 2006). Most known LBGs have been discovered in deep images covering small areas of the sky. The survey by Steidel, et al. (2003), for example, contains 2347 candidate LBGs, but the survey covers only about 0.38 $\deg^2$ with a limiting magnitude 25.5.

However, the limited area of existing LBG surveys also means that the very bright end of the LBG luminosity function is unconstrained. (The luminosity function is the number of galaxies in the luminosity range $[L, L + dL]$ in a given volume.) An SDSS-based arc survey complements existing LBG imaging surveys by covering a much wider area to a brighter limiting magnitude. In the SDSS, we can find both intrinsically very luminous, but rare, LBGs, as well as intrinsically normal-luminosity, but lensed, LBGs, which are also rare.

The SDSS typically has poorer seeing than imaging typically used for arc surveys, with a median seeing of 1.4" in the *r* band (Adelman-McCarthy et al. 2006). In the gravitational lensing search by Luppino, et al. (1999), the imaging of x-ray-selected clusters had an *r* band seeing ranging from 0.5" to 1.3" FWHM with a median value of 0.8" FWHM. In the search for strong lensing in the Red-Sequence Cluster Survey (RCS), the images of clusters with arcs all had seeing better than 1" (Gladders et al. 2003). The median seeing was 0.45", with no image worse than 0.7", for a follow-up project on the RCS arc survey (Gladders et al. 2003). The imaging survey to detect strong lensing by the richest clusters selected from the SDSS used follow-up imaging from the Wisconsin Indiana Yale NOAO (WIYN)

3.5-meter telescope with a median seeing of 0.9" and from the University of Hawaii 88-inch telescope, with seeing of 0.86" and 1.13" for two different runs (Hennawi et al. 2006).

4.1 Motivation/Goal

A search algorithm was developed to select potential gravitational lensing systems from the SDSS database. The selected systems were then inspected visually to single out objects resembling arcs near a lensing galaxy.

BCGs and LRGs are massive galaxies that can strongly lens background galaxies; therefore, the regions surrounding these galaxies are likely places to look for arcs. Catalogs of 28,962 BCGs and 220,758 LRGs have been extracted from the SDSS database. These two catalogs were the basis of the arc search.

4.1.1 The BCG Catalog

The cluster catalog was constructed using the maxBCG algorithm (Koester, et al. 2007). This cluster detection technique exploits three primary features of galaxy clusters. The first is the spatial clustering of galaxies in clusters. The second is that the most luminous cluster galaxies inhabit a tight sequence in the color-magnitude diagram, the so-called “E/S0 ridgeline.” The galaxies in the E/S0 ridgeline have very uniform colors and are among the reddest, brightest, and rarest

galaxies at a given redshift. With the strong 4000 A break in their rest-frame spectra, their color is tightly correlated with redshift so that color measurements have the additional advantage that they provide accurate redshift estimates.

The third and last feature is that there often exists a unique brightest cluster galaxy (BCG) that resides in the E/S0 ridgeline, is typically coincident with the center of the galaxy distribution, and is nearly at rest relative to the center. BCGs in rich clusters usually take the form of giant elliptical galaxies, so large that they are only found at the centers of galaxy clusters. Thus, they provide important additional information about cluster locations and redshifts.

These features are used to form a likelihood function which is redshift-dependent. Individual objects in an input photometric galaxy catalog are evaluated at an array of redshifts with this function to assess the likelihood that they are BCGs living in an overdense environment consisting of red-sequence galaxies with a small dispersion in color (Koester et al. 2007). BCGs are also rough standard candles, which makes up part of the likelihood function.

The cluster catalog used in this work was extracted from the SDSS galaxy catalog using an earlier version of the maxBCG algorithm (Hansen et al. 2005).

4.1.2 The LRG Catalog

SDSS LRGs are selected on the basis of color and magnitude to yield a sample of luminous intrinsically red galaxies that extends fainter and farther than the

SDSS main galaxy sample. (The main spectroscopic galaxy sample of the SDSS is a reddening-corrected r-band magnitude limited sample of galaxies brighter than r = 17.77, with an estimated surface density of 92 galaxies per square degree [Strauss et al. 2002]). LRGs are selected using a variant of the photometric redshift technique and are meant to comprise a uniform, approximately volume-limited sample of objects with the reddest colors in the rest frame (Eisenstein et al. 2001).

In the SDSS catalog of galaxies, a flag is set if the galaxy meets the requirements of an LRG. The simplest prescription for using the LRG sample is to select objects with the GALAXY_RED flag (Eisenstein et al. 2001). The LRG catalog used in this study was extracted from the SDSS catalog using a query stipulating the condition

$$(g.primtarget \ \& \ 0x00000020) > 0.$$

This is equivalent to selecting all those galaxies with the GALAXY_RED PrimTarget flag set.

4.1.3 The Arc Search Query

Visually inspecting all of the galaxies in the two catalogs for nearby arcs would be very time consuming. A query was developed to select only those BCGs and LRGs with nearby objects (potential arcs) that have characteristics of the star-forming galaxies we are especially interested in, making a visual inspection manageable.

The magnitudes in the SDSS database are given in f_υ. As explained in Section 3.1.1, for a star-forming galaxy, approximately equal magnitudes, *m*, should be observed through the green (*g*), red (*r*), and near infrared (*i*) filters: $m_g \cong m_r \cong m_i$. The algorithm, $m_g - m_r < 1$ and $m_r - m_i < 1$, was implemented in the query to select only those BCGs and LRGs with nearby objects that are blue in an effort to find lensed galaxies with flat spectra, i.e., star-forming galaxies. Such selections on color are termed *color cuts.*

The search radius was influenced by the geometry of the prototype lensed Lyman break system, "cB58". In cB58, the image of the lensed Lyman break galaxy is located 6" from the brightest cluster galaxy of the cluster M1512+36 (Yee et al. 1996). We chose a search radius roughly twice the separation in cB58. Therefore, the query specified that the potential arcs must be within 10" of the BCG or LRG. This criterion resulted in a good initial sample of candidate arcs.

In galaxy cluster environments, lensed images would typically be located at larger distances from the lens. This is because larger Einstein radii are associated with larger lens masses. Future queries can be done with a larger search radius, but this larger search area will result in more objects returned. Hence, more time will be needed to inspect the data.

4.2 Details

The SDSS catalog data is stored in a commercial relational database management system, Microsoft's SQL (Structured Query Language) Server. The Catalog Archive Server (CAS) provides access to the object catalogs and related data. It is a companion to the Data Archive Server (DAS), which allows users to download raw (FITS) images and spectra from the survey. The SDSS SkyServer provides a web interface to the CAS. The database can be searched via the SkyServer interface. The SkyServer provides Internet access to the public SDSS data for both astronomers and for science education (http://cas.sdss.org/dr5/en/).

The raw data gathered by the telescope at Apache Point is fed through data analysis software pipelines at Fermilab. Imaging pipelines analyze data from the imaging camera to extract about 400 attributes for each celestial object along with a three-color (g, r, i) cutout image. The spectroscopic pipelines analyze data from the spectrographs to extract calibrated spectra, redshifts, absorption and emission lines, and many other attributes.

After calibration, the pipeline output is available to the astronomers in the SDSS consortium. After approximately a year, the SDSS publishes the data to the astronomy community and the public.

Both the structured data and the images are stored in the SQL database. The SkyServer provides both a text and a GUI SQL interface to mine the SDSS database.

A point-and-click pan-zoom feature lets users pan across a section of the sky and select objects and their spectra (if available).

SQL queries can be used to extract a subset of the data. A query is a request for information. One can specify the desired data and what conditions the data must satisfy. For example, one might ask the database to return the positions of all stars brighter than a certain magnitude.

A basic SQL query consists of three parts:

1. A SELECT clause, which specifies the parameters to retrieve;
2. A FROM clause, which specifies the database tables to extract the data from;
3. A WHERE clause, which specifies the constraints placed on the extracted data.

We used slightly more sophisticated queries (one for the BCGs and an analogous query for the LRGs), incorporating one of the SkyServer's stored procedures termed a “neighbors search.” A procedure takes a number of parameters and executes a previously defined sequence of commands. The neighbors search procedure (spGetNeighborsRadius) is a macro that searches for objects around every object in a table, given a certain search radius.

In our case, the SELECT clause specified the lensing galaxy's ID number, coordinates, and the potential arc's magnitudes. The information in the database is stored in tables, organized in columns and rows. A view is a special subset of a table. In this case, the Galaxy view is comprised of all the galaxies in the PhotoPrimary table. The PhotoPrimary table is comprised of all unique, or primary survey objects.

In the FROM clause, we specified the input tables that contained the list of BCGs or LRGs and specified searching the database's Galaxy view (to ensure that the potential lensed objects found were galaxies, not stars or quasars, for example).

The WHERE clause specified the search radius (in arcminutes) and the magnitude cuts of the search algorithm.

The LRG query follows:

```
# Create table of input galaxies, radii, ids to be used by the spGetNeighborsRadius search
# procedure

CREATE TABLE #UPLOAD(

up_ra FLOAT,

up_dec FLOAT,

up_rad FLOAT,

up_id int)

# Insert the values from the LRG catalog into the table created

INSERT INTO #UPLOAD

SELECT

m.ra AS UP_RA,

m.dec AS UP_DEC,

# Set the search radius at 10" = 0.17'

0.17 as UP_RAD,

m.int_id AS UP_ID

# Use the LRG catalog as input

FROM mydb.LRGs_1  m

CREATE TABLE #tmp (

up_id int,

objid bigint)
```

```
INSERT INTO  #tmp

# Call the Neighbors Search stored procedure

EXEC spGetNeighborsRadius

INSERT INTO mydb.LRGs_1_output

# List object parameters to be returned with the object i.e. objects coordinates and

magnitudes

SELECT

m.int_id, m.objid, m.ra, m.dec, g.objid, g.ra, g.dec, g.dered_u, g.dered_g, g.dered_r, g.dered_i,

g.dered_z,

radius_calc=3600*sqrt((power((cos(radians(m.dec)))*(m.ra-g.ra),2))+(power((m.dec-g.dec),2)))

# Indicate the name of the LRG catalog and that the returned objects should come from
the galaxy
# table; t, m, and g are nicknames for tmp, mydb.LRGs_1, galaxy

FROM #tmp t, mydb.LRGs_1 m,  galaxy g

WHERE

 t.up_id = m.int_id AND

# Select only objects that are galaxies

g.objid=t.objid AND

# Select objects with flat spectra

(g.dered_g-g.dered_r)<1.0 AND

(g.dered_r-g.dered_i)<1 AND

# Do not include the LRG in the returned objects

g.objid <> m.objid
```

4.3 Results

A total of 8459 BCGs (out of 28,962) with potential arcs and a total of 49,026 LRGs (out of 220,758) with potential arcs were returned by the queries. This was still a daunting number of galaxies for visual inspection. To prioritize the inspection, the galaxies were sorted as a function of the number of potential arcs per galaxy. The galaxies with the most potential arcs would be inspected first.

Tables 4.2 and 4.3 show the number of potential BCG and LRG lenses as a function of the number of potential arcs.

Table 4.2. Number of potential BCG lenses.

Number of potential arcs	Number of potential BCG lenses
1	7316
2	1054
3	83
4	6
total	8459

Table 4.3. Number of potential LRG lenses.

Number of potential arcs	Number of potential LRG lenses
1	41646
2	6388
3	831
4	130
5	23
6	5
7	2
8	0
9	0
10	0
11	1
total	49026

CHAPTER 5

ARC IDENTIFICATION

"Mama always told me not to look into the eyes of the sun,
But mama, that's where the fun is."
-Manfred Mann, "Blinded by the Light"

Two criteria must be met for a detected object to be identified as an arc produced by gravitational lensing. The arc must have the correct morphology. Arcs are extended objects with some separation from the lensing galaxy. Second, the arc must be more distant than the lensing galaxy.

For multiple objects detected near the BCG or LRG to be multiple images of the same source, they must all have the same redshift and their geometry must be permitted by lensing theory.

5.1 The Photo Pipeline

The imaging data from the telescope is sent into various pipelines: spectroscopic data into the spectroscopic pipeline, monitor telescope data into the monitor pipeline, and imaging data into the astrometric, photometric, and target

selection pipelines. A pipeline is a computer program that processes digitized data automatically to extract certain types of information. The term "pipeline" connotes the automated nature of the data processing; the data "flow" through the pipelines with little human intervention. Information about stars, galaxies and quasars comes out of the pipelines and is made accessible via the SDSS database.

The objects returned by the query had been defined as separate objects in the database by the photometric pipeline (Photo). Photo turns the imaging data into information about the celestial objects. One of the jobs of Photo is to decide if an initial single detection is in fact a blend of multiple overlapping objects, and, if so, to separate, or *deblend* them. The deblending process is challenging, for it must work on objects with a multitude of sizes and morphologies, so the deblending process is not perfect.

It is the job of the visual inspector to decide whether the objects returned by the query are in fact objects separate from the central BCG or LRG and, if so, whether they could be arcs produced by gravitational lensing.

5.2 Visual Inspection

The visual inspection relied primarily on the morphology and the geometry of the objects. Arcs were identified in the images by their elongated shapes and blue color. Although redshift is important, this criterion was deferred to the more detailed analysis of those arcs that passed the visual inspection.

The arc candidates returned by the query were visually inspected by four individuals. Two of the inspectors, Huan Lin and Jeff Kubo, are experienced astronomers with a good eye for differentiating arcs from objects not formed by lensing. They taught two newcomers to the field, Tom Diehl and me, how to recognize the morphology and geometry of true arcs.

The candidates were viewed as color thumbnails created with the SDSS CAS image list web tool. Objects could be singled out to be viewed in a larger format. The image list tool provides an option to have circles drawn around the objects selected by the Photo.

5.2.1 Morphology

Visually, the arcs would appear bluer than the central LRG or BCG. This is because they are star-forming galaxies whose light is strongly dominated by the very luminous blue stars while the LRGs and BCGs are early type galaxies comprised primarily of older, redder stars. This was the criteria set in the query, so most objects returned by the query near the BCG or LRG would be blue. Any objects that were not blue were not arc candidates.

The blue objects should look arc-like or at least be extended. For simplicity, we did not attempt to use any morphological criteria (i.e., arc-like objects) in our query, so this requisite for flagging an arc must be checked for by the inspectors.

Point sources, like quasars, create more compact images while the extended emission typical of a star-forming galaxy (or host galaxy of the quasar) will appear more arc-like or even form a ring. The difference between the image from a point source and extended emission can be seen in the image of a quasar shown in Figure 5.1. The image shows two images of a quasar, along with a ring from part of the extended emission of the quasar. We do not expect any images from quasars, because the query specified only objects that are galaxies be returned.

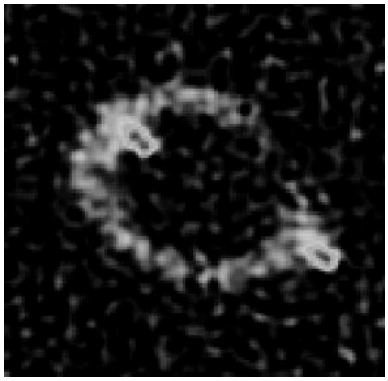

Figure 5.1 This figure shows the first discovered example of an Einstein ring, discovered by Hewitt et al. (1988) using the Very Large Array (VLA) radio telescope.

Examples of objects masquerading as arcs that were retuned by our query are shown in Figures 5.2-5.4 In each case, the image on the top is shown without the Photo objects circled.

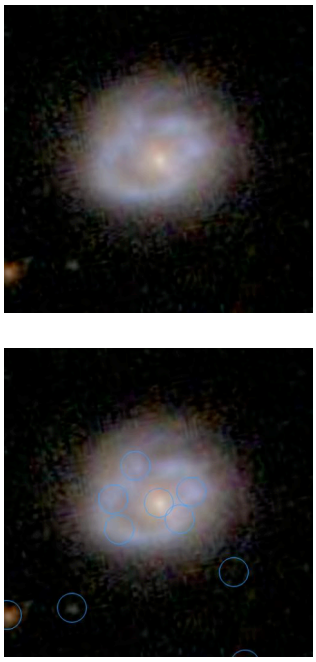

Figure 5.2 HII and star forming knots masquerading as arcs.

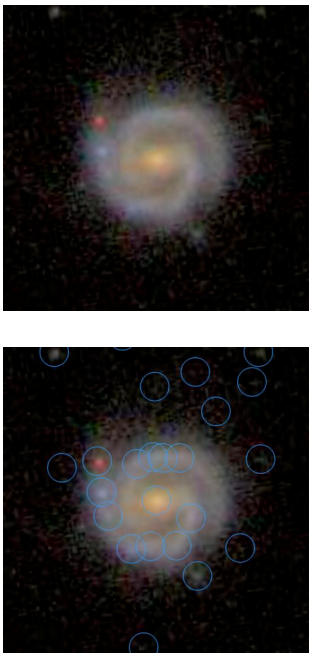

Figure 5.3 Example of spiral arms masquerading as arcs.

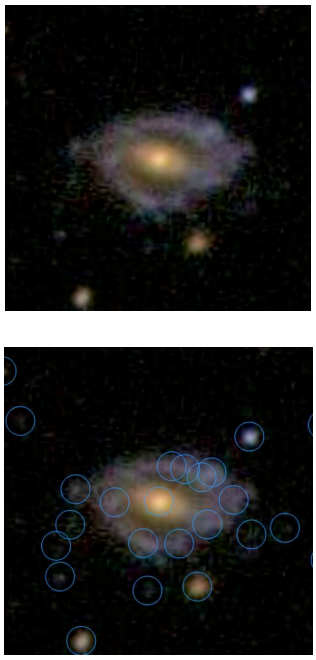

Figure 5.4 Example of spiral bars masquerading as arcs.

Fourteen of the 1081 potential lensing systems inspected by all four inspectors were selected as candidate lensing systems. Objects that show some connection to the central galaxy are not likely arcs. Among these objects are star forming knots and HII regions of spiral galaxies, the connecting bars of barred spiral galaxies, edge-on spirals, or colliding galaxies.

The HST image (Figure 5.5) of the core of the galaxy NGC 253 shows an exceptionally high rate of star formation. In the center are dense knots of stars surrounded by glowing gas and dust lanes. The color is a combination of the light emitted from the young, hot, blue stars and their associated emission and reflection nebulae. Because these nebulae are predominantly ionized hydrogen, they are called HII regions. The hydrogen is ionized by the UV light emitted by the hot, bright, massive pre-main-sequence O and B stars, called OB associations. Photons are emitted as the electrons and protons recombine. Particularly prominent is the emission produced by the transition from the n=3 to the n=2 state, which produces H_α photons at 656 nm in the red portion of the spectrum. Nebulae often appear green, because they also contain oxygen gas which has a green emission line at 501 nm. Because the eye is more sensitive to green than red, the dimmer oxygen line appears brighter to us than the H_α line. The light from the bright stars may also be reflected by the large amount of dust in star-forming nebulae. The size of the dust grains causes blue light to be reflected more efficiently than red light, so reflection nebulae frequently appear blue in color.

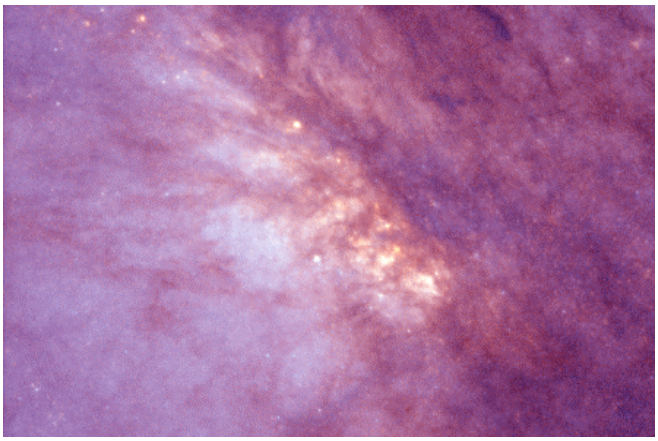

Figure 5.5 HST image of a star-forming region of NGC 253.

5.3 Results, Pretty Pictures

The systems returned by the query were sorted as a function of the number of blue objects found within the 10" radius. As shown in Tables 4.2 and 4.3, the greater the number of potential arcs, the fewer the number of potential lenses. All four inspectors reviewed the candidate lensing systems with three and four potential arcs. Any candidate highlighted by two or more inspectors was marked for further study. There were 6388 systems with two potential arcs (as shown in Table 4.3). Visual inspection of such a large number of images is a huge undertaking. Fortunately, one inspector, H. Lin, looked at this list and found lensing system lrg_2_2811.

The 14 systems marked for further study are listed in Table 5.1, and the 14 corresponding images created with the CAS image list tool (which we used for the visual inspection) are shown in Figures 5.6–5.19. The naming convention is:

(catalog)_(number of potential arcs)_(id number of BCG/LRG).

Table 5.1 List of arc candidates selected for follow-up study.

Name	ra	dec
lrg_3_364	117.161000	45.6575
lrg_3_028	120.349000	45.5995
lrg_4_606	135.011636	22.567678
lrg_3_817	135.343000	18.2423
bcg_3_067	148.167603	34.579469
lrg_4_581	159.681640	48.821597
bcg_3_109	162.429763	44.343192
lrg_3_757	177.138000	19.5009
lrg_3_810	186.828000	17.4311
lrg_3_629	220.386000	-0.899518
lrg_3_227	227.828000	47.2279
lrg_3_651	264.111000	32.4167
lrg_4_670	339.630476	13.332181
lrg_3_139	343.093000	1.11667

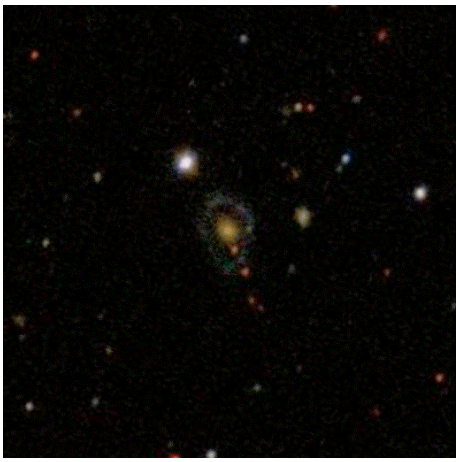

Figure 5.6 lrg_3_651.

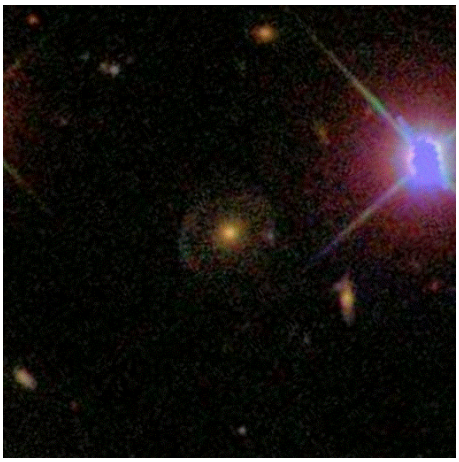

Figure 5.7 lrg_3_28.

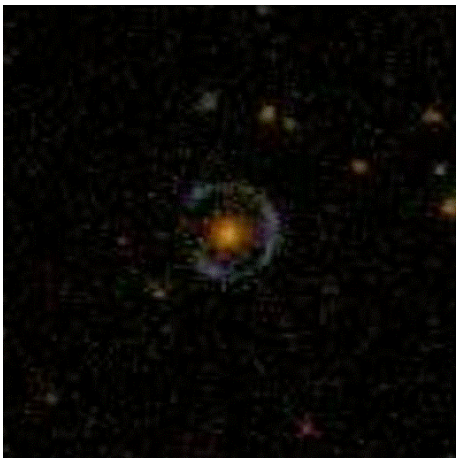

Figure 5.8 lrg_3_757.

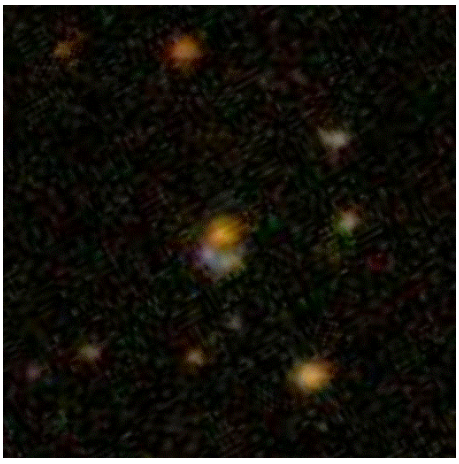

Figure 5.9 lrg_3_364.

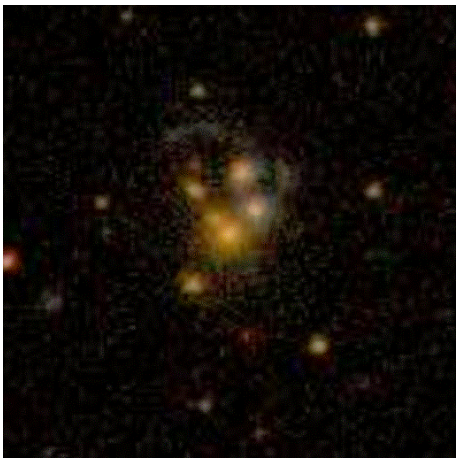

Figure 5.10 lrg_3_810.

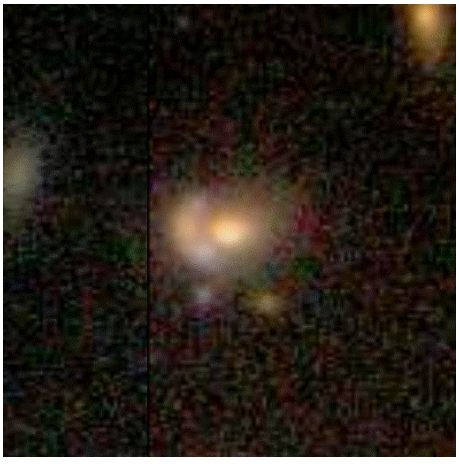

Figure 5.11 lrg_3_139.

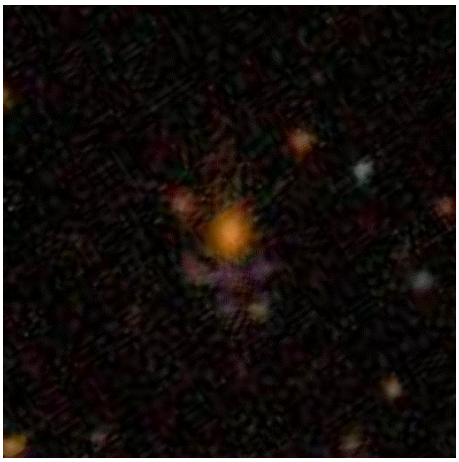

Figure 5.12 lrg_3_227.

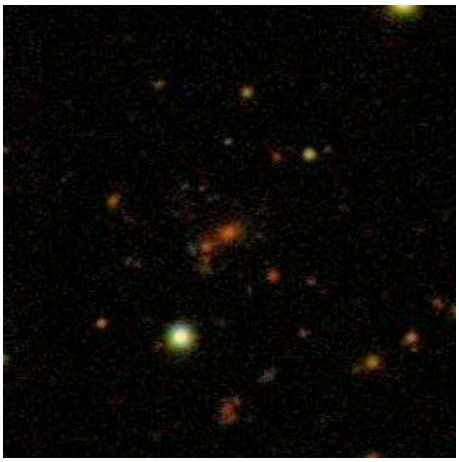

Figure 5.13 lrg_3_629.

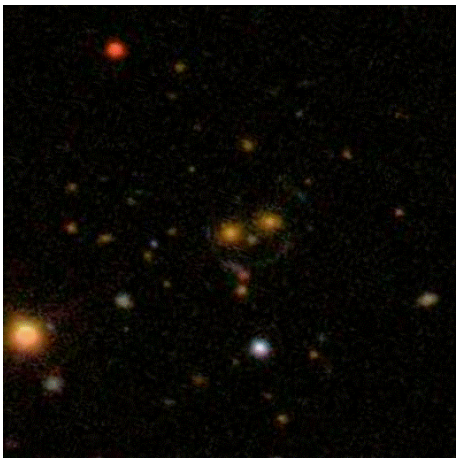

Figure 5.14 lrg_4_581.

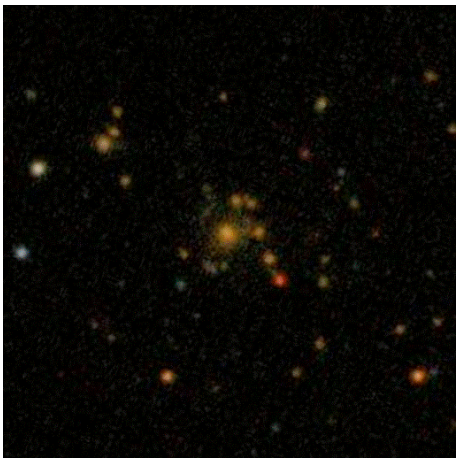

Figure 5.15 lrg_3_817.

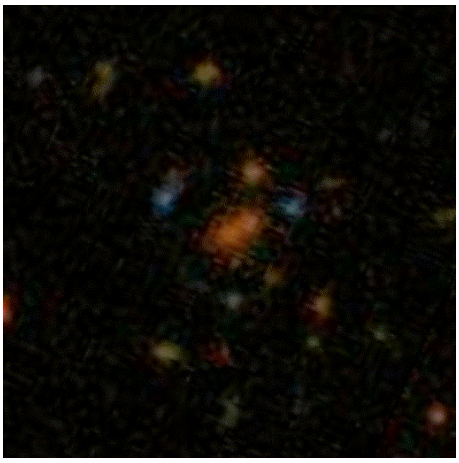

Figure 5.16 lrg_4_606.

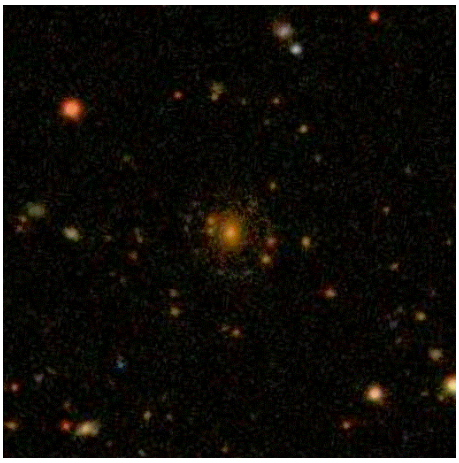

Figure 5.17 lrg_4_670.

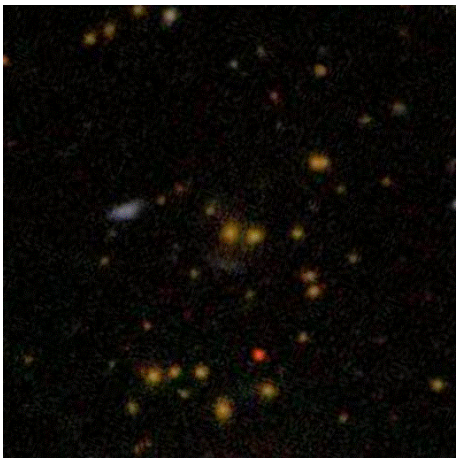

Figure 5.18 bcg_3_067.

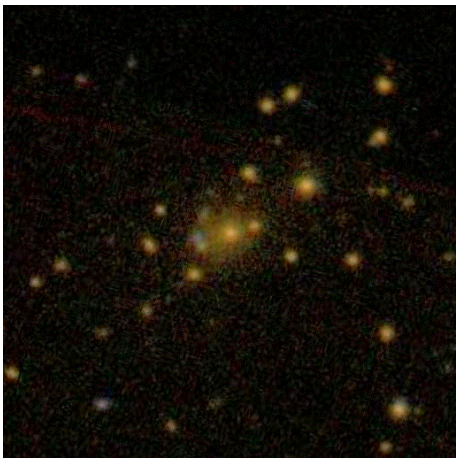

Figure 5.19 bcg_3_109.

CHAPTER 6

USING ARCS TO FIND MASS AND MASS TO LIGHT RATIOS: THE EINSTEIN RADIUS METHOD

"We always did feel the same,
We just saw it from a different point of view,
Tangled up in blue."
-Bob Dylan, "Tangled up in Blue"

Tangled up in the blue arcs and the red lenses is information about the mass and light of the lensing systems. Luminosities and redshifts of the lensing galaxies combined with the geometry and redshift estimates of the lensed blue galaxies yielded mass to light ratios for each of the gravitational lensing systems.

A technique we have dubbed "the Einstein radius method" takes advantage of the simplicity of the mass relation for an SIS lensing mass distribution (Equation 2.1 repeated here from Section 2.1):

$$\theta_E = \alpha$$

$$\theta_E = \left(\frac{4GM}{c^2} \frac{D_{ds}}{D_d D_s} \right)^{1/2}$$

$$M = \theta_E^2 \left(\frac{c^2}{4G} \frac{D_d D_s}{D_{ds}} \right). \qquad \text{Equation 2.1}$$

The Einstein radius, θ_E, can easily be determined by fitting a circle to the arcs (Figures 6.1 and 6.2). The radius along with the angular diameter distances (D_d, D_s, D_{ds}) of the lensing system can then be used to calculate the mass, *M*, inside the Einstein radius.

The light is calculated by summing the luminosities of the lensing galaxies located inside a circle of radius θ_E centered on the lensing galaxies (Figures 6.1 and 6.2).

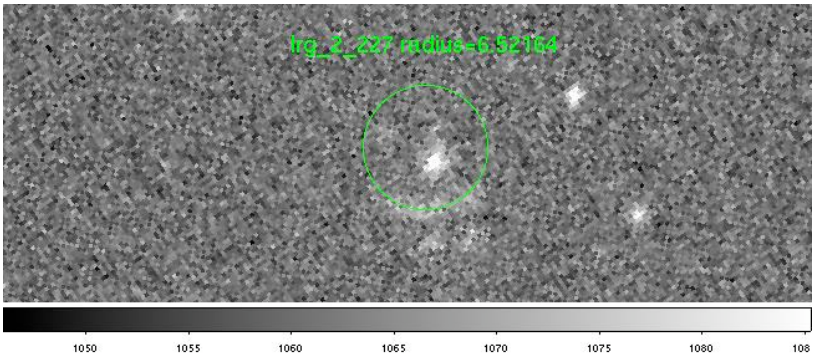

Figure 6.1 Image of lrg_2_227 showing a circle fit to the arc and the Einstein radius in units of arcseconds (viewed and measured using DS9).

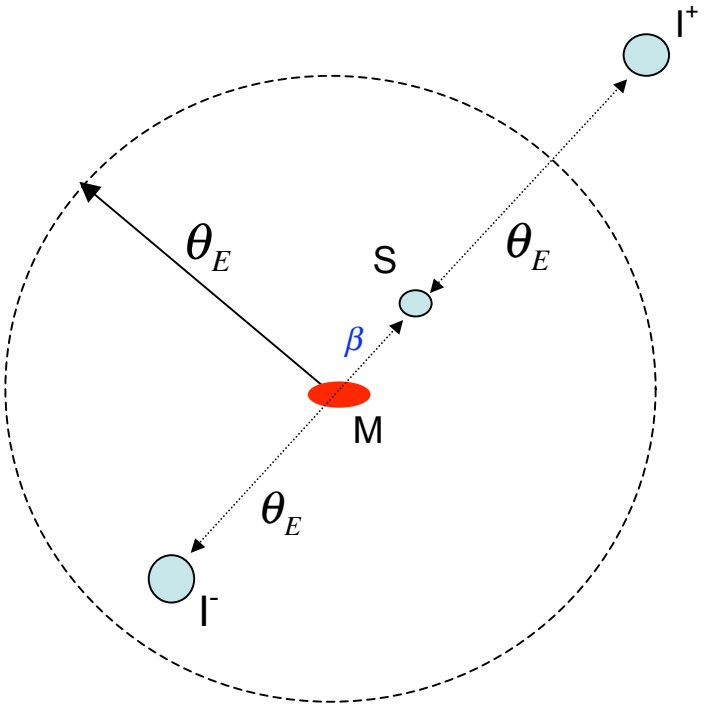

Figure 6.2 Relative locations of the source S and images I^+ and I^- lensed by an SIS mass distribution M (only center is shown). The dashed line is the Einstein ring with radius θ_E. One image is inside the Einstein ring and the other outside. Notation follows Figure 2.1 (Narayan and Bartelmann 1997).

Eight systems with morphologies most applicable to the Einstein radius method were chosen from the list of candidates for analysis. In these systems, the arcs are in a configuration suggesting a circular pattern with the lensing galaxy (or galaxies) centrally located. In one of these systems, lrg_4_581, two sets of arcs were apparent. Each set was analyzed separately (lrg_4_581a and lrg_4_581b) and each has a different central lensing galaxy, bringing the number of systems to nine. A tenth system, the 8 o'clock arc, was also included. The 8 o'clock arc was discovered serendipitously during examination of objects in a catalog of interacting/merging

galaxies (Allam et al. 2007). This system was flagged by our query in the list of potential LRG lensing systems with two arcs and would have likely been found during visual inspection. However, the team did not inspect this list, because it was comprised of 6388 potential systems (as shown in Table 4.3). Visual inspection of such a large number of images is time consuming. One inspector, H. Lin, did look at this list and found lensing system lrg_2_2811, the eleventh system chosen for analysis.

Details of the mass and light calculations for these eleven systems (Table 6.1) are discussed in the following sections.

Table 6.1 Lensing systems chosen for analysis.

lens	name	ra	dec
1	lrg_3_651	264.111233	32.416737
2	lrg_3_757	177.138102	19.500889
3	lrg_3_810	186.828089	17.431085
4	lrg_3_227	227.828076	47.227867
5	lrg_4_581a	159.677907	48.822298
6	lrg_4_606	135.011032	22.568026
7	lrg_4_670	339.630476	13.332181
8	bcg_3_067	148.167603	34.579469
9	lrg_2_2811	181.508721	51.708201
10	eight_oclock	5.670489	14.519559
11	lrg_4_581b	159.68164	48.821597

6.1 Mass

Four quantities are required to calculate the mass of the lens: the Einstein radius (θ_E), the angular diameter distance to the lens (D_d), the angular diameter distance to the source (D_s), and the angular diameter distance between the lens and the source (D_{ds}).

The method used to determine the Einstein radius is described in the following section.

The angular diameter distances are a function of redshift and cosmology. A flat, ΛCDM (Lambda Cold Dark Matter) cosmology is assumed, with $H_0=100h$ km s^{-1} Mpc^{-1}, $\Omega_m = 0.3$, and $\Omega_\Lambda = 0.7$. Determination of the lens and source redshifts is described in Sections 6.1.2 and 6.1.3, respectively.

6.1.1 Einstein Radii

The Einstein radius, θ_E, for each lensing system was found by fitting a circle by hand to the arcs using DS9. DS9 is an astronomical imaging and data visualization application. DS9 provides a tool for measuring the circle's radius. An example of a DS9 image of a circle fit to an arc was shown in Figure 6.1. DS9 images showing the Einstein radii measurements for all 11 lensing systems are shown in Appendix A.

The error is the standard deviation of 10 hand measurements of each Einstein radius.The measured Einstein radii and their errors are shown in Table 6.2

Table 6.2 Parameters required to calculate the mass.

Lensing system	Name	Lens redshift	Lens redshift error	Source redshift (weighted mean)	Minimum source redshift	Maximum source redhift	Einstein radius (arcseconds)	Error in radius (arcseconds)
1	lrg_3_651	0.3340	0.0150	2.8	2.6	3	5.87	0.26
2	lrg_3_757	0.4220	0.0090	2.15	1.5	2.5	5.00	0.11
3	lrg_3_810	0.3830	0.0070	2.45	0.9	2.7	8.15	0.19
4	lrg_3_227	0.4517	0.0003	2.5	0.9	2.7	6.52	0.2
5	lrg_4_581a	0.3890	0.0150	0.8	0.778	2.3	12.12	0.26
6	lrg_4_606	0.4891	0.0002	1.2	1	2.3	7.89	0.24
7	lrg_4_670	0.4128	0.0002	2.55	2.1	2.6	9.40	0.21
8	bcg_3_067	0.4170	0.0120	2.6	2.1	2.8	7.63	0.06
9	lrg_2_2811	0.4224	0.0002	2.7	2.6	2.8	3.79	0.19
10	eight_oclock	0.3805	0.0002	2.95	2.8	3.1	3.23	0.11
11	lrg_4_581b	0.4257	0.0003	2.65	1.2	2.9	9.37	0.15

Redshifts from SDSS and galaxy model only.

Lensing system	Name	Lens redshift	Lens redshift error	Source redshift (weighted mean)	Minimum source redshift	Maximum source redhift	Einstein radius (arcseconds)	Error in radius (arcseconds)
1	lrg_3_651	0.2600	0.0010	0.2608	0.2598	0.2618	5.87	0.26
2	lrg_3_757	0.4440	0.0020	2.382	2.38	2.384	5.00	0.11
3	lrg_3_810	0.3830	0.0070	2.45	0.9	2.7	8.15	0.19
4	lrg_3_227	0.4517	0.0003	0.9838	0.9828	0.9848	6.52	0.2
5	lrg_4_581a	0.3890	0.0150	0.8	0.778	2.3	12.12	0.26
6	lrg_4_606	0.4891	0.0002	2.032	2.03	2.034	7.89	0.24
7	lrg_4_670	0.4128	0.0002	2.55	2.1	2.6	9.40	0.21
8	bcg_3_067	0.4170	0.0120	2.6	2.1	2.8	7.63	0.06
9	lrg_2_2811	0.4224	0.0002	2.002	1.999	2.005	3.79	0.19
10	eight_oclock	0.3805	0.0002	2.73	2.728	2.732	3.23	0.11
11	lrg_4_581b	0.4257	0.0003	2.65	1.2	2.9	9.37	0.15

Redshifts from SDSS and galaxy model replaced by redshifts from follow up observation (shown in red).

6.1.2 Lens Redshifts

Spectroscopic or photometric redshifts (or both) were available for all of the lensing galaxies as shown in Table 6.3. When available, the spectroscopic redshift was used. When a spectroscopic redshift was not available, a photometric redshift was used.

Table 6.3 Lensing galaxy redshifts.
% is the percent difference with respect to the spectroscopic redshift (specz).

lens	name	specz	photoz	photoz2	photoz (%)	photoz2 (%)
1	lrg_3_651	null	0.334	0.282		
2	lrg_3_757	null	0.422	null		
3	lrg_3_810	null	0.383	null		
4	lrg_3_227	0.4517	0.44	0.344	-2.6	-23.8
5	lrg_4_581a	null	0.389	0.393		
6	lrg_4_606	0.4891	0.471	0.439	-3.7	-10.2
7	lrg_4_670	0.4128	0.404	0.355	-2.1	-14.0
8	bcg_3_067	null	0.417	0.396		
9	lrg_2_2811	0.4224	0.425	0.318	0.6	-24.7
10	eight_oclock	0.3805	0.401	0.325	5.4	-14.6
11	lrg_4_581b	0.4257	0.421	0.385	-1.1	-9.6

SDSS Data Release 5, DR5, includes two estimates of photometric redshifts for galaxies calculated by two independent techniques. The first uses a template fitting algorithm which compares the expected colors of a galaxy derived from template spectral energy distributions with those observed for an individual galaxy (Adelman-McCarthy et al. 2007). The results are listed in the CAS Photoz table which includes the estimate of the redshift, spectral type, rest frame colors, rest frame absolute magnitudes, errors for all these quantities, and a quality flag. All photometric objects have an entry in the Photoz table, so it is mandatory to check the quality flag and error characterizations when using the photometric redshifts. The Photoz quality flag is an integer describing the quality (best:5, lowest:0).

The second photometric redshift estimate uses a neural network method (Adelman-McCarthy et al. 2007). The training set consists of 140,000 SDSS photometry measurements with spectroscopic redshifts from various sources. The resultant Photoz2 table contains a photometric redshift, error, and quality flag. As with the Photoz table, the quality flag should be consulted when using the photometric redshifts. For the Photoz2 flag, 0=normal, 1=at least one of the magnitudes undetected, 2=objects with r > 20, and 3=objects where both 1 and 2 apply. The photometric redshifts for objects that have flag=1 or flag=3 are not reliable.

Redshifts from the Photoz table were available for all the lensing galaxies, but redshifts from the Photoz2 table were only available for a subset of the lenses. As can be seen in Table 6.3, when all three redshifts were available, the Photoz redshifts agree better (-0.6% average difference) with the true spectroscopic redshifts than did the Photoz2 redshifts (-16.2% average difference). For this reason, for all cases in which a spectroscopic redshift was not available, the redshift from the Photoz table was used.

Note: The inconsistency between Photoz2 and spectroscopic redshifts is not seen for all ranges of redshift. However, at the redshifts of the lensing galaxies in this study ($z \cong 0.4$), Photoz2 redshifts appear to be biased low when compared to spectroscopic redshifts in spite of the fact that none of the Photoz2 flags (displayed in Table 6.4) indicated a problem.

Table 6.4 Lensing galaxy redshifts, redshift errors, and flags.
(*Null* indicates that no data for this parameter exists in the database.)

lens	name	specz	specz_error	specz_conf	photoz	photoz_error	photoz_quality	photo2z	photoz2_error	photoz2_flag
1	lrg_3_651	null	null	null	0.334	0.015	5	0.282	0.020	0
2	lrg_3_757	null	null	null	0.422	0.009	4	null	null	null
3	lrg_3_810	null	null	null	0.383	0.007	5	null	null	null
4	lrg_3_227	0.4517	0.0003	0.9912	0.440	0.008	4	0.344	0.028	0
5	lrg_4_581a	null	null	null	0.389	0.015	4	0.393	0.027	0
6	lrg_4_606	0.4891	0.0002	0.9903	0.471	0.013	4	0.439	0.027	0
7	lrg_4_670	0.4128	0.0002	0.9997	0.404	0.018	4	0.355	0.020	0
8	bcg_3_067	null	null	null	0.417	0.012	5	0.396	0.030	0
9	lrg_2_2811	0.4224	0.0002	0.9806	0.425	0.008	5	0.318	0.026	0
10	eight_oclock	0.3805	0.0002	0.9997	0.401	0.013	5	0.325	0.023	0
11	lrg_4_581b	0.4257	0.0003	0.9965	0.421	0.042	4	0.385	0.023	0

It is noteworthy that all the lensing systems found via visual inspection of the query results were of nearly the same redshift, $z \cong 0.4$, while the BCG and LRG targets span a wide range of redshifts.

6.1.3 Source Redshift Estimates

While the redshifts of the BCGs and LRGs are generally known from spectroscopy or photometry, redshifts of the candidate arcs are often not available. These sometimes faint, higher redshift objects have not been targeted (selected for spectroscopy) by SDSS. Spectroscopy requires a longer exposure time than imaging. More time must be allocated to obtaining spectra of fainter objects. Spectroscopic redshifts are generally not available in the SDSS database for galaxies with $z > 1.0$. Typically, main-sample galaxies have $z < \sim 0.3$ and LRGs have $z < \sim 0.5$.

Neither of the photometric estimates (Photoz and Photoz2) are reliable for $z > \sim 1$. The photometric redshifts degrade in accuracy for objects with $r > 20$. Not only are these potential arcs faint, they are also distant. The SDSS filters span approximately 6000 A (Chapter 2, Figure 2.8). For redshifts greater than 1.5, the

4000 Angstrom break (a spectral feature especially useful for accurate photometric redshift determination) has been redshifted out of the SDSS filters (Figure 6.3):

$$z = \frac{\Delta\lambda}{\lambda} = \frac{6000\ \text{A}}{4000\ \text{A}} = 1.5\ .$$

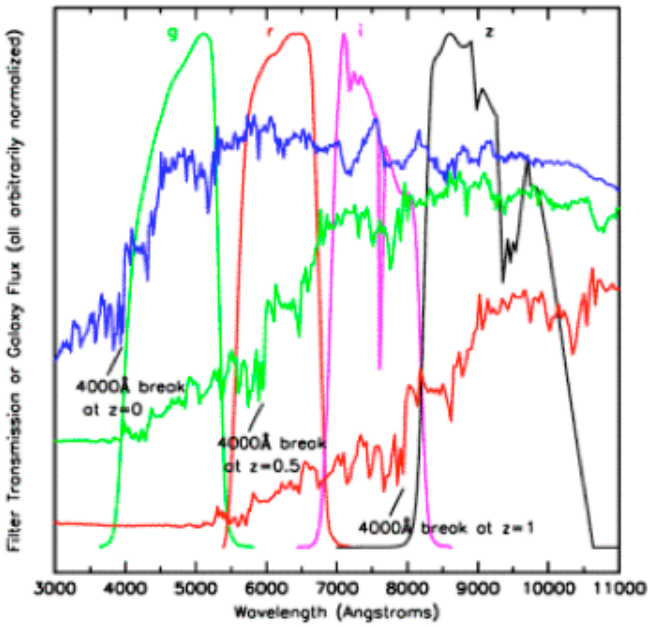

Figure 6.3 SDSS filters no longer straddle the 4000 Angstrom break for z>1.

At $z \cong 3$, the Lyman break is near the center of the u-band. However, as explained in Section 3.1, the u-band signal is weak, making it of limited use in photometric redshift determination. However, as described below, we nonetheless compare color information from the u-band and g-band to a galaxy model to estimate the source redshift.

Color cuts on $m_u - m_g$ can be used to select on redshift, using a method similar to that used to determine photometric redshifts at lower z using the 4000 Angstrom break. Broadband colors can be used to select galaxies at extremely high

(z ~3) redshifts. An actively star-forming galaxy will have a flat spectrum down to the Lyman limit of 912 Angstroms, beyond which the spectrum will be truncated by intervening absorption as was described in Section 3.2 and shown in Figure 3.3. At z=3, this spectral break has moved to the center of the u-band**.** However, at z>3.4, the Lyman limit can be confused with the 4000 Angstrom break at low z (Peacock 2003).

For several reasons, we did not incorporate such a color cut in our queries. First, the u-band signal is noisy. The shorter the wavelength, the more susceptible it is to extinction by the atmosphere.

Second, the u-band signal is weak. It is weak due to intervening line-of-sight absorption by neutral hydrogen and singly ionized helium in intergalactic clumps of highly ionized primordial gas which form the Lyman-α forest (Madau, 1995), starting near the Lyman alpha line, and getting weaker toward the bluer end of the spectrum toward the Lyman limit. Being weak, it makes the signal/noise low. Coupling a weak signal with a noisy signal would likely result in a redshift determination from a measurement of $m_u - m_g$ with a lot of error. This might result in missing, or discarding, potential lensed objects that seem to have different redshifts due to the error in our measurement that in reality have the same redshift

Third, the quantum efficiency of the CCDs is low in u-band, which results in an even lower signal/noise.

In lieu of redshift information from the SDSS database, there are three options: 1. Check the literature to see if redshifts are available for the objects.

2. Perform follow-up spectroscopy on another telescope. Follow-up photometry might also be desirable if the objects are especially faint or if it is suspected that additional arcs would be revealed with a longer exposure time. Such information could also provide useful input to lensing models. 3. Use the color information available from the SDSS and compare the colors to an appropriate galaxy model.

The NASA/IPAC Extragalactic Database (NED) was consulted for the existence of redshift information for the lensing systems. NED is built around a master list of extragalactic objects for which cross-identifications of names have been established, accurate positions and redshifts entered to the extent possible, and some basic data collected. None of the source galaxies had redshifts reported in NED**, s**o redshift estimates for each arc were found by plotting u-g and g-r for each arc on the irregular galaxy model (galaxy models are described in Section 3.3 above).

Follow-up observations (photometric and spectroscopic) have been performed for several of the lensing systems using the 3.5 meter Astrophysical Research Consortium (ARC) telescope at Apache Point Observatory in New Mexico. Spectroscopic redshifts for five of the sources and for two of the lenses were derived from these follow-up observations (Table 6.5). The source redshift obtained for lrg_3_651 rules out this system as a lensing candidate. Additionally, Masamune Oguri provided the source redshift for lrg_2_2811 from observations at the 8.2-meter Subaru telescope on Mauna Kea.

Table 6.5 Redshifts from follow-up observations.
Note that the source redshift rules out lrg_3_651 as a lensing system.

Lensing System	Redshift	Error	Follow up telescope
lrg_3_651			
LRG	0.260	0.001	ARC
source	0.261	0.001	ARC
lrg_3_227			
source	0.984	0.001	ARC
lrg_3_757			
LRG	0.444	0.002	ARC
source	2.382	0.002	ARC
lrg_4_606			
source	2.032	0.002	ARC
lrg_2_2811			
source	2.002	0.003	Subaru
8 o'clock arc			
source	2.730	0.002	ARC

These redshifts will be compared to the source redshift estimates derived using the galaxy model and to the SDSS lens redshifts. Similarly, the masses, luminosities, and mass to light ratios calculated using the follow-up observations will be compared to those calculated using the galaxy model and SDSS redshift information.

Galaxy models exist for various types of galaxies, for example, spiral, elliptical, and irregular, as shown in Figure 6.4. The irregular galaxy model most closely represents a star-forming galaxy, which is the type of galaxy expected for the source. As can be seen in Figure 6.4, the elliptical galaxy is redder than the spiral and irregular and would better represent the LRG and BCG galaxies.

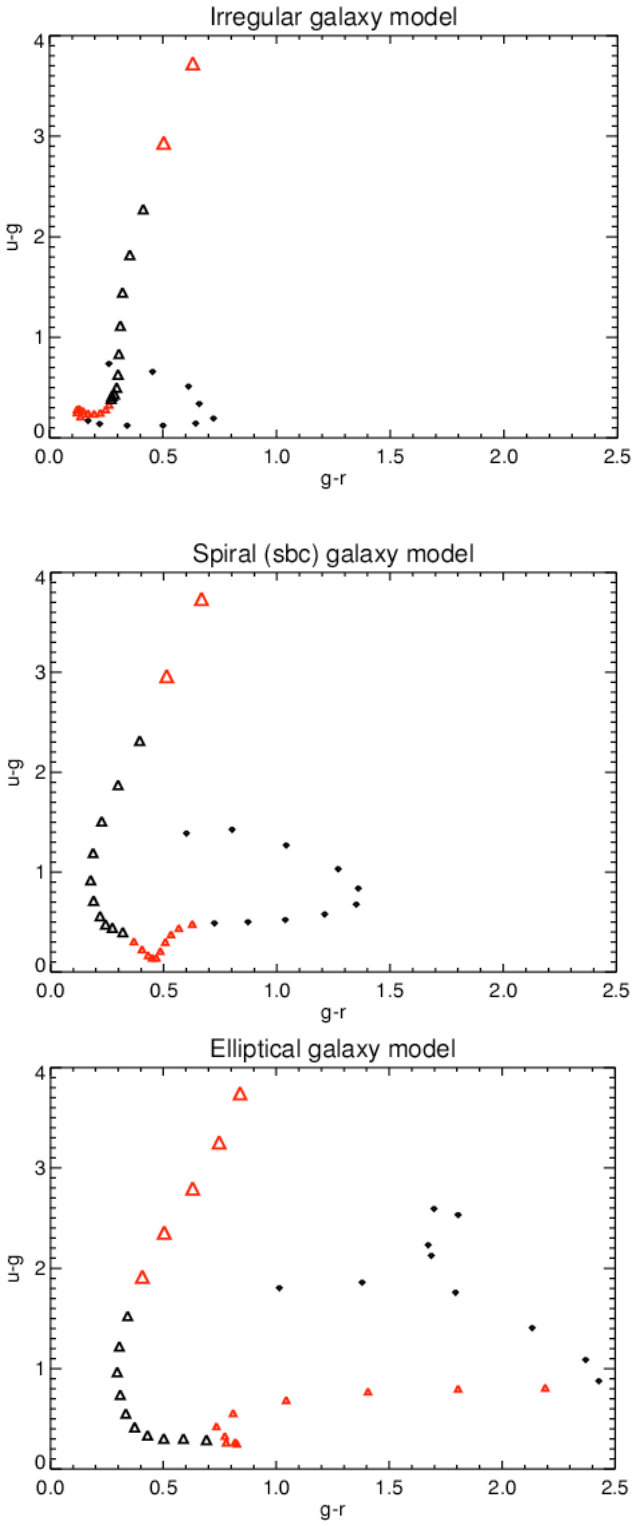

Figure 6.4 Galaxy models. Irregular (top), spiral (middle), elliptical (bottom). Small black diamonds ($0 \le z \le 1.0$), small red triangles ($1.1 \le z \le 2.0$), larger black triangles ($2.1 \le z \le 3.0$), and large red triangles (z>3).

The colors of each arc (blue object), u-g and g-r, were plotted on the irregular galaxy model. The number of blue objects observed for each lensing system is shown in Table 6.6. Plots showing the blue objects' colors plotted on the galaxy model for two of the lensing systems are shown in Figure 6.5. The plots for all the lensing systems are shown in Appendix B.

Table 6.6 Number of blue objects observed for each lensing system.

lensing system	name	number of blue objects
1	lrg_3_651	2
2	lrg_3_757	3
3	lrg_3_810	3
4	lrg_3_227	1
5	lrg_4_581a	3
6	lrg_4_606	4
7	lrg_4_670	7
8	bcg_3_067	3
9	lrg_2_2811	2
10	eight_oclock	2
11	lrg_4_581b	1

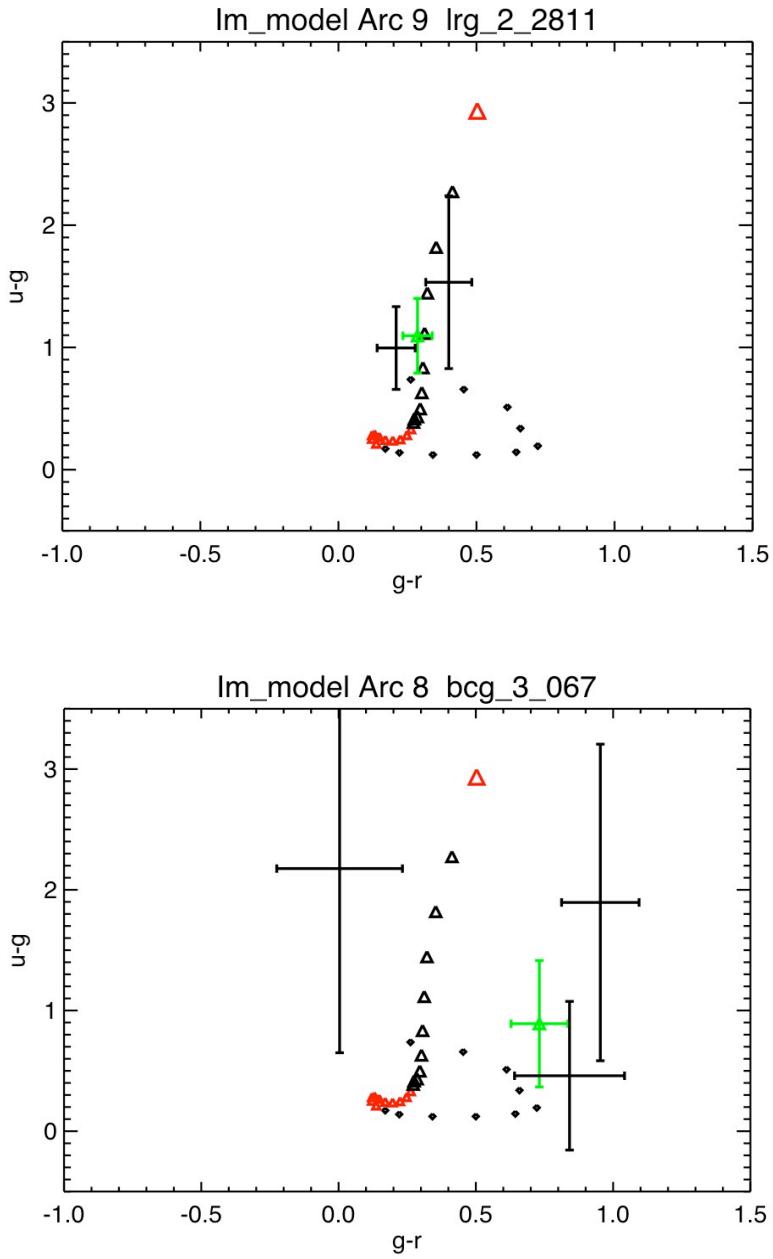

Figure 6.5 Arc colors plotted on irregular galaxy model.
Example with source color data points near the galaxy model (top).
Example with source color data points more distant from the galaxy model (bottom).
Galaxy model: small black diamonds ($0 \le z \le 1.0$), small red triangles ($1.1 \le z \le 2.0$),
larger black triangles ($2.1 \le z \le 3.0$), and large red triangle ($z=3.1$).
Black data points and error bars = colors for each source;
green data points and error bars = weighted mean of the sources.

Three difficulties associated with estimating the redshift using the galaxy model had to be addressed.

First, the source colors are not always coincident with the galaxy model. In some cases, such as lrg_2_2811 (Figure 6.5, top), the colors lie near the galaxy model, so it is easy to identify the corresponding redshift. However, the source colors for most of the lensing systems were displaced horizontally from the galaxy model as seen in the plot for bcg_3_067 (Figure 6.5, bottom). This can be attributed to two causes. First, reddening corrections due to dust in the source galaxy have not been applied to the model; doing so would make the model colors more red (Steidel et al. 2003). Second, there is a fairly large error in the source colors, which is shown by the error bars for u-g and g-r. For cases like bcg_3_067, the source redshift was assumed to be that of the corresponding u-g of the model and independent of g-r.

The second issue posed by the galaxy model was the inconsistency of the arc colors. All of the arcs for a lensing system must have the same redshift, for they are lensed images of the same galaxy. Yet the plotted colors for the arcs are displaced vertically, indicating different redshifts. Again, the sources are faint, so there is a lot of error in the color. The u-band signal is particularly noisy, the signal is weak, and the quantum efficiency of u-band is low for the SDSS CCDs, as was explained in more detail in Section 3.3.3. To help alleviate this problem in determining the redshift, the weighted mean of the colors of each arc, μ_{u-g} and μ_{g-r}, was calculated

$$\mu_{u-g} = \frac{\sum (x_i / \sigma_i^2)}{\sum (1/\sigma_i^2)},$$

where each data point x_i in the sum (in this case, $u_i - g_i$) is weighted inversely by its own variance σ_i^2:

$$\sigma_i^2 = u_{i,error}^2 + g_{i,error}^2 .$$

The uncertainty of the weighted mean, σ_μ, is

$$\sigma_\mu^2 = \frac{1}{\sum (1/\sigma_i^2)} .$$

The individual sources with error bars are plotted in black. The weighted mean with its error is shown in green in Figure 6.5. The redshifts corresponding to the weighted mean and the redshifts corresponding to the minimum and maximum error (i.e., the minimum and maximum extent of the error bars) of the weighted mean are shown in Table 6.2 (top). Also shown are the lens redshifts and their errors. In Table 6.2 (bottom) the redshifts available from follow-up observations replace those from the SDSS and the galaxy model. These are shown in red.

The third problem posed by the galaxy model method was that some values of u-g were degenerate; they could correspond to a low redshift (0<z<1.0, the small black diamonds in the galaxy model) or a higher redshift (1.0<z<2.5, the small red triangles and several of the large black triangles). This was reconciled by noting that the redshift of the source must be greater than that of the lens, so the higher redshift should be chosen. Additionally, not only does the source have to be at a higher redshift than the lens, but it can be shown that the most likely location for a

source is at twice the redshift of the lens (Turner et al. 1984), and we adopt that as the minimum source redshift needed.

6.1.4 Mass Calculations

The mass interior to the Einstein radius was calculated for each of the eleven lensing systems using the angular diameter distances corresponding to each of the three redshifts derived from the galaxy model (minimum, maximum, and weighted mean). It can be seen from Figure 6.6 that, in most cases, the mass is not a strong function of D_s/D_{ds}. (recall Equation 2.1 for the mass).

The error bars are substantially reduced for those systems with follow-up data. It is interesting to note that the masses derived using the redshift estimates from the galaxy model are consistent with the masses derived from the more accurate spectroscopic redshifts obtained for the follow-up observations, an indication of the viability of the galaxy model method.

This can be understood from a plot of the redshift dependence of D_s/D_{ds} (Figure 6.7). For source redshifts greater than ~2, the ratio decreases very slowly with redshift. This is the redshift range of all but four of the source redshifts (Table 6.5)

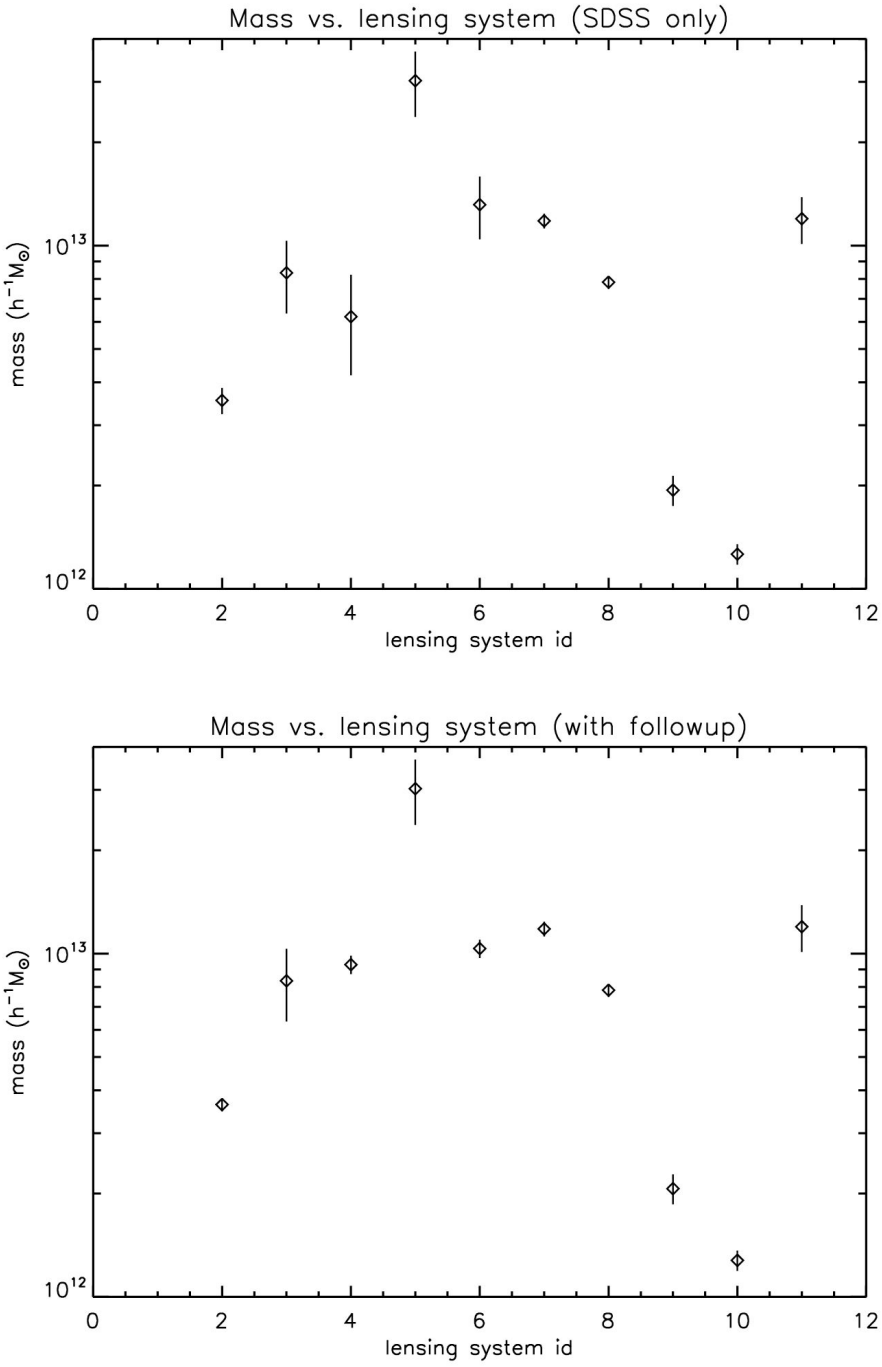

Figure 6.6 Calculated masses for each lensing system.
Using SDSS data only (top), SDSS and follow-up data (bottom).
The error bars for the follow-up data are smaller (bottom).
There was no follow-up data for lensing systems 3, 5, and 11.

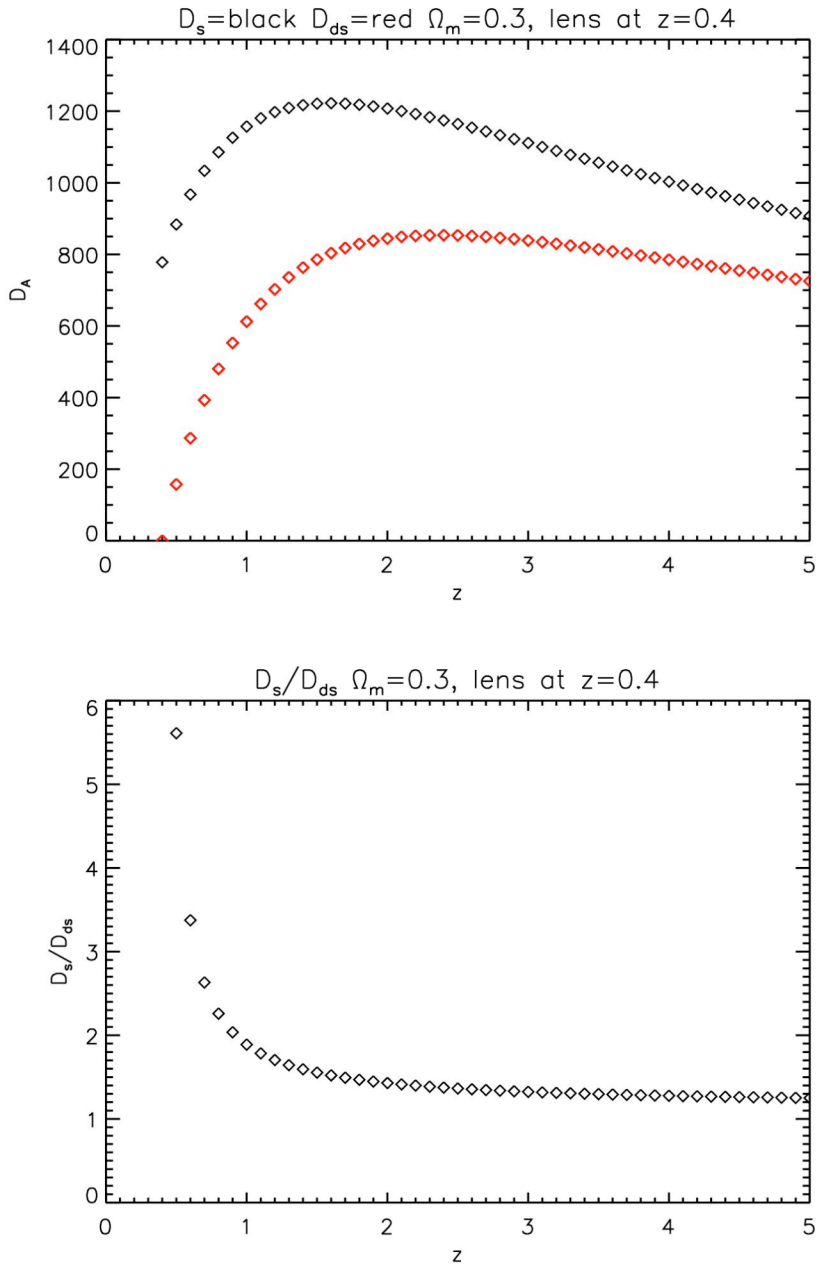

Figure 6.7 Plots of the angular diameter distance for the distance to the source, D_s, and the lens-to-source distance, D_{ds} (top), and the ratio of D_s/D_{ds} (bottom).

The mass is a function of the square of the Einstein radius (Eq. 2.1). As shown in Figure 6.6, the largest mass corresponds to lensing system 5 (lrg_4_581a), the lensing system with the largest Einstein radius.

6.1.5 Errors in the Mass

The errors were calculated via propagation of errors:

$$\sigma_x^2 \simeq \sigma_u^2 \left(\frac{\partial x}{\partial u} \right)^2 + \sigma_v^2 \left(\frac{\partial x}{\partial v} \right)^2 + \ldots$$

where x=*f(u,v)* and *u* and *v* are uncorrelated. In our case, the mass is related to the redshifts, *z*, through the angular diameter distances, D_A, which are rather complicated functions of *z* as shown in Section 2.2.3. Additionally, some of the errors are asymmetric, i.e., the errors on z_{source}. Therefore, for simplicity, we approximated the errors for the mass, luminosity, and mass to light ratios, *M/L*, with the relations shown below and in the following sections.

The errors in the mass, *M*, were calculated as follows:

$$\sigma_M^2 = \sigma_{M,\theta_E}^2 + \sigma_{M,z_{lens}}^2 + \sigma_{M,z_{source}}^2$$

where

$$\sigma_{M,\theta_E} = \left| \frac{M(\theta_E + \theta_{E\_error}) - M(\theta_E - \theta_{E\_error})}{2} \right|$$

$$\sigma_{M,z_{lens}} = \left| \frac{M(z_{lens} + z_{lens\_error}) - M(z_{lens} - z_{lens\_error})}{2} \right|$$

$$\sigma_{M,z_{source}} = \left| \frac{M(z_{source\_maximun}) - M(z_{source\_\min imum})}{2} \right|.$$

θ_{E_error} is the standard deviation of 10 hand measurements of the Einstein radius using DS9. $\sigma_{M,z_{source}}$ affects the mass through the dependence of the angular diameter distances, D_s and D_{ds}, on source redshift.

The masses and associated errors due to the error in the radius, the lens redshift, and the source redshift are shown in Table 6.7. The systems with the largest errors due to the radius measurement are those in which the arcs were too faint, too short, or too few to easily fit to the arc of a circle. The uncertainty in the lens redshifts contributes most to the mass errors for systems without spectroscopic lens redshifts (lrg_3_810, lrg_4_581a, and bcg_3_067), and the uncertainty in the source redshifts contribute most to the mass errors for systems without spectroscopic source redshifts (lrg_3_810, lrg_4_581a, bcg_3_067, lrg_4_670, and lrg_4_581b). Note, follow-up observations ruled out lrg_3_651 as a lensing system.

Table 6.7 Masses and errors.

Lensing system	M ($h^{-1}M_{\odot}$)	σ_M ($h^{-1}M_{\odot}$)	σ_{M,θ_E} ($h^{-1}M_{\odot}$)	$\sigma_{M,z_{lens}}$ ($h^{-1}M_{\odot}$)	$\sigma_{M,z_{source}}$ ($h^{-1}M_{\odot}$)
lrg_3_651	3.73E+12	3.66E+11	3.31E+11	1.53E+11	3.46E+10
lrg_3_757	3.54E+12	3.09E+11	1.56E+11	7.37E+10	2.57E+11
lrg_3_810	8.34E+12	1.99E+12	3.89E+11	1.43E+11	1.95E+12
lrg_3_227	6.21E+12	2.02E+12	3.81E+11	3.34E+09	1.98E+12
lrg_4_581a	3.02E+13	6.49E+12	1.30E+12	1.97E+12	6.05E+12
lrg_4_606	1.32E+13	2.73E+12	8.01E+11	7.56E+09	2.61E+12
lrg_4_670	1.18E+13	5.90E+11	5.28E+11	5.45E+09	2.65E+11
bcg_3_067	7.83E+12	3.33E+11	1.23E+11	2.09E+11	2.29E+11
lrg_2_2811	1.94E+12	1.95E+11	1.95E+11	9.83E+08	1.28E+10
eight_oclock	1.26E+12	8.66E+10	8.61E+10	5.18E+08	9.12E+09
lrg_4_581b	1.20E+13	1.86E+12	3.84E+11	6.90E+09	1.82E+12

Using SDSS data only.

Lensing system	M ($h^{-1}M_{\odot}$)	σ_M ($h^{-1}M_{\odot}$)	σ_{M,θ_E} ($h^{-1}M_{\odot}$)	$\sigma_{M,z_{lens}}$ ($h^{-1}M_{\odot}$)	$\sigma_{M,z_{source}}$ ($h^{-1}M_{\odot}$)
lrg_3_651	NA	NA	NA	NA	NA
lrg_3_757	3.63E+12	1.61E+11	1.60E+11	1.56E+10	6.70E+08
lrg_3_810	8.34E+12	1.99E+12	3.89E+11	1.43E+11	1.95E+12
lrg_3_227	9.29E+12	5.70E+11	5.70E+11	8.31E+09	7.87E+09
lrg_4_581a	3.02E+13	6.49E+12	1.30E+12	1.97E+12	6.05E+12
lrg_4_606	1.03E+13	6.30E+11	6.30E+11	4.37E+09	3.11E+09
lrg_4_670	1.18E+13	5.90E+11	5.28E+11	5.45E+09	2.65E+11
bcg_3_067	7.83E+12	3.33E+11	1.23E+11	2.09E+11	2.29E+11
lrg_2_2811	2.07E+12	2.07E+11	2.07E+11	1.14E+09	7.94E+08
eight_oclock	1.28E+12	8.71E+10	8.71E+10	5.32E+08	1.45E+08
lrg_4_581b	1.20E+13	1.86E+12	3.84E+11	6.90E+09	1.82E+12

Using SDSS plus follow-up data.
Follow-up observations ruled out lrg_3_651 as a lensing system (NA).

6.2 Light

Often there are multiple lenses within the Einstein radius. The number of lensing galaxies for each system is shown in Table 6.8. Images for each system are shown in Section 5.3.

Table 6.8 Number of lensing galaxies within the Einstein radius of each lensing system

lensing system	name	number of lensing galaxies
1	lrg_3_651	2
2	lrg_3_757	1
3	lrg_3_810	5
4	lrg_3_227	2
5	lrg_4_581a	5
6	lrg_4_606	4
7	lrg_4_670	3
8	bcg_3_067	2
9	lrg_2_2811	1
10	eight_oclock	1
11	lrg_4_581b	3

The majority of the light for each lensing system is usually from the central LRG or BCG used in the query alone or combined with one of the neighboring bright red galaxies found within the Einstein radius. This can be seen by comparing the magnitude (dered_u, dered_g, etc.) of the LRG or BCG with the magnitudes of the other galaxies interior to the Einstein radius for each system (Table 6.9). The central LRG or BCG is indicated in the first column.

Accurate redshift information is not available for all of the fainter galaxies inside the Einstein radii. It is assumed they contribute to the lensing and are not foreground or background galaxies from their colors. If the galaxy is red and is within the Einstein radius, it is assumed to be part of the lens.

Table 6.9 Properties of all lenses within the Einstein radius of each lensing system.
Explanation of column labels:
k-corrections (kcorr_*),
extinction-corrected magnitudes (dered_*) and their errors (err_*).

Note that the LRG or BCG used in the query is indicated. The color is only to help guide the eye to separate each lensing system.

Lensing system	kcorr_u	kcorr_g	kcorr_r	kcorr_i	kcorr_z	dered_u	dered_g	dered_r	dered_i	dered_z	err_u	err_g	err_r	err_i	err_z
lrg_3_651	1.0481	1.2333	0.4502	0.2574	0.1686	20.9462	19.4469	17.9221	17.4059	17.0382	0.3430	0.0316	0.0125	0.0133	0.0307
						26.3922	20.5180	19.7013	19.1537	18.3200	1.5432	0.0926	0.0661	0.0707	0.1140
lrg_3_757	2.9970	1.7318	0.7436	0.4050	0.2788	23.0958	20.6420	18.8717	18.1329	17.6945	1.3825	0.0626	0.0198	0.0157	0.0393
lrg_3_810	2.6335	1.6328	0.6212	0.3622	0.2564	22.5584	19.7553	17.8555	17.2420	16.7661	0.9178	0.0317	0.0102	0.0093	0.0212
						23.1454	21.0935	19.7520	18.9890	18.5166	1.0210	0.0661	0.0678	0.0262	0.0646
						21.5531	20.0288	19.2165	18.6942	18.2146	0.2164	0.0241	0.0182	0.0174	0.0406
						20.6882	19.5768	18.9191	18.4907	18.0005	0.1071	0.0173	0.0148	0.0152	0.0339
						23.4878	23.3694	22.0939	22.3903	21.1380	1.6944	0.5959	0.3121	0.6311	0.7903
lrg_3_227	3.2716	1.7968	0.8134	0.4248	0.2916	24.2216	19.9887	18.2681	17.4747	17.0787	3.1018	0.0399	0.0142	0.0112	0.0228
						24.5373	22.1812	20.7548	20.2465	19.4388	2.1164	0.1790	0.0785	0.0769	0.1151
lrg_4_581a	2.5908	1.6402	0.6370	0.3685	0.2584	22.2480	20.5588	18.7950	18.1607	17.6332	0.6708	0.0469	0.0166	0.0137	0.0310
						22.9447	20.2905	18.5577	17.8356	17.3913	1.2372	0.0384	0.0142	0.0110	0.0261
						22.3225	21.6590	20.9195	20.3974	19.7375	0.5323	0.0890	0.0723	0.0666	0.1433
						22.8354	21.8568	21.7775	21.2964	20.9438	0.7573	0.0985	0.1442	0.1388	0.3827
						22.9070	21.6171	20.5667	19.8240	19.1468	1.1461	0.1217	0.0705	0.0537	0.1128
lrg_4_606	3.6838	1.9185	0.9453	0.4572	0.3137	23.8930	20.9515	18.9853	18.1064	17.8474	4.7311	0.1384	0.0379	0.0276	0.0971
						24.8461	22.5060	21.1746	20.0693	19.6094	1.2364	0.1459	0.0661	0.0407	0.1129
						23.0913	23.2671	21.1727	20.5597	19.8970	1.2182	0.4758	0.1170	0.1071	0.2697
						22.0989	22.2952	20.6742	19.8475	19.4417	0.4157	0.1612	0.0577	0.0445	0.1349
lrg_4_670	2.8732	1.6856	0.6849	0.3861	0.2687	20.9812	19.5560	17.7449	17.0565	16.6620	0.3392	0.0380	0.0121	0.0101	0.0256
						24.1305	22.0023	20.5648	19.9778	19.3153	2.3256	0.2109	0.0849	0.0736	0.2000
						25.0810	25.6968	22.7424	21.7012	21.7104	0.8080	0.4917	0.2379	0.1376	0.5059
bcg_3_067	2.1320	1.6525	0.7062	0.3896	0.2641	24.2898	20.5122	18.8662	18.1499	17.8036	2.7717	0.0595	0.0211	0.0198	0.0467
						24.3847	21.0349	19.4941	19.1354	18.3935	1.4739	0.0519	0.0208	0.0256	0.0427
lrg_2_2811	1.5523	1.5765	0.6943	0.3797	0.2491	22.5336	19.9145	18.3486	17.6650	17.2555	1.3138	0.0397	0.0161	0.0124	0.0311
8 o'clock	1.4845	1.5110	0.6213	0.3544	0.2324	21.8575	19.8822	18.2906	17.6490	17.2310	0.7290	0.0476	0.0173	0.0131	0.0331
lrg_4_581b	2.5469	1.7023	0.7330	0.4002	0.2737	22.9447	20.2905	18.5577	17.8356	17.3913	1.2372	0.0384	0.0142	0.0110	0.0261
						22.2480	20.5588	18.7950	18.1607	17.6332	0.6708	0.0469	0.0166	0.0137	0.0310
						22.3225	21.6590	20.9195	20.3974	19.7375	0.5323	0.0890	0.0723	0.0666	0.1433

6.2.1 Luminosity Calculations

The light, or luminosity (L), of each lens, expressed in terms of the luminosity of the Sun (L_{Sun}), was calculated for each lensing galaxy via

$$\frac{L_{lens}}{L_{Sun}} = 10^{\frac{-M+M_{Sun}}{2.5}},$$

where M is the absolute magnitude of the lensing galaxy, and M_{Sun} is the absolute magnitude of the Sun. The absolute magnitudes for the Sun are (from the SDSS website):

M(g)= +5.12 (+/-0.02)

u-g = +1.43 (+/-0.05) → u = 1.43+5.12 = 6.55

g-r = +0.44 (+/-0.02) → r = 5.12-0.44 = 4.68

r-i = +0.11 (+/-0.02) → i = 4.68-0.11 = 4.57

i-z = +0.03 (+/-0.02) → z = 4.57-0.3 = 4.27

The absolute magnitude of each lensing galaxy is

$$M = m - DM - k,$$

where m is the apparent magnitude, DM is the distance modulus, and k is the k-correction. The apparent magnitude and k-correction for each lensing galaxy are given in the SDSS database. The k-correction used for the luminosity calculation was chosen to be the k-correction for the LRG. The values for each system are shown in Table 6.2 above. The distance modulus is defined as

$$DM \equiv 5\log_{10}\left(\frac{D_L(pc)}{10pc}\right),$$

where D_L is the luminosity distance of the lens. D_L can be expressed terms of the angular diameter distance (D_d)

$$D_L = D_d \cdot (1+z)^2.$$

Rewriting the expression for DM in a slightly different form and in units of *Mpc,* which are more amenable to extragalactic distances:

$$DM = 5\log_{10}\left(\frac{D_L(Mpc)}{10pc \cdot \frac{1Mpc}{10^6\,pc}}\right)$$

$$DM = 5\log_{10}(D_L(Mpc)) - 5\log_{10}(10^{-5}Mpc)$$

$$DM = 5\log_{10}(D_L(Mpc)) + 25$$

This expression for DM yields the following equation for the absolute magnitude:

$$M = m - [5\log_{10} D_L(Mpc)] - 25 - k.$$

The *total* light for each system was found by adding the luminosities for all the lensing galaxies in the system. The results for the *g, r, i,* and *z* bands are shown the Figure 6.8. The u-band signal is very noisy and weak, so it is not included in the analysis. The light values are rest-frame luminosities. The top four plots use SDSS data only for the calculations. The bottom four plots included follow-up data, which reduced the errors for some systems by providing a more accurate lens redshift. While follow-up data provided both improved source and lens redshifts for some systems, only the more accurate lens redshift information would affect the luminosity. Luminosity is not a function of the source redshift.

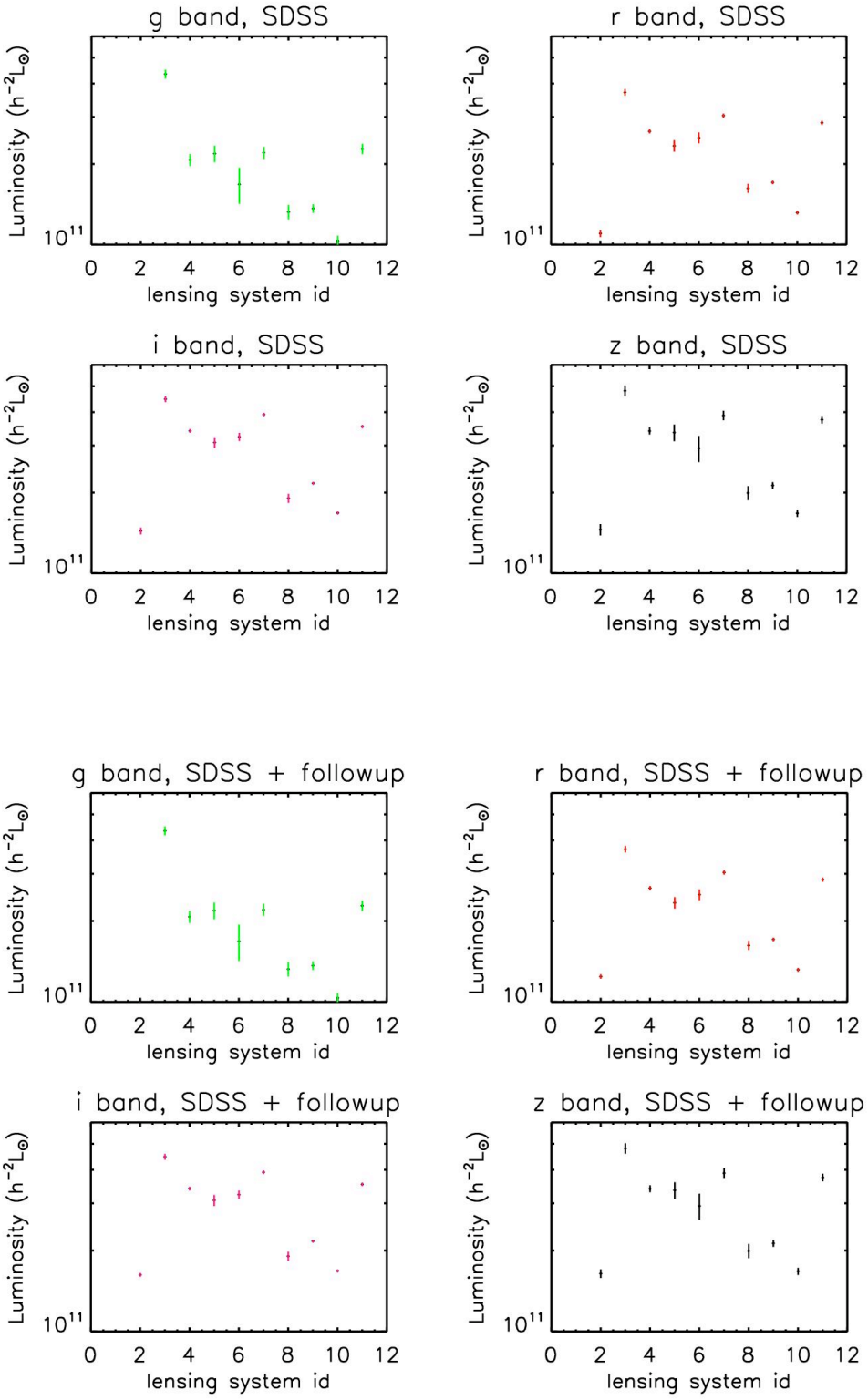

Figure 6.8 Luminosity for each lensing system.
SDSS data (top), SDSS and follow-up data (bottom).

6.2.2 Errors in the Luminosity

The errors in the luminosity, L, were calculated via

$$\sigma_L^2 = \sigma_{L,m}^2 + \sigma_{L,z_{lens}}^2,$$

where

$$\sigma_{L,m} = \left| \frac{L(m + m_{error}) - L(m - m_{error})}{2} \right|$$

$$\sigma_{L,z_{lens}} = \left| \frac{L(z_{lens} + z_{lens\_error}) - L(z_{lens} - z_{lens\_error})}{2} \right|$$

The magnitude error (m_{error}) is given for each apparent magnitude, m, for each object in the SDSS database. The error in the lens redshift affects the luminosity, because the luminosity distance, D_L, is a function of the lens redshift. The errors contributed by each variable are tabulated in Tables 6.10 (SDSS data only) and 6.11 (SDSS and follow-up data).

Additionally, the lens and source galaxies in these systems lie within ten arcseconds of each other. This close proximity might lead to the light from the LRGs and BCG getting tangled up in the light from the lensed blue galaxies in the deblending process. Deblending is the process by which overlapping objects in images are separated. Similarly, the color of the arcs might be contaminated with light from the nearby lens galaxy. We have not yet attempted to estimate the errors due to these effects.

Table 6.10 Luminosities and errors in luminosity using only SDSS data (g, r, i, and z bands).

SDSS data only	$L\ (h^{-2}L_{\odot})$	$\sigma_{L_{total}}\ (h^{-2}L_{\odot})$	$\sigma_{L,mag}\ (h^{-2}L_{\odot})$	$\sigma_{L,z_{lens}}\ (h^{-2}L_{\odot})$
g band				
lrg_3_651	NA	NA	NA	NA
lrg_3_757	8.04E+10	5.07E+09	4.64E+09	2.04E+09
lrg_3_810	4.34E+11	1.63E+10	1.37E+10	8.79E+09
lrg_3_227	2.08E+11	1.08E+10	1.08E+10	1.48E+08
lrg_4_581a	2.19E+11	1.56E+10	1.24E+10	9.46E+09
lrg_4_606	1.68E+11	2.62E+10	2.62E+10	9.17E+07
lrg_4_670	2.21E+11	1.14E+10	1.14E+10	1.28E+08
bcg_3_067	1.33E+11	8.25E+09	6.92E+09	4.49E+09
lrg_2_2811	1.37E+11	4.99E+09	4.99E+09	8.95E+07
eight_oclock	1.04E+11	4.54E+09	4.54E+09	5.19E+07
lrg_4_581b	2.28E+11	1.02E+10	1.02E+10	1.70E+08
r band				
lrg_3_651	NA	NA	NA	NA
lrg_3_757	1.10E+11	3.44E+09	2.01E+09	2.79E+09
lrg_3_810	3.71E+11	1.04E+10	7.21E+09	7.50E+09
lrg_3_227	2.65E+11	4.93E+09	4.92E+09	1.89E+08
lrg_4_581a	2.34E+11	1.15E+10	5.51E+09	1.01E+10
lrg_4_606	2.51E+11	1.17E+10	1.17E+10	1.37E+08
lrg_4_670	3.04E+11	5.38E+09	5.38E+09	1.76E+08
bcg_3_067	1.62E+11	6.34E+09	3.14E+09	5.50E+09
lrg_2_2811	1.71E+11	2.53E+09	2.53E+09	1.12E+08
eight_oclock	1.32E+11	2.10E+09	2.10E+09	6.61E+07
lrg_4_581b	2.85E+11	4.91E+09	4.90E+09	2.13E+08
i band				
lrg_3_651	NA	NA	NA	NA
lrg_3_757	1.44E+11	4.20E+09	2.09E+09	3.65E+09
lrg_3_810	4.47E+11	1.14E+10	6.85E+09	9.06E+09
lrg_3_227	3.41E+11	5.01E+09	5.00E+09	2.43E+08
lrg_4_581a	3.08E+11	1.45E+10	5.81E+09	1.33E+10
lrg_4_606	3.23E+11	1.10E+10	1.10E+10	1.76E+08
lrg_4_670	3.92E+11	5.67E+09	5.66E+09	2.27E+08
bcg_3_067	1.91E+11	7.48E+09	3.77E+09	6.46E+09
lrg_2_2811	2.17E+11	2.48E+09	2.48E+09	1.42E+08
eight_oclock	1.68E+11	2.04E+09	2.04E+09	8.43E+07
lrg_4_581b	3.53E+11	4.87E+09	4.86E+09	2.64E+08
z band				
lrg_3_651	NA	NA	NA	NA
lrg_3_757	1.46E+11	7.09E+09	5.28E+09	4.73E+09
lrg_3_810	4.81E+11	2.15E+10	1.75E+10	1.25E+10
lrg_3_227	3.40E+11	1.01E+10	1.01E+10	3.11E+08
lrg_4_581a	3.36E+11	2.39E+10	1.50E+10	1.86E+10
lrg_4_606	2.93E+11	3.28E+10	3.28E+10	2.05E+08
lrg_4_670	3.89E+11	1.57E+10	1.57E+10	2.89E+08
bcg_3_067	2.00E+11	1.20E+10	8.33E+09	8.68E+09
lrg_2_2811	2.13E+11	6.10E+09	6.10E+09	1.79E+08
eight_oclock	1.68E+11	5.10E+09	5.10E+09	1.08E+08
lrg_4_581b	3.75E+11	1.22E+10	1.22E+10	3.59E+08

Table 6.11 Luminosities and errors in luminosity using SDSS and follow-up data (g, r, i, and z bands).

SDSS + followup	L ($h^{-2}L_{\odot}$)	$\sigma_{L_{total}}$ ($h^{-2}L_{\odot}$)	$\sigma_{L,mag}$ ($h^{-2}L_{\odot}$)	$\sigma_{L,z_{lens}}$ ($h^{-2}L_{\odot}$)
g band				
lrg_3_651	NA	NA	NA	NA
lrg_3_757	9.07E+10	5.26E+09	5.24E+09	5.03E+08
lrg_3_810	4.34E+11	1.63E+10	1.37E+10	8.79E+09
lrg_3_227	2.08E+11	1.08E+10	1.08E+10	1.48E+08
lrg_4_581a	2.19E+11	1.56E+10	1.24E+10	9.46E+09
lrg_4_606	1.68E+11	2.62E+10	2.62E+10	9.17E+07
lrg_4_670	2.21E+11	1.14E+10	1.14E+10	1.28E+08
bcg_3_067	1.33E+11	8.25E+09	6.92E+09	4.49E+09
lrg_2_2811	1.37E+11	4.99E+09	4.99E+09	8.95E+07
eight_oclock	1.04E+11	4.54E+09	4.54E+09	5.19E+07
lrg_4_581b	2.28E+11	1.02E+10	1.02E+10	1.70E+08
r band				
lrg_3_651	NA	NA	NA	NA
lrg_3_757	1.24E+11	2.37E+09	2.27E+09	6.89E+08
lrg_3_810	3.71E+11	1.04E+10	7.21E+09	7.50E+09
lrg_3_227	2.65E+11	4.93E+09	4.92E+09	1.89E+08
lrg_4_581a	2.34E+11	1.15E+10	5.51E+09	1.01E+10
lrg_4_606	2.51E+11	1.17E+10	1.17E+10	1.37E+08
lrg_4_670	3.04E+11	5.38E+09	5.38E+09	1.76E+08
bcg_3_067	1.62E+11	6.34E+09	3.14E+09	5.50E+09
lrg_2_2811	1.71E+11	2.53E+09	2.53E+09	1.12E+08
eight_oclock	1.32E+11	2.10E+09	2.10E+09	6.61E+07
lrg_4_581b	2.85E+11	4.91E+09	4.90E+09	2.13E+08
i band				
lrg_3_651	NA	NA	NA	NA
lrg_3_757	1.62E+11	2.52E+09	2.35E+09	9.00E+08
lrg_3_810	4.47E+11	1.14E+10	6.85E+09	9.06E+09
lrg_3_227	3.41E+11	5.01E+09	5.00E+09	2.43E+08
lrg_4_581a	3.08E+11	1.45E+10	5.81E+09	1.33E+10
lrg_4_606	3.23E+11	1.10E+10	1.10E+10	1.76E+08
lrg_4_670	3.92E+11	5.67E+09	5.66E+09	2.27E+08
bcg_3_067	1.91E+11	7.48E+09	3.77E+09	6.46E+09
lrg_2_2811	2.17E+11	2.48E+09	2.48E+09	1.42E+08
eight_oclock	1.68E+11	2.04E+09	2.04E+09	8.43E+07
lrg_4_581b	3.53E+11	4.87E+09	4.86E+09	2.64E+08
z band				
lrg_3_651	NA	NA	NA	NA
lrg_3_757	1.64E+11	6.07E+09	5.95E+09	1.17E+09
lrg_3_810	4.81E+11	2.15E+10	1.75E+10	1.25E+10
lrg_3_227	3.40E+11	1.01E+10	1.01E+10	3.11E+08
lrg_4_581a	3.36E+11	2.39E+10	1.50E+10	1.86E+10
lrg_4_606	2.93E+11	3.28E+10	3.28E+10	2.05E+08
lrg_4_670	3.89E+11	1.57E+10	1.57E+10	2.89E+08
bcg_3_067	2.00E+11	1.20E+10	8.33E+09	8.68E+09
lrg_2_2811	2.13E+11	6.10E+09	6.10E+09	1.79E+08
eight_oclock	1.68E+11	5.10E+09	5.10E+09	1.08E+08
lrg_4_581b	3.75E+11	1.22E+10	1.22E+10	3.59E+08

6.3 Mass to Light Ratios

The mass to light ratios were calculated for each system using the mass and luminosity values described in the previous sections. Plots of M/L as a function of mass, M/L as a function of radius (in arcseconds), and M/L as a function of radius (in kiloparsecs) are shown in Figures 6.9, 6.10, and 6.11.

The calculation of the errors in M/L are presented in Section 6.3.1. The conversion of the radius from arcseconds to parsecs is related to the angular diameter distance. Since the angular diameter distance is a function of the lens redshift, the error in the redshift produces an error in the radius. The method to calculate this error is shown in Section 6.3.2.

The errors are tabulated in Tables 6.12 (SDSS data only) and 6.13 (SDSS and follow-up data).

6.3.1 Errors in M/L

The errors in the mass to light ratio, M/*L*, were calculated via

$$\sigma^2_{\frac{M}{L}} = \sigma^2_{\frac{M}{L},\theta_E} + \sigma^2_{\frac{M}{L},z_{source}} + \sigma^2_{\frac{M}{L},m} + \sigma^2_{\frac{M}{L},z_{lens}},$$

where

$$\sigma_{\frac{M}{L},\theta_E} = \frac{1}{2}\left|\frac{M(\theta_E + \theta_{E\_error})}{L} - \frac{M(\theta_E - \theta_{E\_error})}{L}\right|$$

$$\sigma_{\frac{M}{L},z_{source}} = \frac{1}{2}\left|\frac{M(z_{source\_maximun})}{L} - \frac{M(z_{source\_minimum})}{L}\right|$$

$$\sigma_{\frac{M}{L},m} = \frac{1}{2}\left|\frac{M}{L(m+\sigma_m)} - \frac{M}{L(m-\sigma_m)}\right|$$

$$\sigma_{\frac{M}{L},z_{lens}} = \frac{1}{2}\left|\frac{M(z_{lens} + z_{lens\_error})}{L(z_{lens} + z_{lens\_error})} - \frac{M(z_{lens} - z_{lens\_error})}{L(z_{lens} - z_{lens\_error})}\right|$$

θ_{E_error} is the standard deviation of 10 hand measurements of the Einstein radius using DS9. It affects the numerator of M/L through the dependence of mass on the Einstein radius.

The error in the source redshift affects the numerator of M/L through the dependence of the mass on the angular diameter distances, D_s and D_{ds}, which are dependent on the source redshift.

The error in the magnitude affects the denominator of M/L through the dependence of luminosity on the lens magnitude.

The error in the lens redshift affects both the numerator and denominator of M/L through the dependence of both the mass and the luminosity on the angular diameter distances, which are functions of the lens redshift.

The errors are presented in Tables 6.12 (SDSS data only) and 6.13 (SDSS and follow-up data).

6.3.2 Errors in Radius (Conversion from arcsec to kpc)

$$\sigma_R^2 = \sigma_{R,\theta_E}^2 + \sigma_{R,D_d}^2$$

$$\sigma_{R,\theta_E} = \left| \frac{R(\theta_E + \theta_{E,error}) - R(\theta_E + \theta_{E,error})}{2} \right|$$

$$\sigma_{R,z_{lens}} = \left| \frac{R(z_{lens} + z_{lens\_error}) - R(z_{lens} - z_{lens\_error})}{2} \right|$$

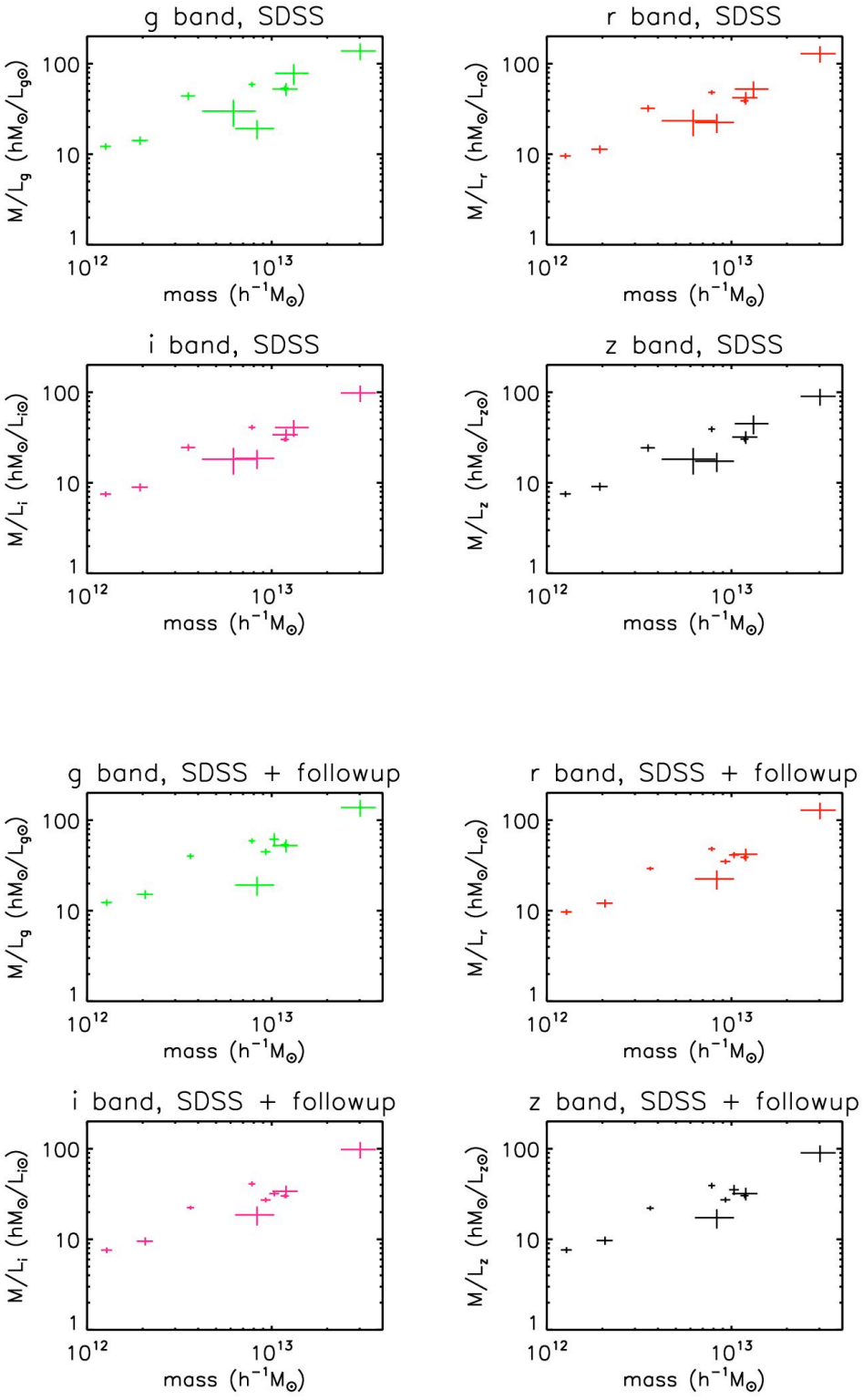

Figure 6.9 M/L for *g, r, i, z* as f(mass). SDSS data only (top). SDSS data plus follow up data (bottom).

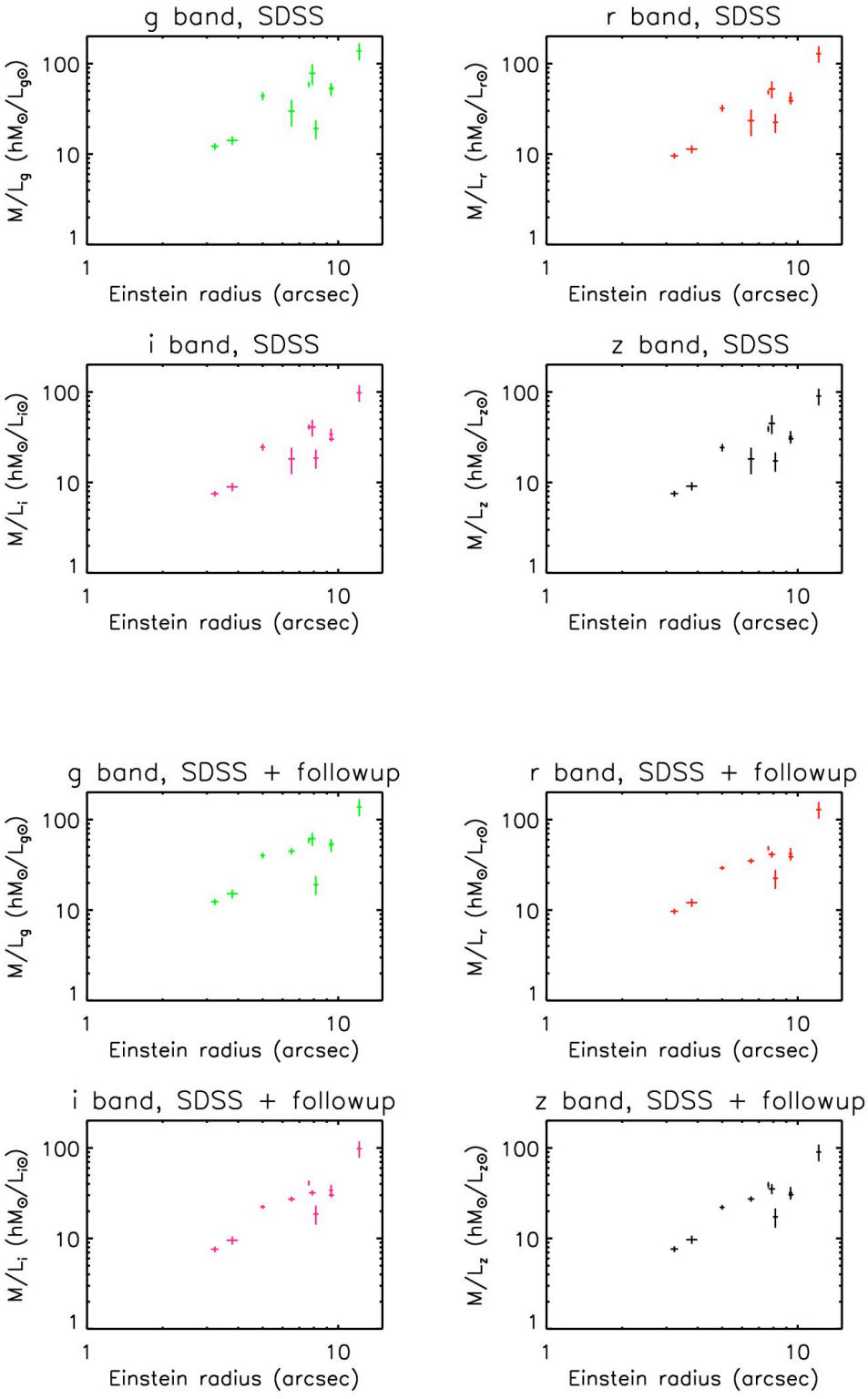

Figure 6.10 M/L for *g, r, i, z* as f(Einstein radius) units in arcsec. SDSS data only (top). SDSS data plus follow up data (bottom).

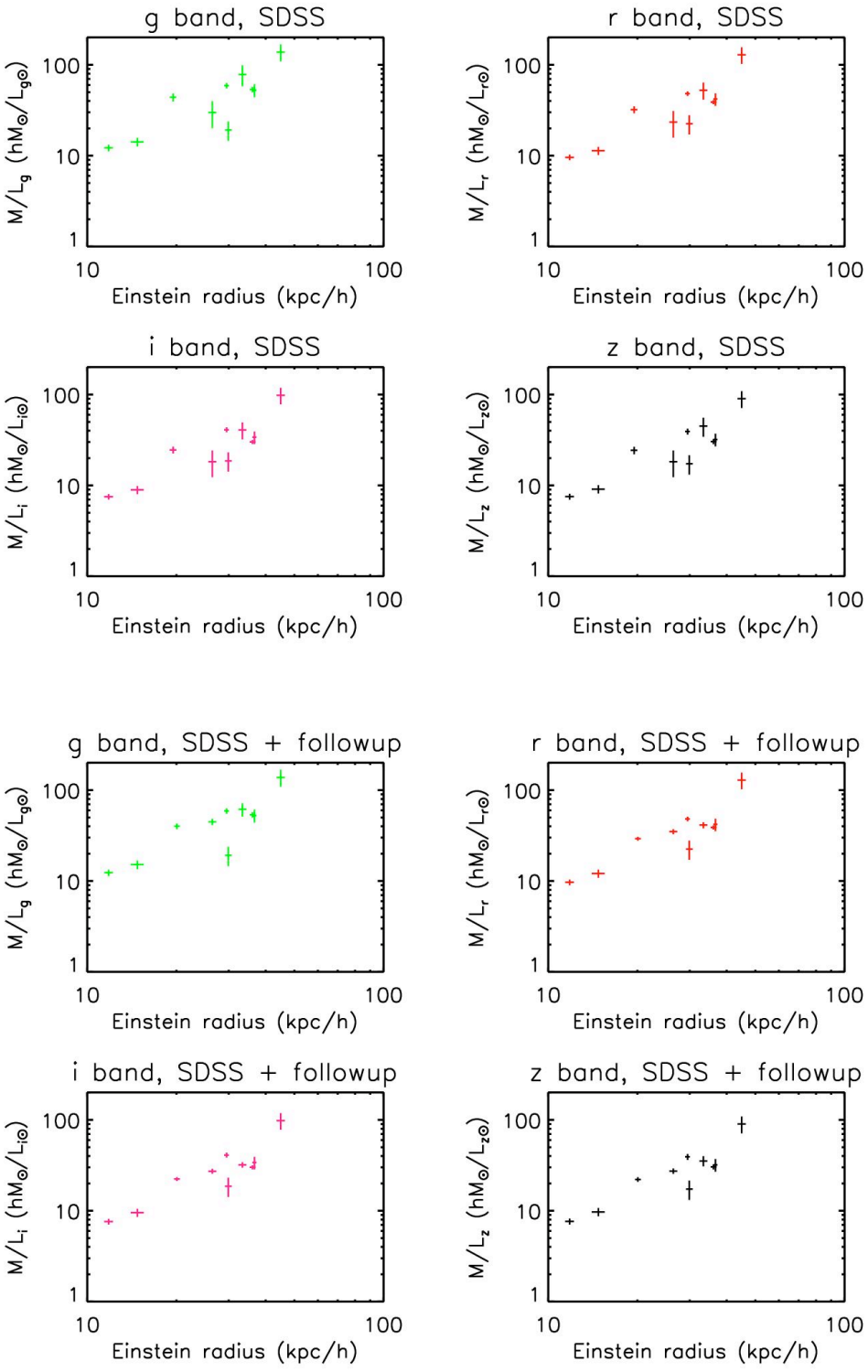

Figure 6.11 M/L for *g, r, i, z* as f(Einstein radius) units in kpc/h. SDSS data only (top). SDSS data plus follow-up data (bottom).

Table 6.12 M/L ratios and the associated errors with SDSS data only.

	M/L	$\sigma_{M/L,\theta_E}$	$\sigma_{M/L,z_{source}}$	$\sigma_{M/L,m}$	$\sigma_{M/L,z_{lens}}$	$\sigma_{M/L,total}$
g band						
lrg_3_651	NA	NA	NA	NA	NA	NA
lrg_3_757	44.017	1.936	3.195	2.540	0.198	4.520
lrg_3_810	19.206	0.896	4.483	0.605	0.060	4.612
lrg_3_227	29.928	1.835	9.541	1.549	0.005	9.839
lrg_4_581a	138.137	5.925	27.650	7.815	3.013	29.375
lrg_4_606	78.294	4.764	15.535	12.130	0.002	20.277
lrg_4_670	53.517	2.392	1.199	2.754	0.006	3.840
bcg_3_067	59.045	0.929	1.725	3.081	0.426	4.168
lrg_2_2811	14.199	1.424	0.094	0.519	0.002	1.519
eight_oclock	12.198	0.831	0.088	0.535	0.001	0.993
lrg_4_581b	52.522	1.683	7.986	2.350	0.009	8.493
r band						
lrg_3_651	NA	NA	NA	NA	NA	NA
lrg_3_757	32.118	1.412	2.332	0.586	0.144	2.793
lrg_3_810	22.491	1.049	5.250	0.437	0.070	5.372
lrg_3_227	23.410	1.436	7.463	0.434	0.004	7.612
lrg_4_581a	129.163	5.540	25.854	3.036	2.817	26.655
lrg_4_606	52.457	3.192	10.409	2.435	0.002	11.156
lrg_4_670	38.894	1.738	0.871	0.689	0.005	2.063
bcg_3_067	48.182	0.758	1.408	0.933	0.348	2.732
lrg_2_2811	11.344	1.138	-0.075	0.168	0.002	1.153
eight_oclock	9.584	0.653	-0.069	0.153	0.001	0.674
lrg_4_581b	41.983	1.345	-6.383	0.721	0.007	6.563
i band						
lrg_3_651	NA	NA	NA	NA	NA	NA
lrg_3_757	24.586	1.081	1.785	0.356	0.111	2.123
lrg_3_810	18.635	0.869	4.350	0.285	0.058	4.445
lrg_3_227	18.232	1.118	5.812	0.268	0.003	5.925
lrg_4_581a	98.229	4.213	19.662	1.854	2.143	20.248
lrg_4_606	40.724	2.478	8.080	1.389	0.001	8.565
lrg_4_670	30.141	1.347	0.675	0.435	0.004	1.569
bcg_3_067	41.036	0.645	1.199	0.811	0.296	2.559
lrg_2_2811	8.937	0.897	0.059	0.102	0.001	0.904
eight_oclock	7.510	0.512	0.054	0.091	0.001	0.523
lrg_4_581b	33.905	1.086	5.155	0.467	0.006	5.289
z band						
lrg_3_651	NA	NA	NA	NA	NA	NA
lrg_3_757	24.310	1.069	1.765	0.881	0.085	2.249
lrg_3_810	17.338	0.809	4.047	0.627	0.042	4.175
lrg_3_227	18.259	1.120	5.821	0.541	0.002	5.952
lrg_4_581a	90.106	3.865	18.036	4.029	1.533	18.938
lrg_4_606	44.918	2.733	8.913	5.018	0.001	10.587
lrg_4_670	30.370	1.357	0.680	1.223	0.003	1.949
bcg_3_067	39.190	0.616	1.145	1.634	0.220	2.898
lrg_2_2811	9.112	0.914	0.060	0.261	0.001	0.953
eight_oclock	7.538	0.514	0.054	0.230	0.001	0.565
lrg_4_581b	31.964	1.024	4.860	1.037	0.004	5.074

Units are all $h\mathrm{M}_{\odot}/\mathrm{L}_{\odot}$

Table 6.13 M/L ratios and the associated errors with SDSS and follow-up data.

	M/L	$\sigma_{M/L,\theta_E}$	$\sigma_{M/L,z_{source}}$	$\sigma_{M/L,m}$	$\sigma_{M/L,z_{lens}}$	$\sigma_{M/L,total}$
g band						
lrg_3_651	NA	NA	NA	NA	NA	NA
lrg_3_757	40.036	1.761	0.007	2.310	0.050	2.905
lrg_3_810	19.206	0.896	4.483	0.605	0.060	4.612
lrg_3_227	44.775	2.746	0.038	2.317	0.008	3.593
lrg_4_581a	138.137	5.925	27.650	7.815	3.013	29.375
lrg_4_606	61.551	3.745	0.018	9.536	0.008	10.245
lrg_4_670	53.517	2.392	1.199	2.754	0.006	3.840
bcg_3_067	59.045	0.929	1.725	3.081	0.426	4.168
lrg_2_2811	15.138	1.519	0.006	0.553	0.002	1.616
eight_oclock	12.339	0.841	0.001	0.541	0.001	1.000
lrg_4_581b	52.522	1.683	7.986	2.350	0.009	8.493
r band						
lrg_3_651	NA	NA	NA	NA	NA	NA
lrg_3_757	29.213	1.285	0.005	0.533	0.037	1.391
lrg_3_810	22.491	1.049	5.250	0.437	0.070	5.372
lrg_3_227	35.023	2.148	0.030	0.650	0.006	2.244
lrg_4_581a	129.163	5.540	25.854	3.036	2.817	26.655
lrg_4_606	41.239	2.509	0.012	1.915	0.005	3.156
lrg_4_670	38.894	1.738	0.871	0.689	0.005	2.063
bcg_3_067	48.182	0.758	1.408	0.933	0.348	2.732
lrg_2_2811	12.094	1.213	0.005	0.179	0.001	1.226
eight_oclock	9.694	0.661	-0.001	0.154	0.001	0.679
lrg_4_581b	41.983	1.345	6.383	0.721	0.007	6.563
i band						
lrg_3_651	NA	NA	NA	NA	NA	NA
lrg_3_757	22.362	0.983	0.004	0.324	0.028	1.036
lrg_3_810	18.635	0.869	4.350	0.285	0.058	4.445
lrg_3_227	27.277	1.673	0.023	0.401	0.005	1.720
lrg_4_581a	98.229	4.213	19.662	1.854	2.143	20.248
lrg_4_606	32.015	1.948	0.010	1.092	0.004	2.233
lrg_4_670	30.141	1.347	0.675	0.435	0.004	1.569
bcg_3_067	41.036	0.645	1.199	0.811	0.296	2.559
lrg_2_2811	9.528	0.956	0.004	0.109	0.001	0.962
eight_oclock	7.596	0.518	0.001	0.092	0.001	0.526
lrg_4_581b	33.905	1.086	5.155	0.467	0.006	5.289
z band						
lrg_3_651	NA	NA	NA	NA	NA	NA
lrg_3_757	22.112	0.972	0.004	0.801	0.022	1.261
lrg_3_810	17.338	0.809	4.047	0.627	0.042	4.175
lrg_3_227	27.317	1.675	0.023	0.810	0.004	1.861
lrg_4_581a	90.106	3.865	18.036	4.029	1.533	18.938
lrg_4_606	35.312	2.149	0.011	3.945	0.003	4.492
lrg_4_670	30.370	1.357	0.680	1.223	0.003	1.949
bcg_3_067	39.190	0.616	1.145	1.634	0.220	2.898
lrg_2_2811	9.714	0.975	0.004	0.278	0.001	1.013
eight_oclock	7.625	0.520	0.001	0.232	0.001	0.569
lrg_4_581b	31.964	1.024	4.860	1.037	0.004	5.074

Units are all $h\mathrm{M}_{\odot}/\mathrm{L}_{\odot}$

CHAPTER 7

ANALYSIS OF RESULTS

"From there to here, and here to there, funny things are everywhere."
-Dr Seuss

Astronomers are interested in determining the matter density of the universe. The universal mass density can be estimated from the observed mean luminosity density in the universe when multiplied by the *M/L* ratio on large scales (Bahcall et al. 1995). The density parameter is important in determining the spatial curvature and expansion rate of the universe. Another reason to learn about the matter density is to determine what the universe is made of, i.e., what fraction of the density is baryonic, what fraction is dark matter, and what constitutes dark matter (Ryden, 2003). In an effort to answer these questions, several techniques to measure mass have been developed. An overview of these techniques is presented in Section 7.1.

Trends in *M/L* as a function of mass and scale in our ten lensing systems are presented in Section 7.2. Differences as a function of bandpass are also discussed. *M/L* derived from the ten lensing systems studied in this thesis are compared to data found in the literature in Section 7.3. We show that the increasing *M/L* with scale observed on the scales of our lensing systems (~10 kpc to ~50 kpc) are consistent with published *M/L* for galaxies and groups of galaxies on both similar and smaller

(1 kpc -10 kpc) scales, and we also discuss *M/L* for larger (100 kpc – 1 Mpc) scales from the literature.

7.1 How to Measure Mass

Converting an observed luminosity to mass using an assumed average *M/L* for stars yields a mass much less than is derived by other methods, implying that not all mass is luminous (Ryden 2003). The other methods can be classified into three categories: using cosmology, detecting matter via its gravitational effect on luminous matter, and detecting matter by its effect on the trajectory of photons. An outline of these techniques is presented in Figure 7.1. The three categories are discussed briefly in the following three sections.

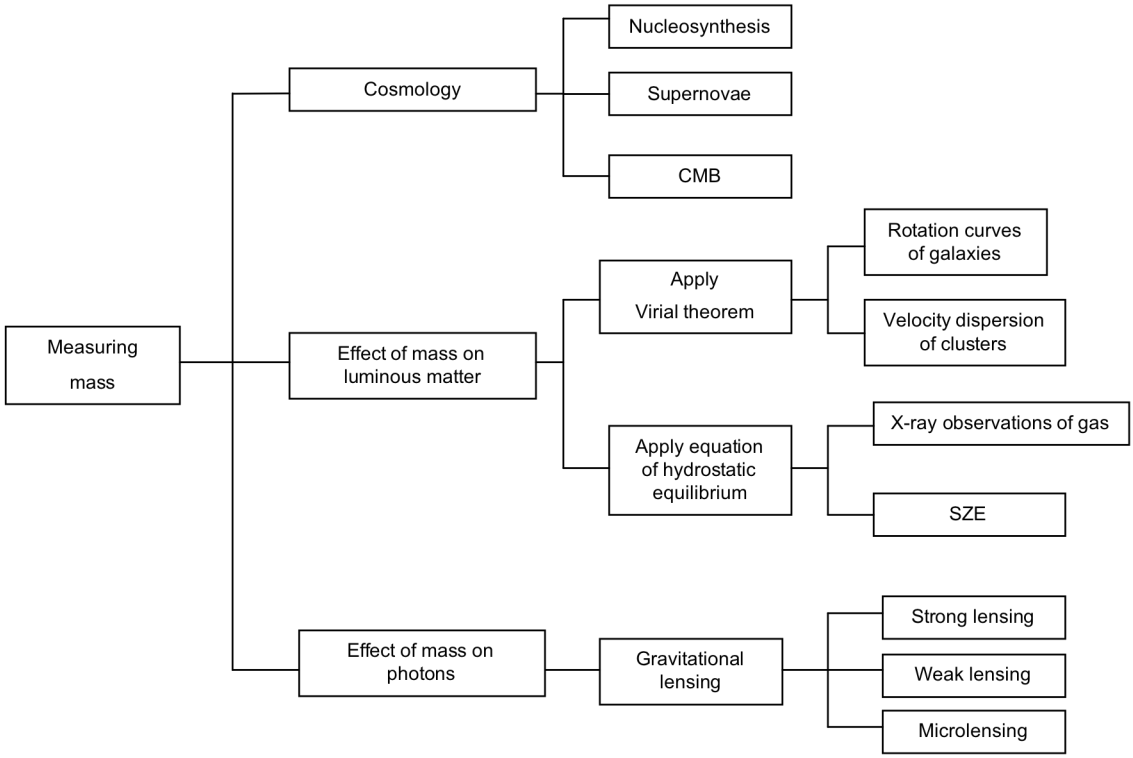

Figure 7.1 Methods for determining mass.

7.1.1 Measuring Matter Density by Cosmology

One way of measuring the total mass density is to pick out observations that are sensitive to Ω_b/Ω_m (where Ω_b is the baryon density), and use the apparent value of Ω_b to infer Ω_m. Anisotropies in the CMB are also sensitive to the matter density. (Dodelson 2003).

The distribution of galaxies in the universe, in particular, the power spectrum of this distribution, is very sensitive to Ω_m. Another method relates the cosmic velocity field to the observed galaxy spectrum. This relation is sensitive to Ω_m. (Dodelson 2003).

7.1.2 Detecting Matter by its Effect on the Trajectory of Mass

From studies of the Coma cluster, it has been found that the total amount of x-ray-emitting gas is $\sim 2\times10^{14}\ M_{Sun}$, roughly 6-7 times its mass in stars. Studies of the dynamics of the stars and gas imply there is additional baryonic matter too cold (brown dwarfs and cold stellar remnants) or too diffuse (low-density x-ray gas in clusters) to be readily visible, as well as nonbaryonic dark matter which doesn't absorb, emit, or scatter light at any wavelength (Ryden 2003).

If the orbital speed, *v,* is considered as approximately constant with radius, the mass of a spiral galaxy, including both the luminous disk and the dark halo, can be found from

$$M(R_{halo}) = \frac{v^2 R_{halo}}{G}\ , \qquad \text{Equation 7.1}$$

where R_{halo} is the radius of of the dark halo (Ryden 2003). A rough estimate of R_{halo} can be made by looking at the velocities of globular clusters and satellite galaxies.

An analogous method can be applied to estimate elliptical galaxy and cluster masses. Because the systems are gravitationally bound, not expanding with the Hubble flow, and they are moving at nonrelativistic speeds, the dynamics can be treated by Newtonian mechanics. The virial theorem can be used to estimate the mass

$$M = \frac{\langle v^2 \rangle r_h}{\alpha G}, \qquad \text{Equation 7.2}$$

where r_h is the half-mass radius (the radius of a sphere centered on the center of the mass and containing a mass $M/2$), and α is a numerical factor of order unity that depends on the density profile (Ryden 2003).

There is a similarity between Equation 7.1, used to estimate the mass of a spiral galaxy, and Equation 7.2, used to estimate the mass of a cluster of galaxies. In either case, the mass of a self-gravitating system can is estimated by multiplying the square of a characteristic velocity by a characteristic radius, then dividing by the gravitational constant *G*. Having only partial information complicates both cases. For clusters, $\langle v^2 \rangle$ and r_h are not known exactly. R_{halo} is not known for spiral galaxies. Approximations and assumptions must be made.

A completely different tracer of galaxy cluster mass is the hot gas that is visible in x-rays. The x-ray gas indicates the presence of dark matter. If there were no gravitational attraction by dark matter, the hot gas would have expanded beyond a galaxy or cluster on time scales much shorter than the Hubble time. The temperature and density of the hot gas can be used to make another estimate of the total mass. If the hot gas is supported by its own pressure against gravitational infall, it can be assumed to obey the equation of hydrostatic equilibrium. Combining the equation of hydrostatic equilibrium with the ideal gas law, the mass as a function of radius, *r*, is

$$M(r) = \frac{kT(r)r}{G\mu m_p}\left[-\frac{d\ln\rho}{d\ln r} - \frac{d\ln T}{d\ln r}\right] \qquad \text{Equation 7.3}$$

where *T* is the temperature of the gas, μ is the mass in units of the proton mass (m_p), ρ is the density of the gas, and *M* is the total mass inside a sphere of radius *r* (Ryden 2003). Again there are estimates and approximations involved. A spherical distribution of gas is assumed, although observations show this is not exact (Figure 7.2). It is assumed μ is constant with radius, which would be expected if the chemical composition and ionization state of the gas are uniform throughout the cluster.

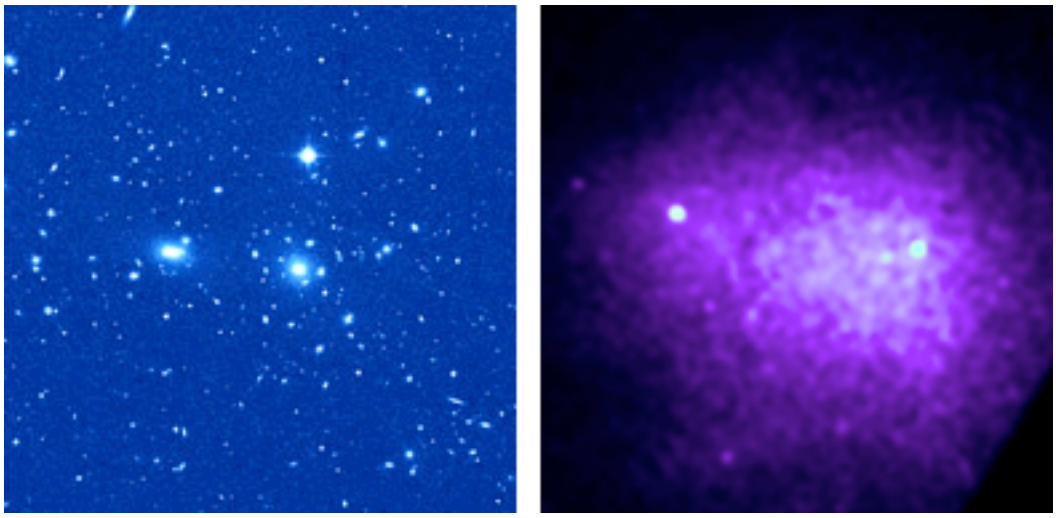

Figure 7.2 Optical (left) and x-ray (right) image of Coma cluster.
(Image credit: NASA/CXC/SAO,)

The x-rays are a combination of bremsstrahlung emission, caused by acceleration of free electrons by protons and helium nuclei, and line emission from highly ionized iron and other heavy elements. It is possible to fit models to the emission to compute the temperature, pressure and chemical composition required to obtain a mass estimate from Equation 7.3.

An estimate of the mass of the Coma cluster using the virial theorem applied to its galaxies is consistent with the mass estimate derived from the equation of hydrostatic equilibrium applied to its gas, yielding a mass of $\sim 2 \times 10^{15} M_{\odot}$ (Ryden 2003).

The hot gas that x-ray observations reveal in clusters may also be detected in ways other than via its thermal bremsstrahlung emission. Scattering of cosmic microwave background (CMB) photons by the hot thermal distribution of electrons leads to a distortion in the CMB spectrum known as the Sunyeav-Zel'dovich effect

(SZE) (Carlstrom et al., 2002). CMB photons passing through a cluster will undergo inverse Compton scattering by collisions with the intracluster medium. The photons that scatter off the much higher energy electrons will, on average, be shifted to higher energy. The resulting CMB spectrum is non-Planckian. Compared to an initial Planck spectrum, there are fewer photons at low energies and more at higher energies (Figure 7.3).

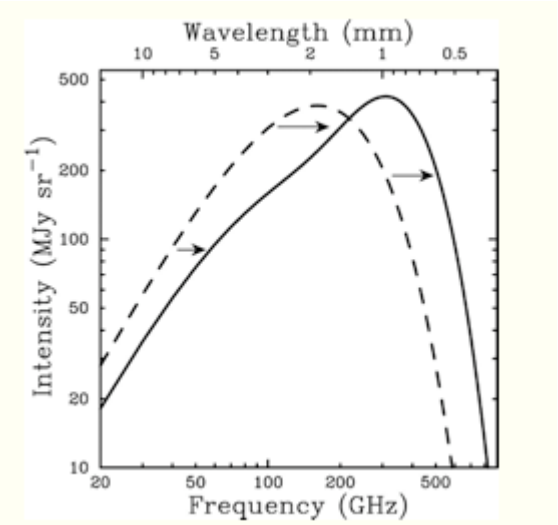

Figure 7.3 CMB intensity (dashed line). Distortion of CMB due to SZE (solid line) (Carlstrom et al. 2002),

The intensity of the SZE summed over an entire cluster depends on the total mass of the cluster. A smaller mass cluster produces a weaker signal than a higher mass cluster. (Hence the SZE is associated with massive objects as clusters. A single galaxy has insufficient mass to cause detectable distortions in the CMB.)

7.1.3 Comparison of Mass Estimate from Dynamics to Lensing

The big difference and advantage of lensing over mass estimates from dynamics is that one need not assume dynamical or hydrostatic equilibrium. The mass derived from lensing is independent of equilibrium conditions. Additionally, the dynamical models suffer from the required approximations and assumptions described in Section 7.1.2.

Studies have been done to compare mass estimates from lensing to those derived from other methods with slightly inconsistent results (Peacock 2003). Some have found that lensing results give masses a factor of two larger than those from x-rays. This would require some means of supporting the gas in addition to its thermal pressure. Magnetic fields would be a possibility. Alternatively, more sophisticated x-ray gas models may be required. For example, the models may need to allow for a mix of temperatures and densities at a given radius (Peacock 2003).

On scales beyond 100 kpc there is no evidence of a discrepancy between lensing and x-ray masses (Peacock 2003).

Substructure of dark matter halos can be very complex and the definition of a dark matter halo center is scale dependent (Cabanac et al. 2007). While weak lensing can reveal mass to light ratios of clusters, it cannot provide information about the inner structure of clusters. Strong lensing can help reveal the detailed structure of cluster halos and their light vs. mass distribution. Strong lensing arcs in the center of group haloes can provide a unique measure of the total projected density profile,

where dynamical estimates only provide constraints on the baryonic mass with the strong assumption that groups are virialized systems (Cabanac et al. 2007).

However, gravitational lensing is not free of assumptions. The limitations include how well the chosen lensing model represents reality. For example, is an SIS mass profile a legitimate profile to assume or is a different or more complex profile required? Errors in the redshifts of the lens and source as well as the quality and depth of the photometry can affect the resultant mass.

7.2 Trends in our Data

The scales of the arc systems studied in this thesis range from ~10 kpc to ~50 kpc. The observed Einstein radii were converted to distance using the relation for the angular diameter distance, which is a function of redshift and cosmology. The observed Einstein radii range from about 3" to 9.5". The lower limit is constrained by the 1.4" point spread function (PSF) of the SDSS. (PSF is a mathematical description of the image of a point source formed by a telescope and associated instrumentation.) However, the true lower limit is a bit larger, ~2", imposed by the ability of the those doing the manual inspection of the arc candidates to resolve the images. The upper limit was constrained by our search radius of 10". (The radius of one system was 12.2", which escaped the limit, because this arc was found serendipitously, associated with a system of a smaller radius.)

7.2.1 M/L as f(radius)

M/L increases with radius (Figure 7.4). This can be understood by considering that, for larger and larger radii, more and more of the region beyond the luminous parts of a galaxy are being probed and more mass, but not very much more light, is being included. It can also be inferred that the radii probed have not extended beyond the dark matter halo. If the radii were larger than the halo, there would be no additional mass to add, and *M/L* would be constant.

Not all of our systems are individual galaxies. For some systems, the light from one (or two) large and a few small neighboring galaxies are included within the radius. From the observed trend of increasing *M/L* with radius, it can be concluded that the added mass is still increasing faster than the added light from the neighbors.

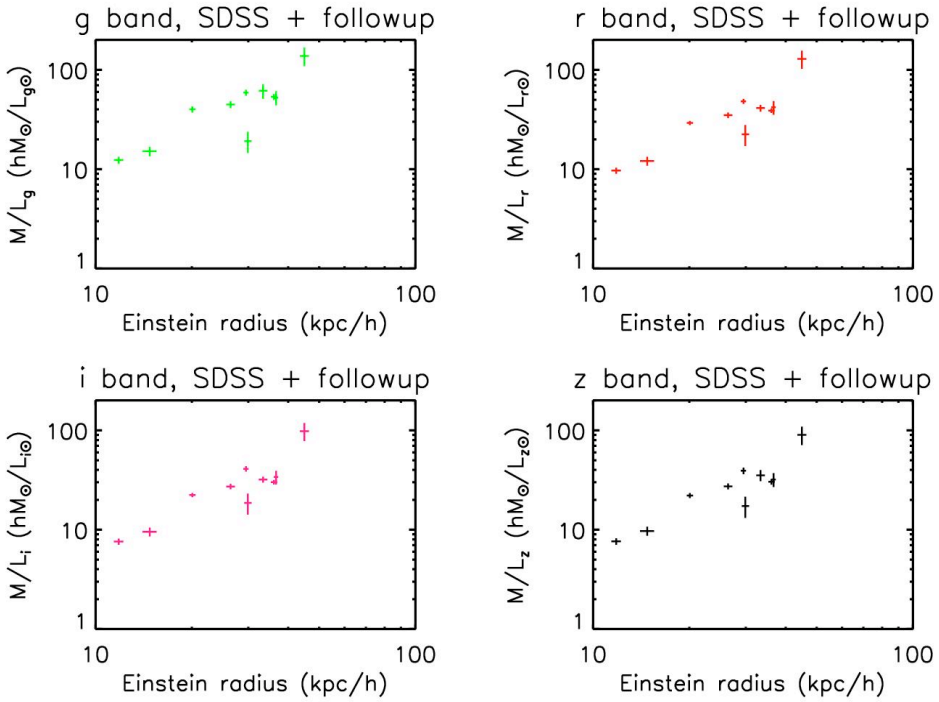

Figure 7.4 M/L vs. radius for four SDSS bandpasses.

7.2.2 M/L as f(mass)

M/L also increases with the mass of the lens (Figure 7.5). Our sample of lensing systems ranges from individual galaxies to groups. Table 7.1 shows the approximate range of mass, radius, and *M/L* for objects of different scales. The larger the radius, the more non-luminous mass is included in the total.

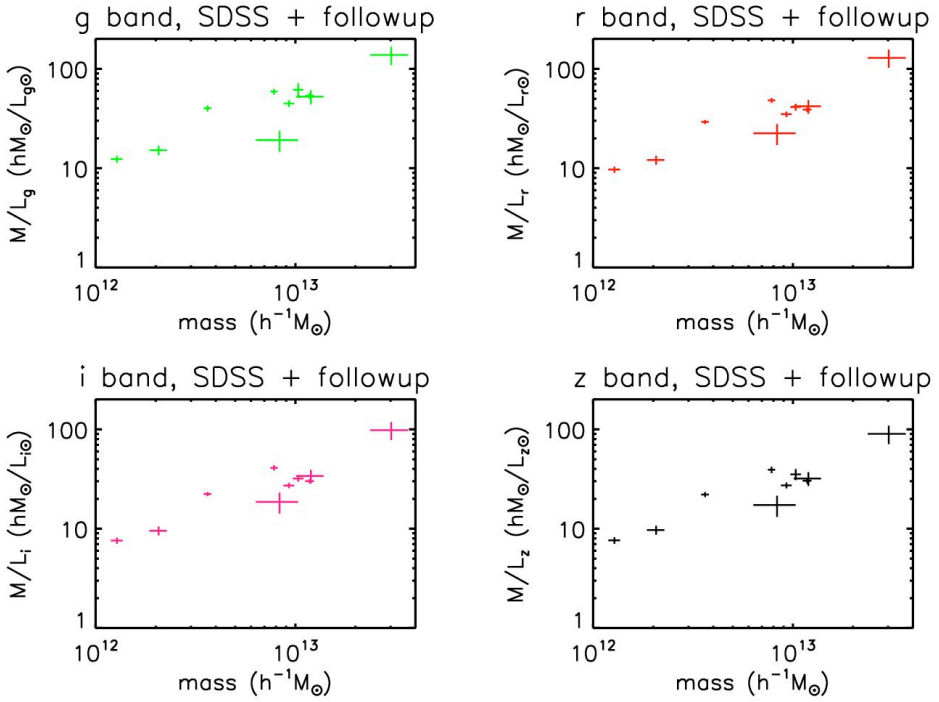

Figure 7.5 M/L vs. mass for four SDSS bandpasses.

Table 7.1 Approximate mass, radius, and *M/L* for different scales.

	mass ($M_\odot$)	radius (kpc)	M / L ($M_\odot/L_\odot$)
stars	1		1
Milky Way	~3e12	~300	~150
spiral galaxies	~10e12	~1-300	1-200
elliptical galaxies	~10e12	~1-200	1-100
groups	~10e13	~200-1000	100-300
clusters	>10e14	>1000	100-400

The larger masses correspond to larger Einstein radii. This follows from Equation 2.1,

$$M = \theta_E^2 \left(\frac{c^2}{4G} \frac{D_d D_s}{D_{ds}} \right),$$

and is shown for our data in Figure 7.6.

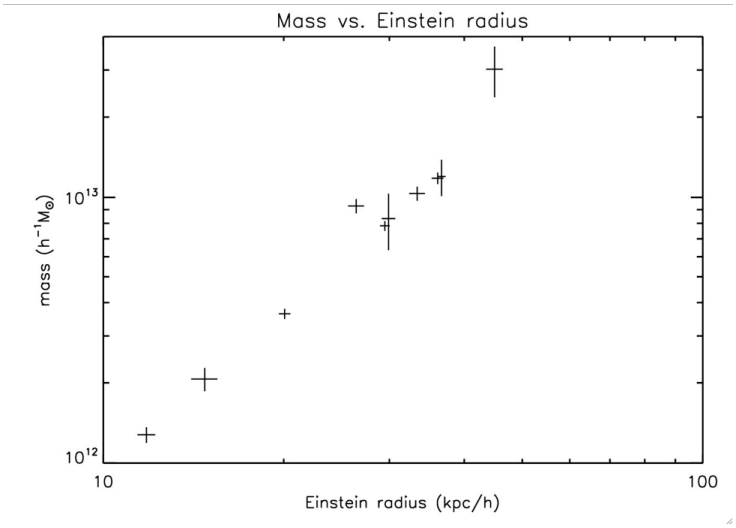

Figure 7.6 Mass vs. radius for our 10 lensing systems.

7.2.3 Luminosity as f(bandpass)

The *M/L* are greater for increasing wavelength,

$$\frac{M}{L_g} > \frac{M}{L_r} > \frac{M}{L_i} > \frac{M}{L_z} \text{ in units of } \frac{\mathrm{M}_\odot}{\mathrm{L}_\odot},$$

as can be seen in the four plots for *g, r, i, z* in Figures 7.4 and 7.5. This is a reflection of the fact that $L_{LRG} / L_\odot$ increases with wavelength. The Sun is a G star. Comparing the spectrum of a G star (which peaks at ~5000 Angstroms) to the spectrum of an elliptical galaxy (as an LRG) shown in Figure 7.7, it can be seen that the elliptical galaxy is redder than the Sun.

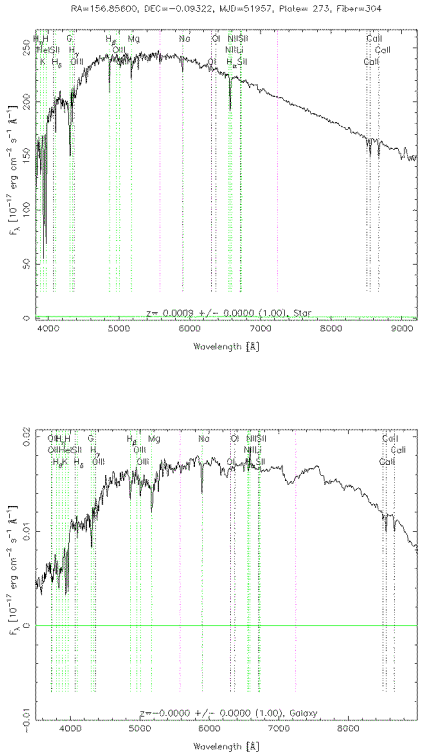

Figure 7.7 Spectrum of a G star (top), elliptical galaxy (bottom).

7.3 Comparison of Observed M/L Trends to Literature

We compare our data to four sets of *M/L* found in the literature. Bahcall et al. (1995) fit a function *M/L(R)* for elliptical galaxies to data from several sources that applied dynamical measurements. Our data plus three other sets of *M/L* data based on lensing, provide a comparison of methods that rely on dynamics and the associated assumptions (described in section 7.1.2), to lensing, which is free of these assumptions. Our data and two sets of *M/L* from the literature are based on strong lensing by galaxies (Keeton, et al.1998, Treu et al. 2006, Koopmans et al. 2006), and the third is based on weak lensing by galaxy groups (Parker, et al. 2005). Overall trends can be seen in the data shown in Figure 7.8. Details of each set of data and a discussion of how well they agree with one another are presented below.

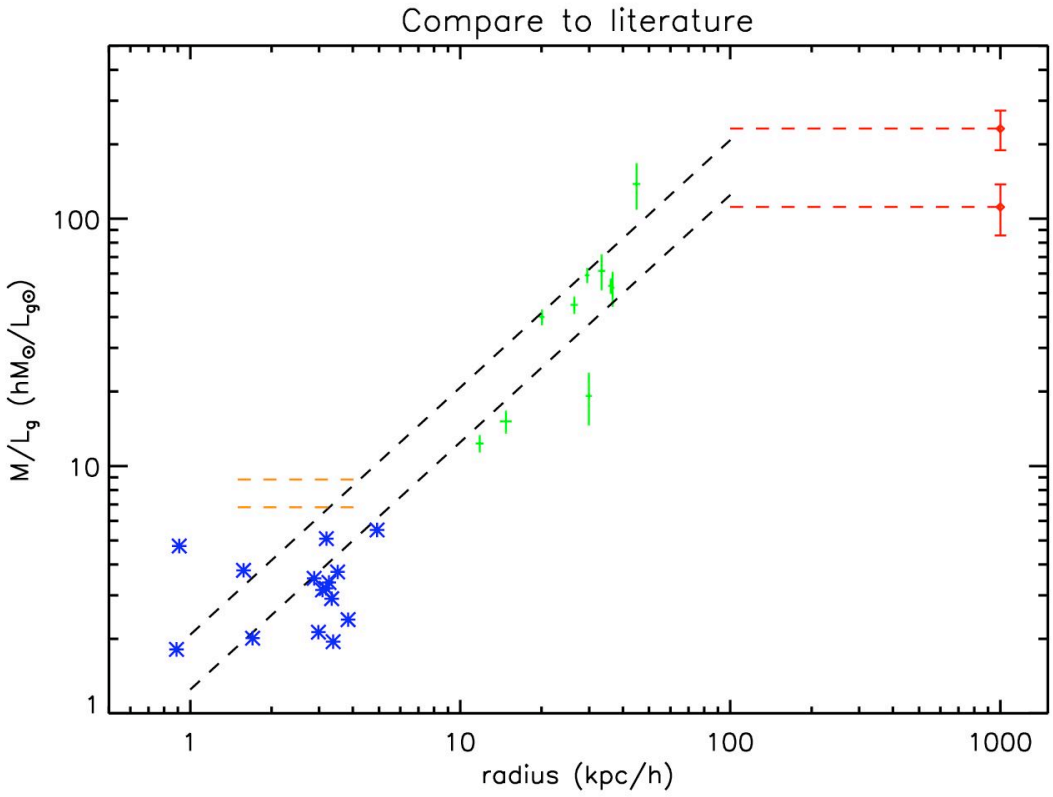

Figure 7.8 Thesis data (green) with data from the literature. Bahcall et al. 1995 (black dashed lines), SLACS 2006 (blue data points), Keeton et al. 1998 (orange dashed lines), Parker et al. 2005 (red data points for rich and poor groups and red dashed lines indicating range of rich and poor groups).

All of the comparison data are from observations in the Johnson-Morgan/Cousins filter system (*U, B, V*) while our data are from observations using the SDSS filter system (*u, g, r, i, z*). The factors required to convert mass to light ratios using *B* or *V* luminosities, M/L_B or M/L_V, to mass to light ratios in the *g* band, M/L_g are derived in the following section. Conversion to *g* band was chosen, as opposed to conversion to one of the other SDSS filters, because of all the SDSS filters (*u, g, r, i, z*), *g* band is most similar to *B* and *V* (Fukugita, et al. 1995).

An appropriate conversion must also be made if the comparison data assumed a cosmology different from the cosmology used in the analysis of our lensing systems: $H_0 = 100h$km/s/Mpc, $h = 1$, $\Omega_m = 0.3$, $\Omega_\Lambda = 0.7$. The required conversions will be described separately for each set of comparison data below.

7.3.1 Conversion from M/L_B and M/L_V to M/L_g

The factor to convert M/L_B to M/L_g (expressed in units of solar luminosity) is $n_{B\to g}$, where

$$n_{B\to g} \cdot \frac{M}{L_B/L_{B,\odot}} = \frac{M}{L_g/L_{g,\odot}}.$$

$$n_{B\to g} = \frac{\dfrac{M}{L_g/L_{g,\odot}}}{\dfrac{M}{L_B/L_{B,\odot}}} = \frac{\dfrac{L_B}{L_{B,\odot}}}{\dfrac{L_g}{L_{g,\odot}}} = \frac{\dfrac{L_B}{L_g}}{\dfrac{L_{B,\odot}}{L_{g,\odot}}} \qquad \text{Equation 7.1}$$

where

$$\frac{L_B}{L_g} = 10^{\frac{-M_B + M_g}{2.5}}$$

and

$$\frac{L_{B,\odot}}{L_{g,\odot}} = 10^{\frac{-M_{B,\odot} + M_{g,\odot}}{2.5}}.$$

From Table 3 of Fukugita, et al. (1995), for elliptical galaxies in the rest frame, $\mathrm{M}_g - \mathrm{M}_B = -0.55$, where M is absolute magnitude (to differentiate it from italicized *M,* which is *mass*):

$$\frac{L_B}{L_g} = 10^{\frac{-0.55}{2.5}} = 0.602.$$

From the SDSS website, $\mathrm{M}_{g,\odot} = 5.12$ and $\mathrm{M}_{B,\odot} = 5.47$:

$$\frac{L_{B,\odot}}{L_{g,\odot}} = 10^{\frac{-5.47+5.12}{2.5}} = 0.724.$$

With these values, Equation 7.1 yields resultant conversion factor:

$$n_{B\to g} = \frac{\frac{L_B}{L_g}}{\frac{L_{B,\odot}}{L_{g,\odot}}} = \frac{0.602}{0.724} = 0.832.$$

The factor to convert M/L_V to M/L_g is derived analogously using the values for elliptical galaxies in the *V* band from Fukugita, et al. (1995), $\mathrm{M}_g - \mathrm{M}_B = -0.55$ and $\mathrm{M}_B - \mathrm{M}_V = 0.95$ yielding $\mathrm{M}_g - \mathrm{M}_V = 0.41$ and

$$\frac{L_V}{L_g} = 10^{\frac{0.41}{2.5}} = 1.459.$$

From the SDSS website, $\mathrm{M}_{g,Sun} = 5.12$ and $\mathrm{M}_{V,Sun} = 4.82$:

$$\frac{L_{V,\odot}}{L_{g,\odot}} = 10^{\frac{-4.82+5.12}{2.5}} = 1.318.$$

With these values, the resultant conversion factor is

$$n_{V\to g} = \frac{\frac{L_V}{L_g}}{\frac{L_{V,\odot}}{L_{g,\odot}}} = \frac{1.459}{1.318} = 1.11.$$

These are not big corrections. M/L_B differs from M/L_g by -17%, while M/L_V differs from M/L_g by +11%. In other words, $M/L_g = 0.83 \cdot M/L_B$ and $M/L_g = 1.11 \cdot M/L_V$. The correction from *B* to *g* is slightly larger than the correction required for *V* to *g*.

7.3.2 Comparison to Bahcall, et al.

Bahcall, et al. present *M/L* as a function of scale for spiral and elliptical galaxies, groups, and clusters (Bahcall et al. 1995). Since the M/L found in this thesis are for elliptical galaxies, these *M/L* will be compared to the function Bahcall et al. present for ellipticals:

$$\frac{M}{L_B} = (200 \pm 50)\left(\frac{R}{0.1h^{-1}Mpc}\right)h\left(\frac{M}{L}\right)_{Sun}.$$

The function is a fit to the data from several types of observations. On luminous matter and gas-dominated scales, *M/L* were determined from the virial mass based on the velocities of stars. Beyond the luminous region, mass is estimated by the motion of satellites around the galaxies The data for scales $\geq$20 kpc are based on observations of extended x-ray halos, assuming that the x-ray gas is gravitationally bound to the galaxy.

Bahcall et al. converted all data to a consistent set of units, with $H_0 = 100h$ km s^{-1} Mpc^{-1}, and all luminosities refer to the total luminosity in the blue (*B*) band, corrected for galactic and internal extinction and redshift. Although the values of H_0 are the same as used for our analysis ($H_0 = 100h$km/s/Mpc), the observed bands differ. Converting Bahcall's M/L_B to M/L_g via multiplying by the factor 0.83 derived in Section 7.4.1 yields

$$\frac{M}{L_B} = (0.83)(200 \pm 50)\left(\frac{R}{0.1h^{-1}Mpc}\right)h\left(\frac{M}{L}\right)_{Sun}.$$

The high and low ranges of this function are plotted in Figure 7.8 (black dashed lines) from the smallest ($R \sim 1$ kpc) to the largest ($R \sim 100$ kpc) observed extent of the individual elliptical galaxies. A subset of their data includes measurements at different radii of the same galaxy. The increasing *M/L* with *R* implies that there is more matter beyond the luminous range of the galaxies. This is consistent with the *M/L* derived from our lensing systems (Figure 7.8).

Bahcall et al. also present evidence that the trend of increasing *M/L* with *R* stops at about 200 kpc. Beyond this scale, M/L of groups and clusters appears to flatten rather than increase with scale. Bahcall et al. suggest that for elliptical galaxies, most of the dark matter resides in large galaxy halos with $R \sim 100$ kpc and that the mass of groups and clusters may be accounted for by the mass of the individual member galaxies, including their dark matter halos and intracluster gas.

The flattening of the M/L curve is supported by the data from Parker, et al. (2005), which is discussed in Section 7.3.5.

7.3.3 Comparison to SLACS

The Sloan Lens ACS (SLACS) Survey is a spectroscopic and imaging survey of galaxy-scale strong gravitational lenses. Lens candidates are selected spectroscopically from the SDSS database of galaxy spectra. Selected targets show multiple nebular emission lines at a redshift significantly higher than the SDSS target galaxy, where it is hoped that these lines indicate the presence of a distant lensed

source. Like our search for lensing system around LRGs and BCGs, the SLACS survey is optimized to detect bright, early type lens galaxies. The difference is that we used photometric data to select on specific colors, while SLACS used spectroscopic data to select on the presence of specific spectral lines.

Spectra for the SDSS are obtained with 3-arcsecond diameter spectroscopic fibers. Therefore, the arcs detected by SLACS must be contained within the fiber radius, limiting the Einstein radii to about 1.5 arcseconds. This scale provides a nice comparison to the Bahcall *M/L(R)* function at scales smaller than our data. The radii and surface brightness of the SLACS candidate systems were obtained from follow-up observations using the Advanced Camera for Surveys (ACS) aboard the Hubble Space Telescope (HST). Treu et al. (2006) and Koopmans et al (2006) estimated the mass enclosed by the Einstein radii from lens modeling.

Treu et al. (2006) and Koopmans et al (2006) provide the magnitude, Einstein radius, and the mass within the Einstein radius for each of 15 systems (Table 7.2). To determine the *M/L* for each system we needed to calculate the luminosity from the given magnitude. The SLACS data includes observations in both *B* and *V* bands. Since the correction required to convert to *g* band is smaller for *V* than for *B* (Section 7.4.3), we chose to calculate the *V* band luminosity. The *V* band luminosity (in units of solar luminosity) was calculated via

$$\frac{L_V}{L_{V,Sun}} = 10^{\frac{-M_V + M_{V,Sun}}{2.5}}$$

and is shown in column 4 of Table 7.2. The conversion from *V* band to *g* band (multiplication by 1.11),

$$\frac{M/M_{Sun}}{L_g/L_{g,Sun}} = 1.11\frac{M/M_{Sun}}{L_V/L_{V,Sun}},$$

is shown in column 6.

The SLACS Survey used $H_0 = 70\text{km/s/Mpc}$, while we used $H_0 = 100\text{km/s/Mpc}$, so *M/L* [$h\text{M}_{\text{Sun}}/\text{L}_{\text{g,Sun}}$] was scaled by 1/0.7 (column 7 of Table 7.2) and the radius, R[h^{-1} kpc] was scaled by 0.7 (column 9 of Table 7.2) to make the SLACS data consistent with our data. They used $\Omega_m = 0.3$, $\Omega_\Lambda = 0.7$, as we did, so no additional scaling for cosmology was required.

The *M/L* are plotted in Figure 7.8. They follow the overall trend of decreasing *M/L* as the scale decreases.

Table 7.2 SLACS data. (Treu et al. 2006, Koopmans et al. 2006)

Lens Name	V	M_Ein (Msun)	L_V (L_Vsun)	M/L_V (Msun/L_Vsun)	n*M/L_V (Msun/Lg_sun)	(1/0.7)*n*M/L_V (Msun/Lg_sun)	R_Ein (kpc)	0.7*R_Ein (kpc)
SDSS J003753.21-094220.1...	-23.11	2.73E+11	1.49E+11	1.835	2.037	2.910	4.77	3.339
SDSS J021652.54-081345.3...	-23.94	4.82E+11	3.20E+11	1.508	1.674	2.392	5.49	3.843
SDSS J073728.45+321618.5...	-23.69	3.12E+11	2.54E+11	1.229	1.364	1.949	4.83	3.381
SDSS J091205.30+002901.1...	-23.41	3.96E+11	1.96E+11	2.019	2.241	3.202	4.55	3.185
SDSS J095629.77+510006.6...	-23.17	3.70E+11	1.57E+11	2.353	2.612	3.731	5.02	3.514
SDSS J095944.07+041017.0...	-21.45	7.70E+10	3.22E+10	2.388	2.650	3.786	2.25	1.575
SDSS J125028.25+052349.0...	-23.05	1.89E+11	1.41E+11	1.343	1.490	2.129	4.26	2.982
SDSS J133045.53-014841.6...	-20.25	3.20E+10	1.07E+10	2.997	3.326	4.752	1.3	0.91
SDSS J140228.21+632133.5...	-23.06	3.03E+11	1.42E+11	2.133	2.367	3.382	4.66	3.262
SDSS J142015.85+601914.8...	-21.51	3.90E+10	3.41E+10	1.144	1.270	1.815	1.27	0.889
SDSS J162746.44-005357.5...	-22.68	2.22E+11	1.00E+11	2.217	2.461	3.516	4.11	2.877
SDSS J163028.15+452036.2...	-23.09	5.08E+11	1.46E+11	3.478	3.860	5.515	7.03	4.921
SDSS J230053.14+002237.9...	-22.62	3.04E+11	9.47E+10	3.209	3.562	5.088	4.56	3.192
SDSS J230321.72+142217.9...	-23.03	2.75E+11	1.38E+11	1.990	2.209	3.155	4.41	3.087
SDSS J232120.93-093910.2...	-22.59	1.17E+11	9.22E+10	1.270	1.409	2.013	2.43	1.701

7.3.4 Comparison to Keeton et al.

Keeton et al. (1998) combined photometry and lens modeling to 17 gravitational lens galaxies between z~0.1 and z~1.0. Most of the galaxies were early type, providing a nice comparison to our sample of lensing LRGs. Keeton fit the lensing data to the function

$$\log\ M/L_B(z) = \log M/L_B(0) + z[d(\log M/L_B)/dz] + ...$$

and provide values for each term as a function of several cosmologies. As none of their cosmologies match ours ($\Omega_m = 0.3,\ \Omega_\Lambda = 0.7$), we averaged the results they give for $\Omega_m = 0.4,\ \Omega_\Lambda = 0.6$ and $\Omega_m = 0.2,\ \Omega_\Lambda = 0.8$. The average is shown the last row of Table 7.3. Using z=0.4, which is the typical lens redshift in our data, results in the M/L_B shown in column 4 of Table 7.3. Keeton used observations in *B* band, so the M/L_B was converted to M/L_g (column 5 of Table 7.3) as described in Section 7.3.1. This M/L_g is shown on Figure 7.8. The indicated range of radii was derived from examination of the range of Einstein radii Keeton et al. present for systems at z~0.4. The indicated range of *M/L* indicates the error on the fits given the errors reported by Keeton et al. Keeton et al. did not provide M and L data for the individual systems, so only their fit, rather than an *M/L* for each system (as for SLACS), could be plotted.

Table 7.3 Empirical results. (Top rows, Keeton et al. 1998) and average for the desired cosmology,

Ω_m,Ω_Λ	$\log M/L_B(0)$	$d(\log(M/L_B)dz$	M/L_B	M/L_g
0.4,0.6	1.19 ± 0.04	-0.53 ± 0.08	9.50	7.89
0.2,0.8	1.19 ± 0.04	-0.65 ± 0.08	8.51	7.063
0.3,0.7	---	---	---	7.474

The Keeton et al. range is for a scale similar to those of the SLACS survey, consistent with the trends observed by SLACS.

7.3.5 Comparison to Parker et al.

Parker et al. (2005) present *M/L* of galaxy groups from a weak lensing study of 116 Canadian Network for Observational Cosmology (CNOC2) galaxy groups. They estimate that galaxy groups have a mean *M/L* of $185\pm28\ h\ M_{Sun}/L_{B,Sun}$ within $1\ h^{-1}$ Mpc and that this *M/L* is constant as the distance from the group center increases for scales from 100 kpc to 1 Mpc. They also found that, when their sample was sorted into rich and poor galaxy groups, rich groups have a larger *M/L* than the poor groups, $M/L_B=278\pm42(hM_{Sun}/L_{B,Sun})$ and $M/L_B=134\pm26(hM_{Sun}/L_{B,Sun})$, respectively. This range of *M/L* and the independence of *M/L* on *R* is shown in Figure 7.8 (red dashed lines representing *M/L* for rich and poor groups). Since Parker's observations were in *B* band, their data was converted to *g* band using the method described in Section 7.3.1. Parker used $H_0=100$km/s/Mpc, $h=1$, $\Omega_m=0.3,$ and $\Omega_\Lambda=0.7$, as we did, so no scaling for cosmology was required.

Our larger mass lensing systems are of the scale of poor groups, with *M/L* approaching ~100 hM/L_{Sun}, consistent with the *M/L* found by Parker et al. for poor groups.

Ryden (2003) says typical *M/L* for clusters lie in the range of 200-300 M/L_B, citing Coma as a typical example. As rich groups approach the size of small clusters, this is consistent with the values of the rich groups from Parker et al.

7.4 Discussion of Results

Our study complements existing strong lensing research in several ways.

7.4.1 Demonstration of Search Method

We have shown that interesting strong lensing systems can be filtered out of a huge database, like that of the SDSS, by application of a search based on color cuts. Fourteen candidate lensing systems were singled out by manual inspection of a subset of the systems returned by our query. Perhaps more strong lensing systems would be found if we inspected the balance of the systems returned, those systems with only one or two blue objects within the 10-arcsecond search radius.

This raises the question of how many strong lens systems we expected to find. This is a question of active study in the field of strong lensing. All of the lensing systems we found were at nearly the same redshift, $z\sim0.4$. Gladders et al. (2003) found disagreement with theoretical predictions in the results to their search for strong lensing clusters in the Red-Sequence Cluster Survey (RCS). Estrada et al. (2007) have found a pronounced drop in the cross section for arc production by clusters at $z<0.3$.

7.4.2 The "Einstein Radius Method"

We have shown that a good approximation of the mass of strong lensing systems with nearly symmetric arcs can be found by the Einstein radius method. Two of the systems analyzed by the Einstein radius method were also analyzed by L. Buckley-Geer and H. Lin using a more sophisticated modeling technique, gravlens/lensmodel (Keeton 2001). Such modeling requires accurate photometry and has the capability of modeling more complicated mass distributions than the SIS. For example, they used a singular isothermal ellipse (SIE) to model the mass distribution. The lens masses derived from gravlens/lensmodel are in good agreement with those found by the Einstein radius method (Table 7.4).

Table 7.4 Comparison of masses derived from the "Einstein radius method" to those from gravlens/lensmodel.

Lensing system	gravlens/lensmodel	Einstein radius method
8 o'clock	1.35×10^{12} $h^{-1}M_{\odot}$	$(1.26 \pm 0.09) \times 10^{12}$ $h^{-1}M_{\odot}$
lrg_2_2811	1.98×10^{12} $h^{-1}M_{\odot}$	$(1.94 \pm 0.20) \times 10^{12}$ $h^{-1}M_{\odot}$

By avoiding detailed modeling that often requires information from time-consuming follow-up observations, the Einstein method yields more *M/L* statistics.

7.4.3 Comparison to Literature

The systems discovered by our search enhance the detailed study of distant star-forming galaxies, like LBGs, by adding to currently limited statistics. The range of *M/L* found (~10-140 $hM_{\odot}/L_{\odot}$) helps fill in the gap in *M/L* statistics from lensing for the intermediate mass range ($10^{12} - 10^{13}$ $h^{-1}M_{\odot}$). This is important for understanding the formation of large-scale structure.

The search radius determines the scale of the systems returned by our query. As a next step, we propose to search at larger radii with the hope of discovering more star-forming galaxies and more massive systems to add *M/L* statistics in the range of poor to rich groups and clusters.

REFERENCES

Adelberger, K. L., 2002 PhD thesis Caltech

Adelman-McCarthy, J. K., et al. 2006, ApJS, 162, 38

Adelman-McCarthy, J. K., et al. 2007, ApJS, in press

Allam, S. S., et al. 2007, ApJ Letters, 662, L51

Bahcall, N. A., et al. 1995, ApJ, 447, L81

Baker, A. J., et al. 2004, ApJ, 613, L113

Bruzual, A. G., et al. 1993, ApJ, 405, 538

Cabanac, R. A., et al. 2007, A&A 461, 813

Carlstrom, J. E., et al. 2002 Annual Review of Astronomy & Astrophysics, 40, 643

Clayton, D. D. *Principles of Stellar Evolution and Nucleosynthesis* (University of Chicago Press, Chicago, IL USA 1983)

Coleman, G. D., et al. 1980, ApJS, 43, 393

Dodelson, S. *Modern Cosmology* (Academic Press USA 2003)

Ebbels, T, et al. 1998, Mon. Not. R. Astron. Soc. 295, 75

Eisenstein, D. J., et al. 2001, ApJ, 122, 2267

Estrada, J., et al. 2007, ApJ, 660, 1176

Fernie, J. D., 2005, American Scientist, 93,104

Fukugita, M., et al. 1995, PASP, 107, 945

Gladders, M. D., et al. 2003, ApJ, 593, 48

Hansen, S. M., et al. 2005, ApJ, 633, 122

Hennawi, J. F., et al. 2006, AJ, submitted, astro-ph/0610061

Hewitt, J. N., et al. 1988, Nature, 333,537

Hogg, D. W., 2000, astro-ph/9905116

Keeton, C. R., et al. 1998, ApJ, 509, 561

Keeton, C. R. 2001, ApJ, 561, 46

Kling, T. P., et al. 2000, Phys. Rev. D 62

Kochanek, C. S. 2004, astro-ph/0407232v1

Koester, B. P., et al. 2007a, astro-ph/0701265v1

Koester, B. P., et al. 2007b, astro-ph/0701268v1

Koopmans, L. V. E., et al. 2006 ApJ, 649, 599

Luppino, G. A., et al. 1999 A&AS, 136, 117

Lynds, R., and Petrosian, V. 1986 Bull. Am. Astron. Soc., 18, 1014

Madau, P. 1995, ApJ, 441, 18

Mollerach, S. and Roulet, E., *Gravitational Lensing and Microlensing* (World Scientific, Singapore, 2002)

Narayan, R. and Bartelmann, M., 1997, astro-ph/9606001v2

Nesvadba, N. P. H., et al. 2006, astro-ph/0606527

Oke, J. B. and Gunn, J. E., 1983 ApJ, 266, 713

Parker, L. C., et al. 2005 ApJ, 634, 806

Peacock, J. A., *Cosmological Physics* (Cambridge University Press, Cambridge, UK, 2003)

Pettini, M., et al., 2002 ApJ, 569, 572

Ryden, B., *Introduction to Cosmology* (Addison Wesley, San Francisco, 2003)

Schlegel, D. J., et al. 1998 ApJ, 500, 525

Shapley, A. E., et al. 2006, astro-ph/0606635

Soucail, G., Fort, B., Mellier, Y., & Picat, J. P.,1987, Astronomy and Astrophysics, 172, L14-L16

Spergel, D. N., et.al. 2007, ApJS, 170, 377

Steidel, C. C., et al. 2003, ApJ, 592, 728

Strauss, M. A, et al. 2002 Astron.J. 124, 1810

Teplitz, H. I., et al. 2000 ApJ, 533, L65

Treu, T., et al. 2006 ApJ, 640, 662

Turner, E. L., et al. 1984, ApJ, 284, 1

Walsh, D., Carswell, R. F., Weymann, R. J., 1979, Nature, 279, 382

Weisberg, J. M., et al. 2005, Science, 309, 71

Yee, H. K., et al. 1996, AJ, 111, 1783

APPENDIX A

IMAGES OF THE LENSING SYSTEMS

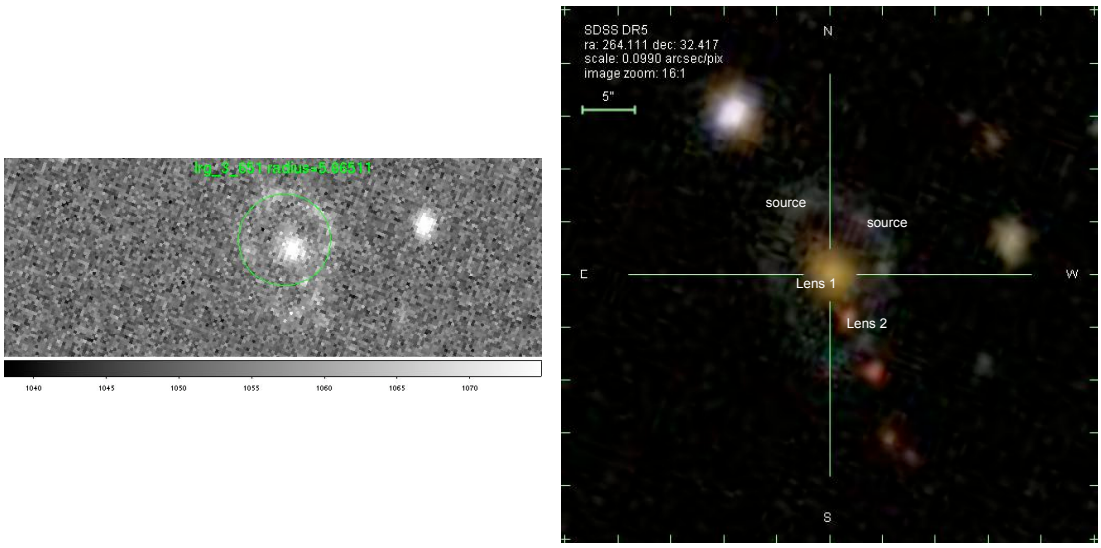

lrg_3_651

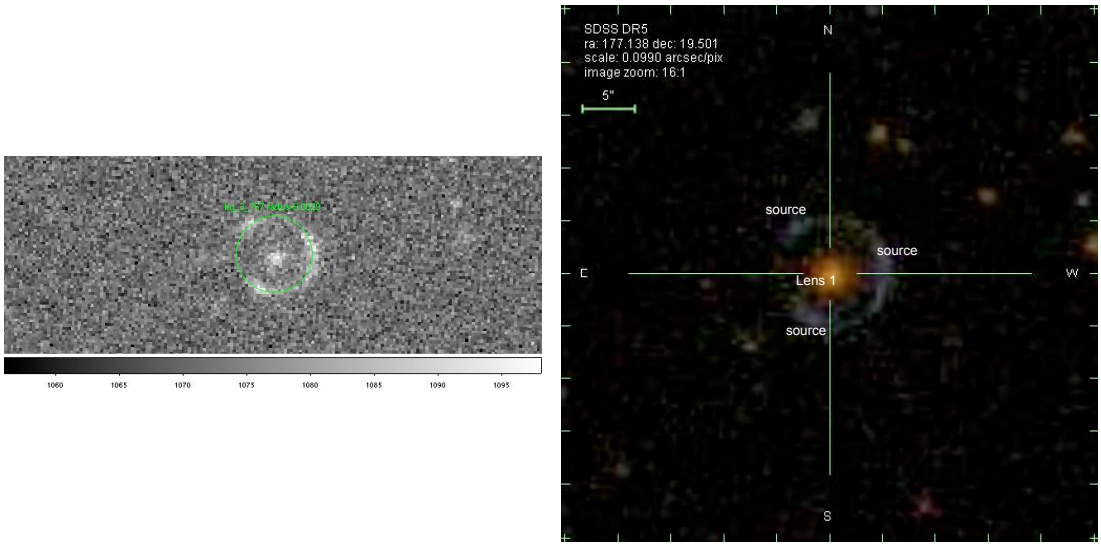

lrg_3_757

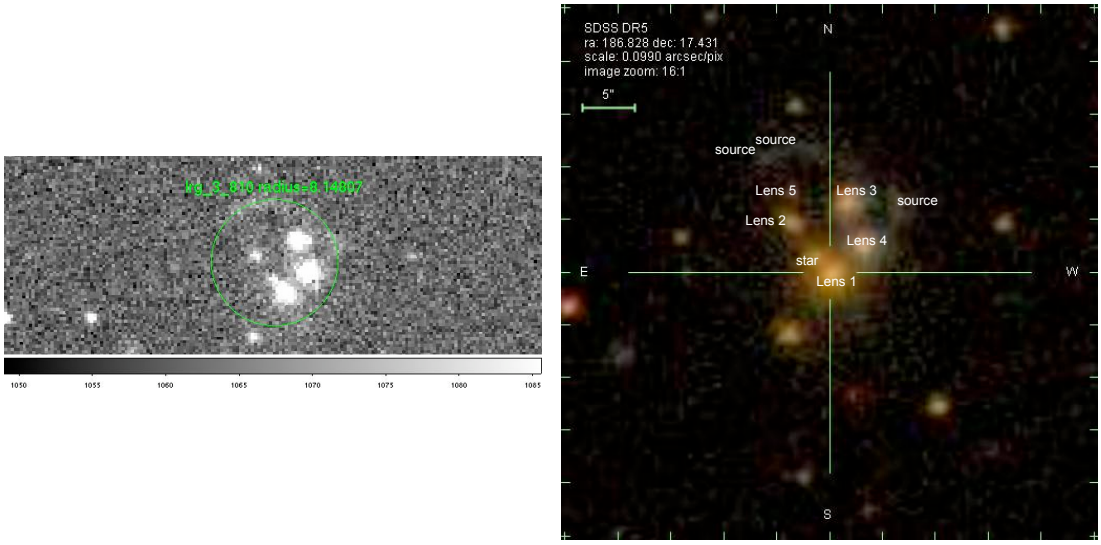

lrg_3_810

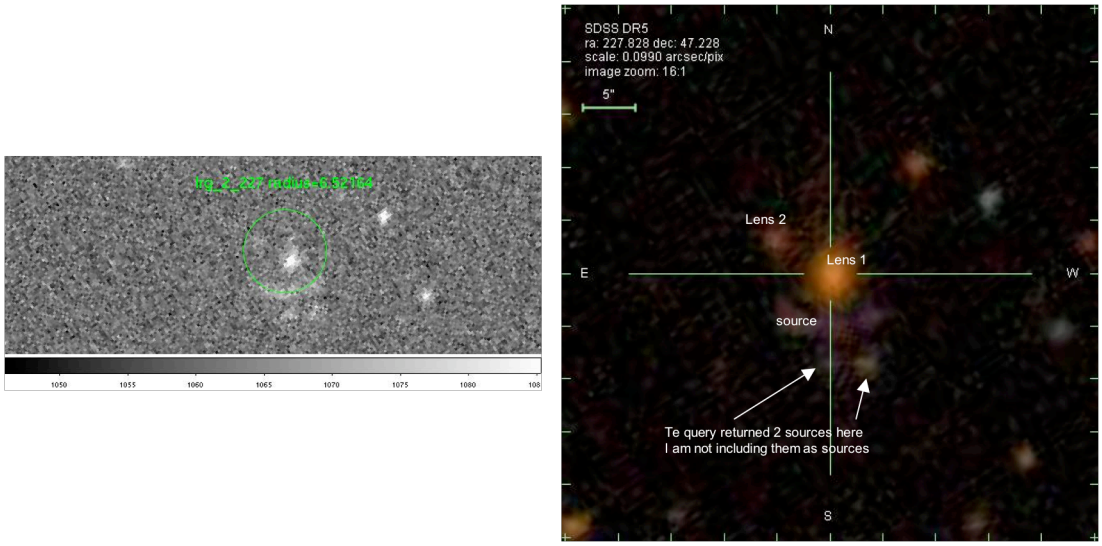

lrg_3_227

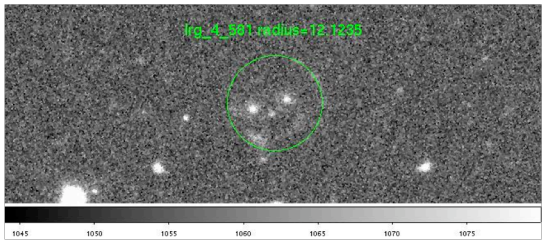

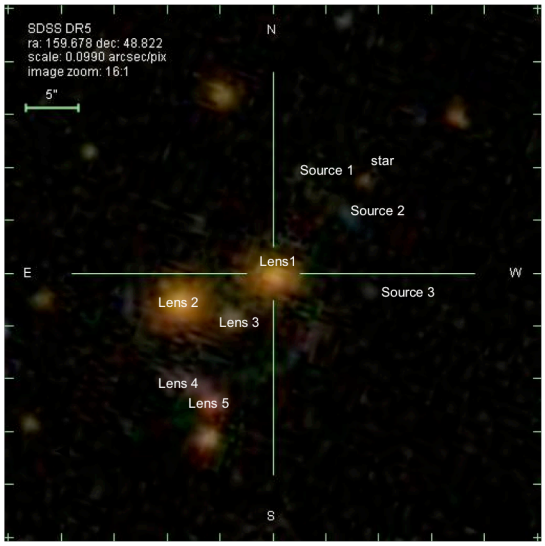

lrg_4_581a

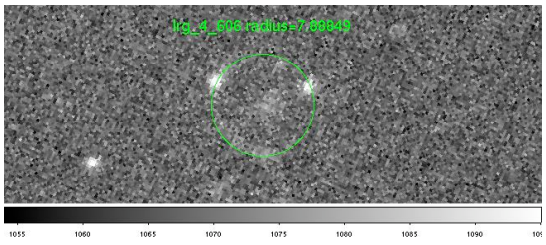

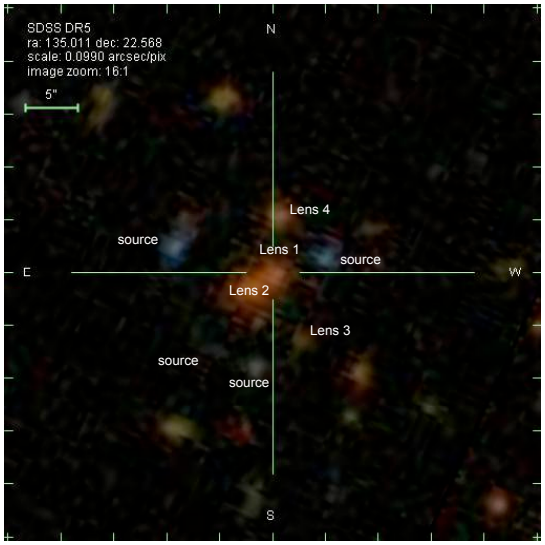

lrg_4_606

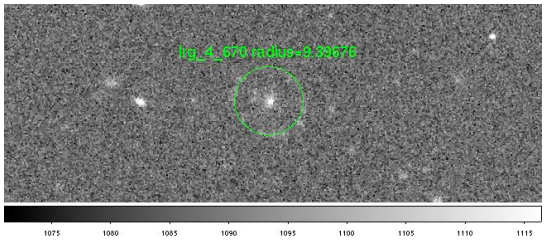

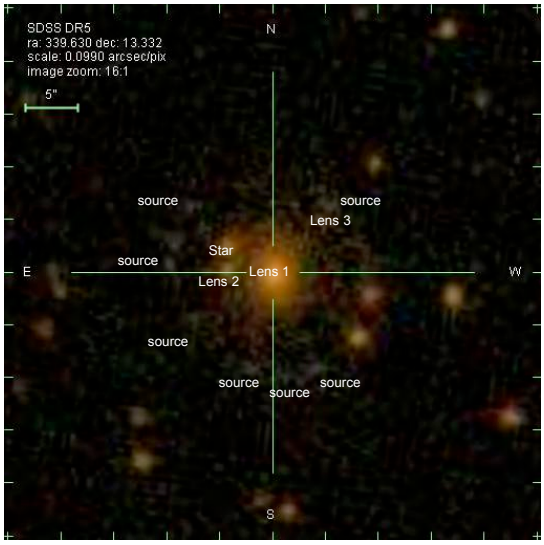

lrg_4_670

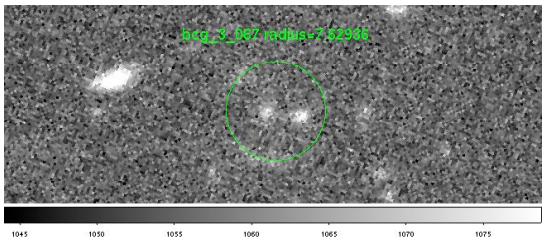

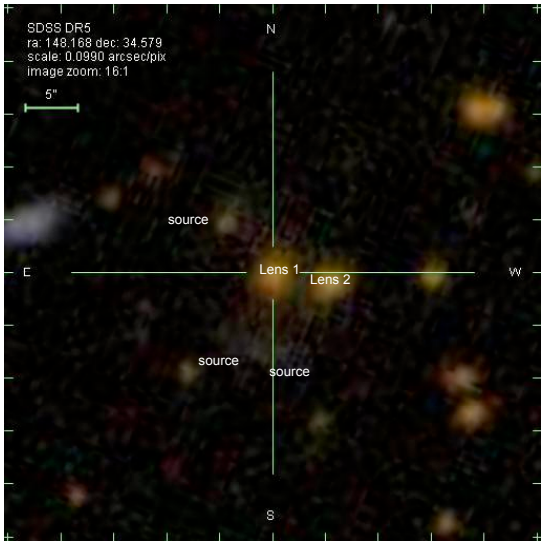

bcg_3_067

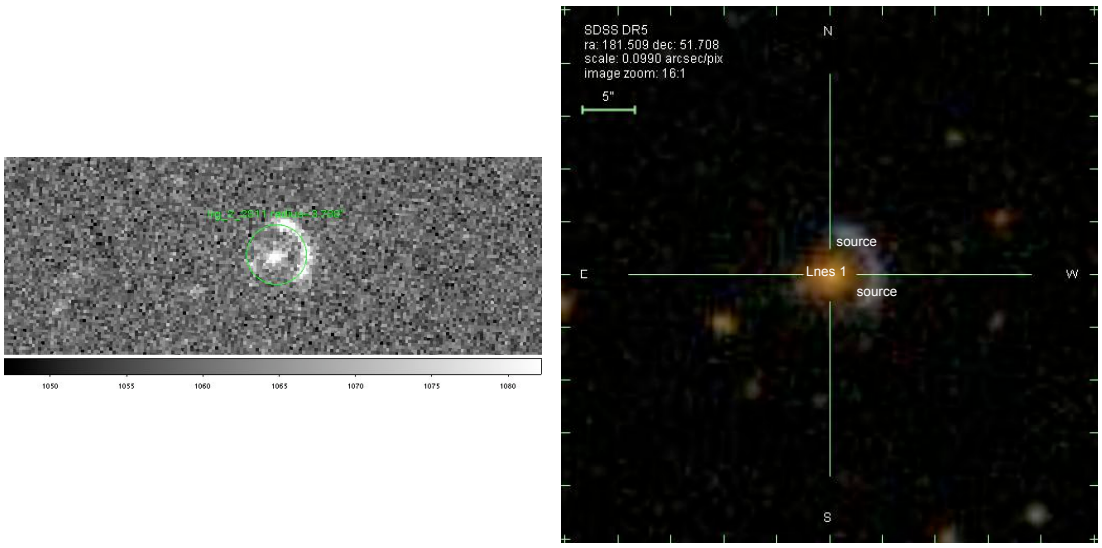

lrg_2_2811

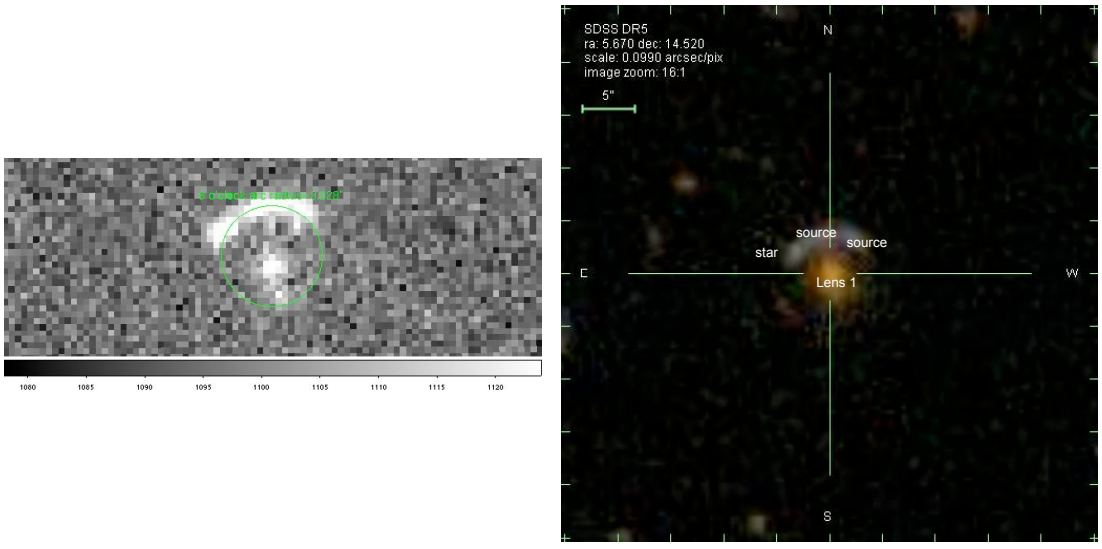

8 o’clock arc

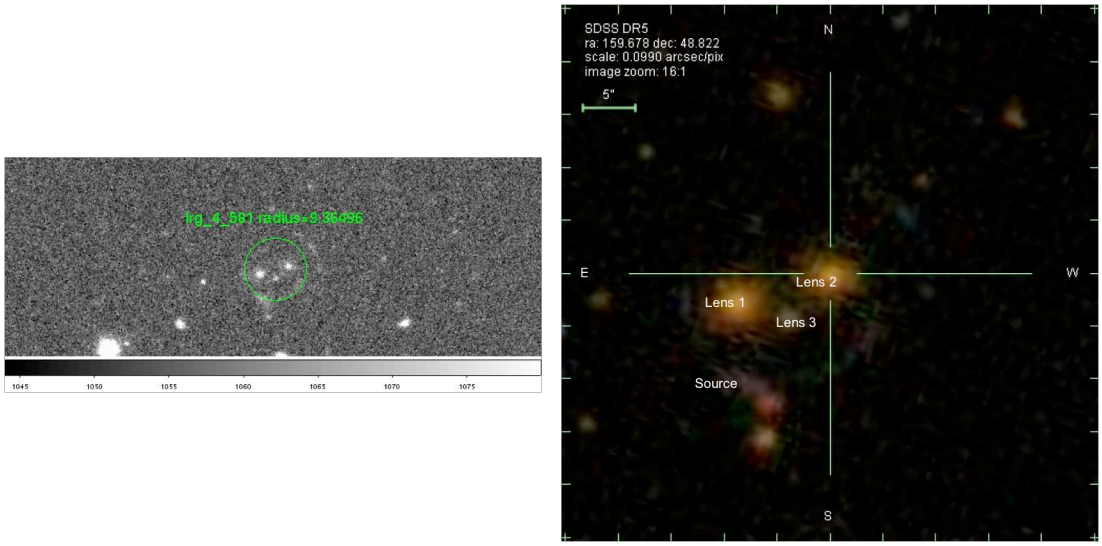
lrg_4_581 radius=9.56496
1045
1050
1055
1060
1065
1070
1075
SDSS DR5
ra: 159.678 dec: 48.822
scale: 0.0990 arcsec/pix
image zoom: 16:1
5"
N
E
W
S
Lens 2
Lens 1
Lens 3
Source

lrg_4_581b

APPENDIX B

GALAXY MODEL CURVES

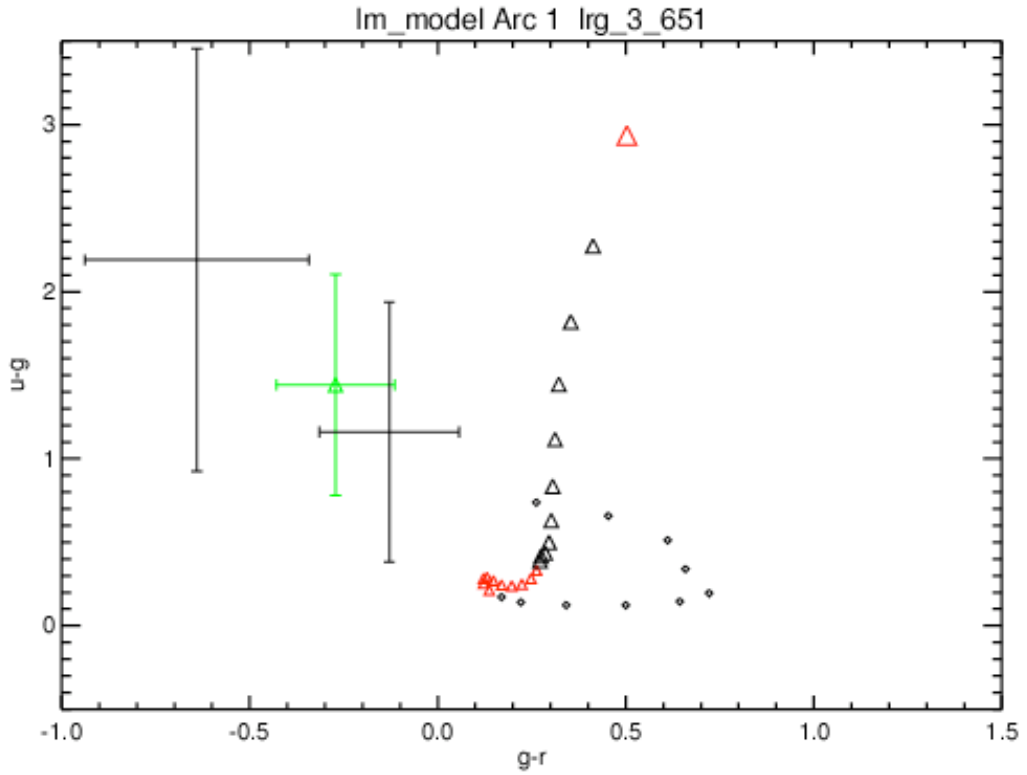
lm_model Arc 1 lrg_3_651
u-g
g-r
3
2
1
0
-1.0
-0.5
0.0
0.5
1.0
1.5

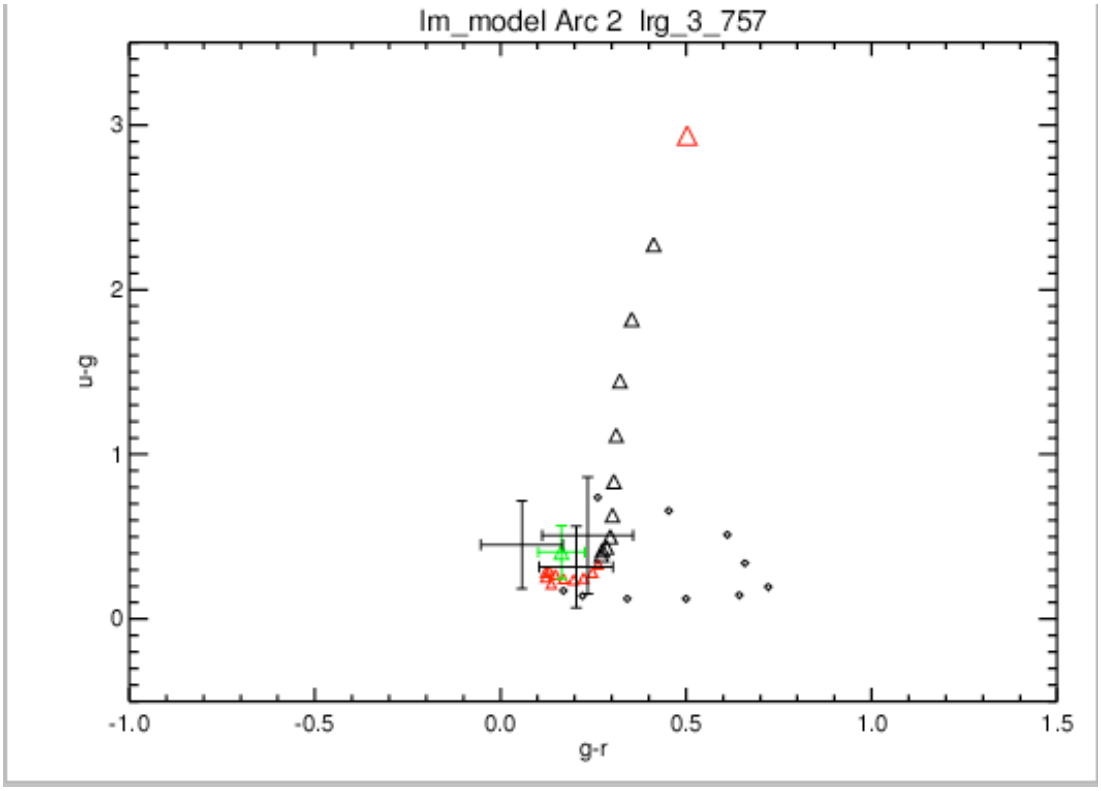
lm_model Arc 2 lrg_3_757
u-g
g-r
3
2
1
0
-1.0
-0.5
0.0
0.5
1.0
1.5

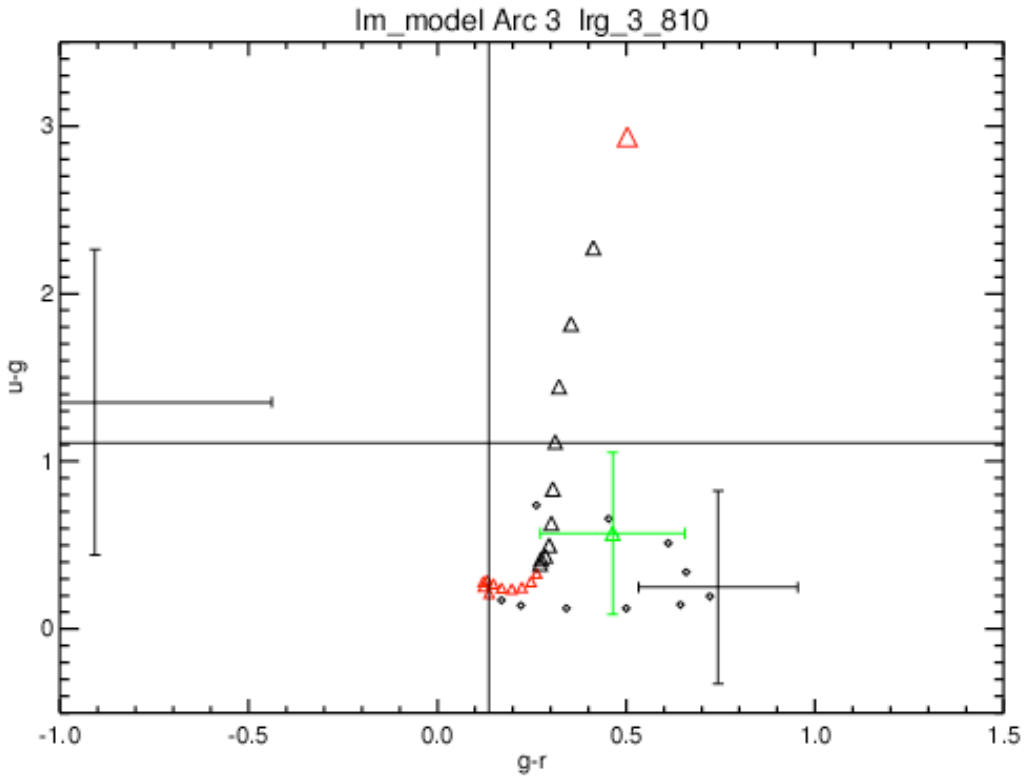
lm_model Arc 3 lrg_3_810
u-g
g-r
3
2
1
0
-1.0
-0.5
0.0
0.5
1.0
1.5

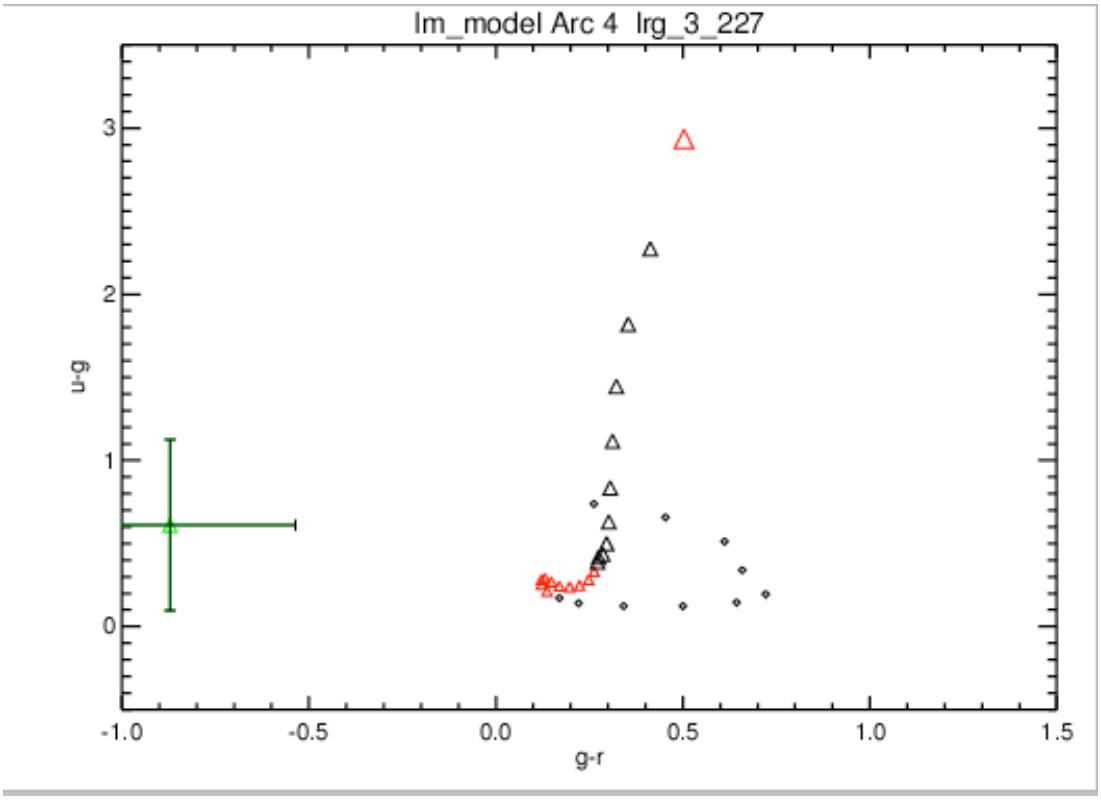
lm_model Arc 4 lrg_3_227
u-g
g-r
3
2
1
0
-1.0
-0.5
0.0
0.5
1.0
1.5

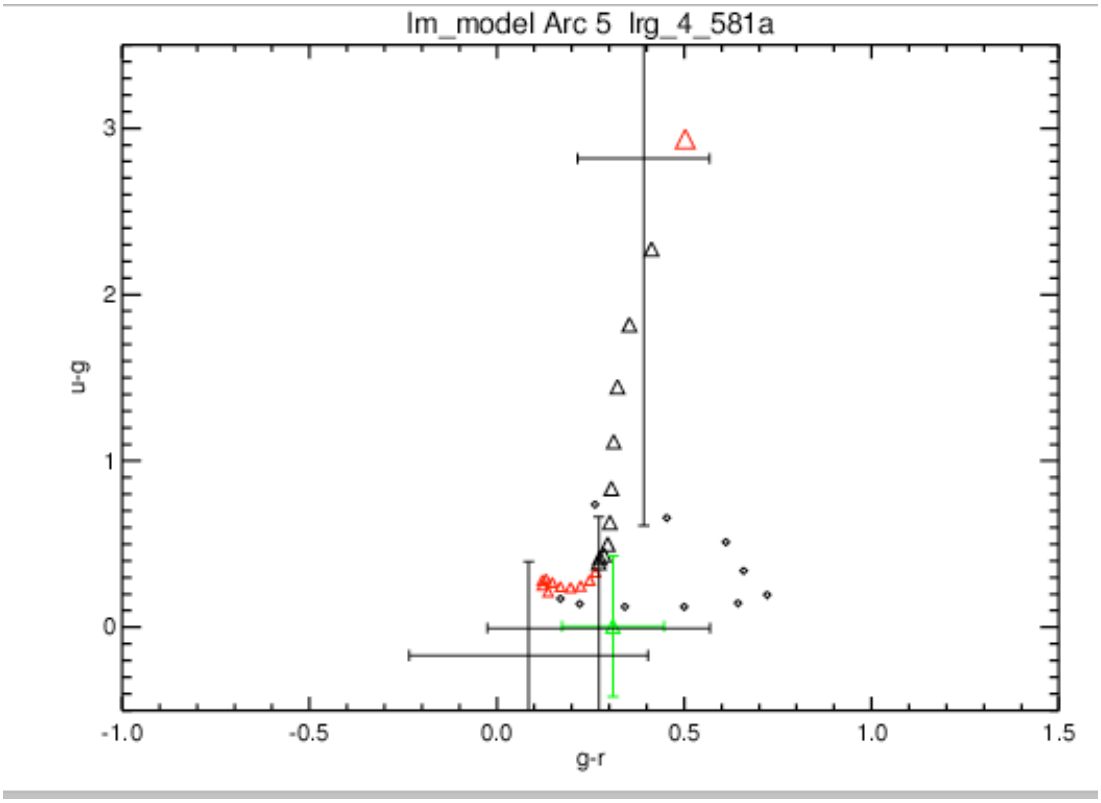
lm_model Arc 5 lrg_4_581a
u-g
g-r
3
2
1
0
-1.0
-0.5
0.0
0.5
1.0
1.5

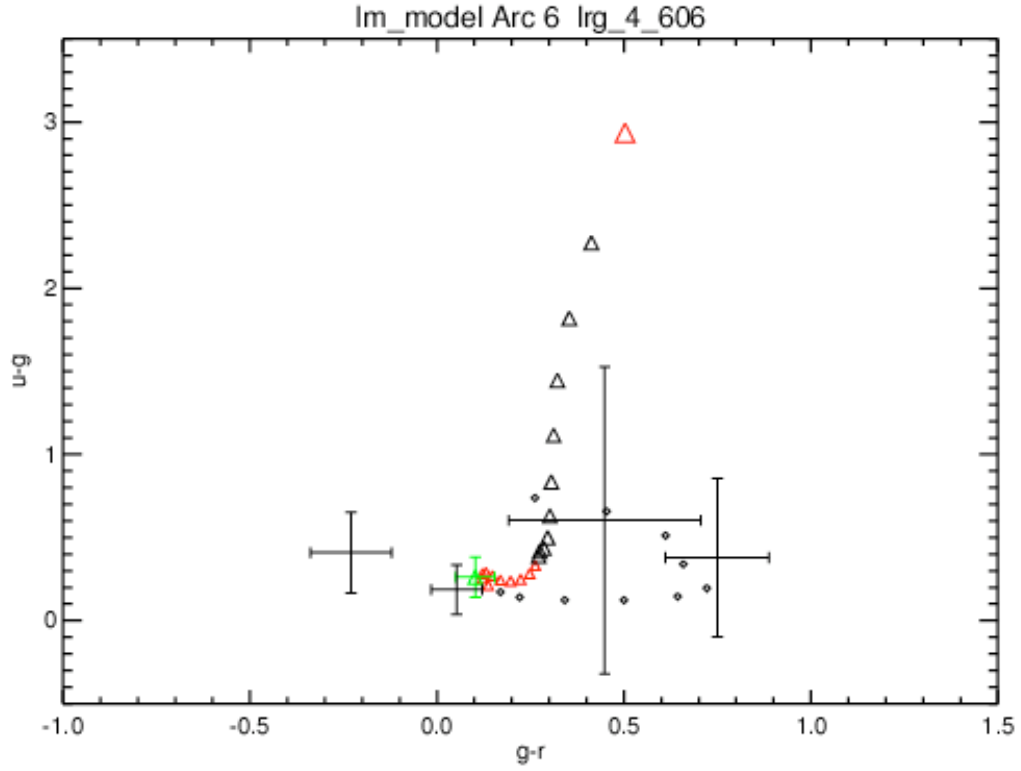
lm_model Arc 6 lrg_4_606
u-g
g-r
3
2
1
0
-1.0
-0.5
0.0
0.5
1.0
1.5

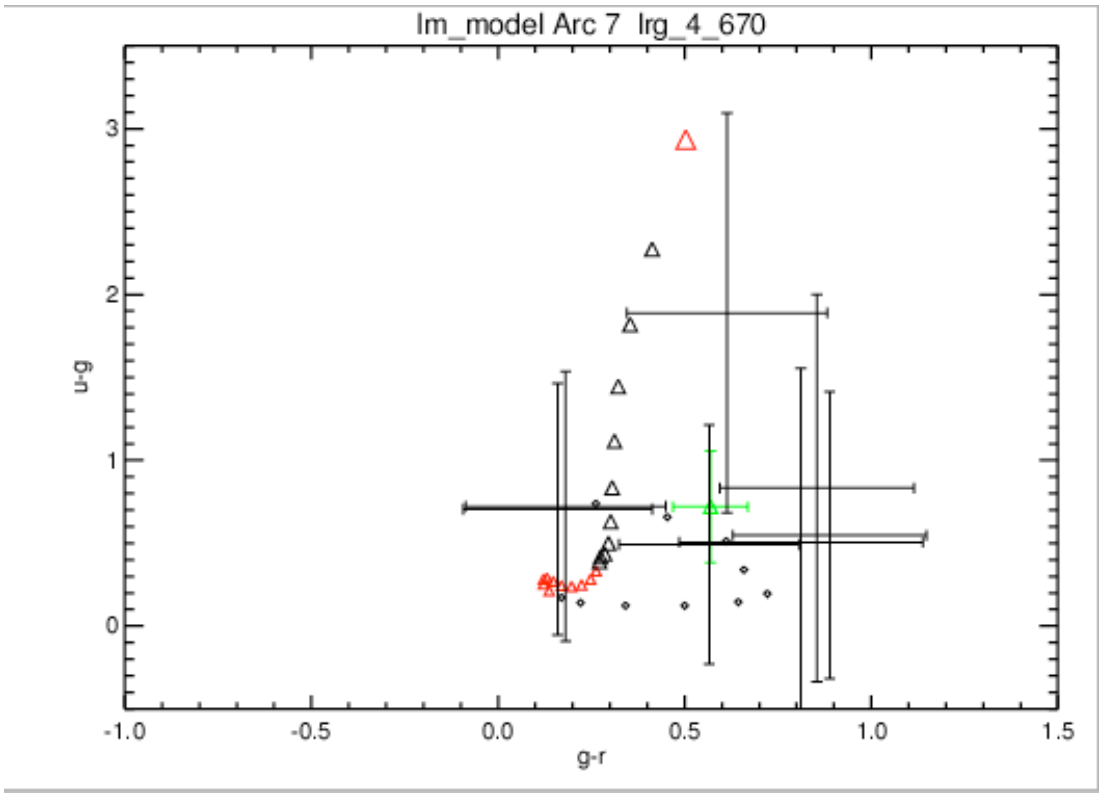
lm_model Arc 7 lrg_4_670
u-g
g-r
3
2
1
0
-1.0
-0.5
0.0
0.5
1.0
1.5

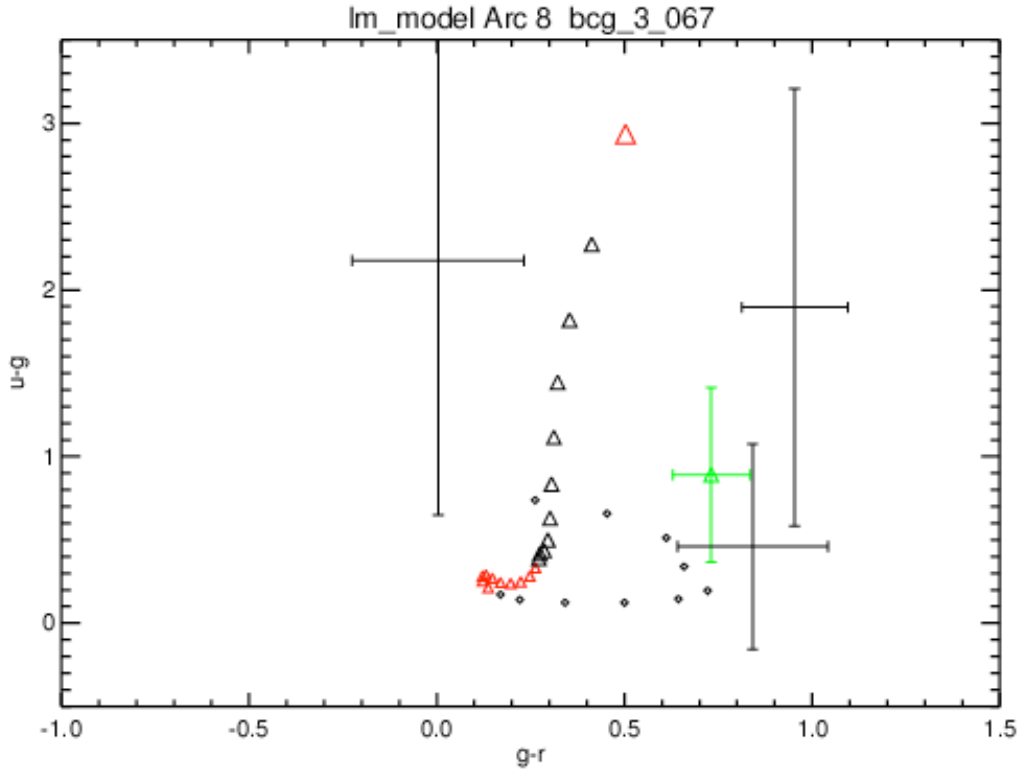
lm_model Arc 8 bcg_3_067
u-g
g-r
3
2
1
0
-1.0
-0.5
0.0
0.5
1.0
1.5

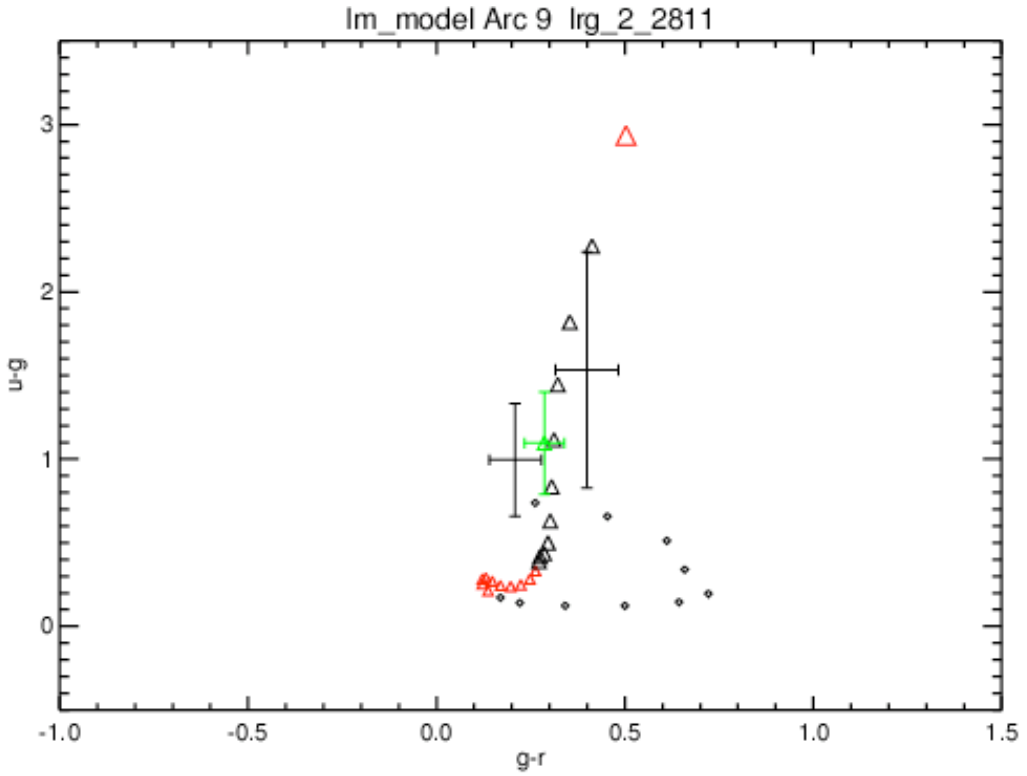
lm_model Arc 9 lrg_2_2811
u-g
g-r
3
2
1
0
-1.0
-0.5
0.0
0.5
1.0
1.5

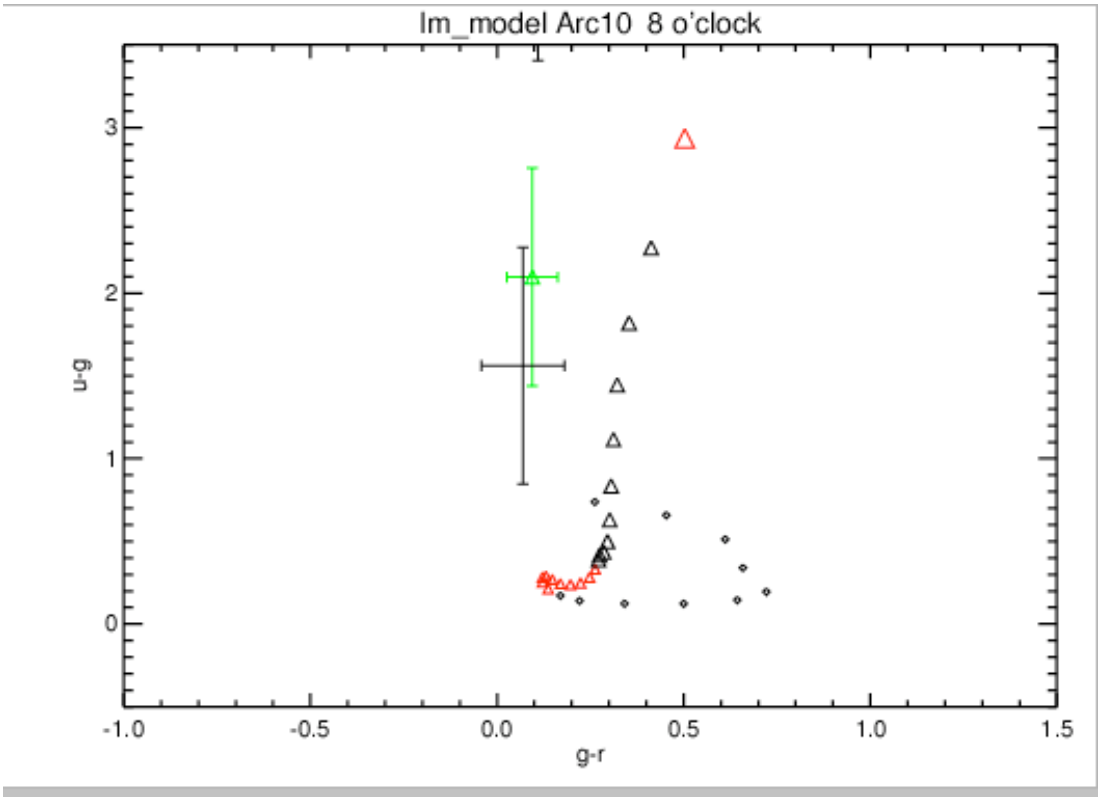
lm_model Arc10 8 o'clock
u-g
g-r
3
2
1
0
-1.0
-0.5
0.0
0.5
1.0
1.5

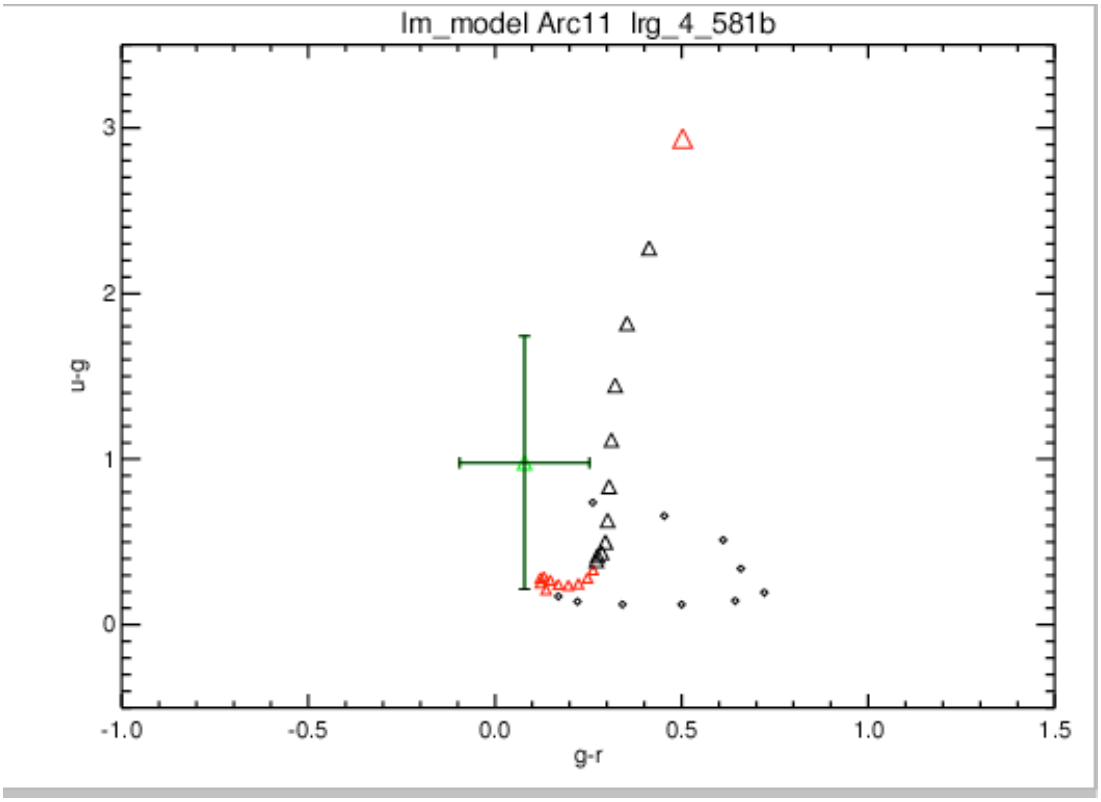
lm_model Arc11 lrg_4_581b
u-g
g-r
3
2
1
0
-1.0
-0.5
0.0
0.5
1.0
1.5